UNIVERSIDAD COMPLUTENSE DE MADRID
FACULTAD DE CIENCIAS FÍSICAS

TESIS DOCTORAL

Temas selectos en física cuántica de muchos: sistemas cuánticos integrables y abiertos, el método variacional de la matriz densidad reducida y aislantes topológicos

Selected topics in quantum many-body physics : integrable and open quantum systems, the variational reduced density matrix method and topological insulators

MEMORIA PARA OPTAR AL GRADO DE DOCTOR

PRESENTADA POR

Álvaro Rubio García

Directores

Jorge Dukelsky Bercovich
Rafael Alejandro Molina Fernández
Juan José García Ripoll

Madrid

UNIVERSIDAD COMPLUTENSE DE MADRID
FACULTAD DE CIENCIAS FÍSICAS

UNIVERSIDAD
COMPLUTENSE
MADRID

TESIS DOCTORAL

Temas selectos en física cuántica de muchos cuerpos: sistemas cuánticos integrables y abiertos, el método variacional de la matriz densidad reducida y aislantes topológicos

Selected topics in quantum many-body physics: integrable and open quantum systems, the variational reduced density matrix method and topological insulators

MEMORIA PARA OPTAR AL GRADO DE DOCTOR
PRESENTADA POR

Alvaro Rubio García

DIRECTORES
Jorge Dukelsky Bercovich
Rafael Alejandro Molina Fernández
Juan José García Ripoll

TUTORA
Arantzazu Mascaraque Susunaga

Agradecimientos

Hay muchas personas a las que quiero agradecer y dedicar esta tesis. Tanto si su contribución fue grande como pequeña, una parte de ellos está incluida en mi tesis. La mayoría se merecen una dedicatoria más grande, pero espero que se sientan representados con estas palabras.

Me gustaría agradecer en primer lugar a Jorge, quien ha sido mi invaluable guía estos cuatro años. Las charlas en el café, sus consejos, su atención y su ayuda han sido para mí un regalo inestimable en todo este tiempo. Ha sabido hacer de esta etapa un recorrido emocionante y apasionado por llegar a las fronteras del conocimiento pero, sobre todo, ha dotado a este viaje de una calidez y cercanía que han hecho los momentos más duros agradables y los más ligeros apasionantes. Después de todo este tiempo no puedo sino pensar que no he tenido mayor suerte que tenerle a él como director, guía y amigo.

Otra persona a la que quiero agradecer y sin cuya compañía esta tesis no hubiera tenido lugar es Rafa. Su cercanía, su curiosidad, su interés por los nuevos temas y su apoyo constante en el doctorado son impagables. Los buenos momentos en los cafés con él han sacado del doctorado momentos bastante entretenidos y lo ha hecho cien veces más llevadero. Me siento muy agradecido de haber coincidido con Rafa este tiempo.

Me gustaría dedicar unas palabras también a Juanjo, mi primer director, con quien entré a la Academia y di mis primeros pasos en la ciencia. Junto con él descubrí en la programación una pasión que me ha enamorado todos estos años. Su dedicación y sus aportaciones le han dado a esta tesis una calidad inestimable. Aún recuerdo con mucha nostalgia aquellos días en Benasque con él y su grupo.

Un lugar especial en esta tesis lo tienen Pedro y Eduardo por todas las charlas y buenos momentos en el café que han convertido bastantes mañanas que empezaban duras en días divertidos y agradables. Por fortuna, la soledad en mi despacho la han llenado hasta desbordarla Yuriko, Ana, María y Nacho, por esos aportes de alegría que han dado tantos buenos momentos. Ni que decir que las comidas con Miriam y Paloma han sido de los momentos más reconfortantes que he pasado en el CSIC.

Quiero agradecer a Isa por todo su cariño y su apoyo, tanto en los buenos como en los malos momentos. He descubierto en ella a una amiga que ha hecho mi vida mil veces más agradable. Sin olvidarme tampoco de Víctor, Óscar, Jaime, Álvaro, Carlos, Marina, Belén y Simón, que, después de casi *toda una vida, siguen siendo los mejores amigos que se puede tener. Un lugar especial siempre lo tendrá Don José Luis. Su pasión por enseñar, su cariño y su cercanía han dejado en mí una marca que no se va a borrar nunca.*

María fue mi mejor compañía en los primeros pasos en este doctorado y llenó todo ese tiempo de luz y color. Si por un lado me han ayudado a progresar académicamente, María ha sido la persona que más me ha ayudado a progresar en mi lado más humano. Su cariño y su confianza son de los que han dejado una huella más profunda en mí. Por otro lado, quiero agradecer a Leticia por acompañarme en los últimos pasos en esta tesis, por hacerme más llevadera esta escritura en medio de la cuarentena.

Por supuesto no me olvido de Diego, Pablo y Elías. Su cariñosa acogida en Buenos Aires y los largos años de amistad y colaboración han contribuido en buena parte a esta tesis. I would also like to thank Jiannis and Chris for their heartwarming welcome in Leeds. In hindsight, I only regret not having stayed longer in there with them.

En un lugar especial quiero agradecer a mis padres. Sin ellos no sería la persona que soy ahora. Su educación, su cariño, su cultura y su apoyo constante han sido los que me han sostenido en los malos y en los buenos momentos y es imposible entender al Álvaro de la tesis sin comprenderles antes a ellos. Me gustaría agradecer también a mis hermanos por todos los buenos momentos que hemos disfrutado en compañía.

En último lugar, quiero dedicar esta tesis a mi abuelo Alberto, a quien le hubiese hecho muchísima ilusión poder verme defendiendo la tesis. Ha sido una motivación constante y la razón de que yo haya salido de ciencias.

Álvaro

Contents

Temas selectos en física cuántica de muchos cuerpos: sistemas cuánticos integrables y abiertos, el método variacional de la matriz densidad reducida y aislantes topológicos

Resumen

El problema de muchos cuerpos es un tema central y omnipresente en la física cuántica con aplicaciones muy variadas, desde el diseño de nuevos fármacos hasta la investigación en nanotecnologías o la construcción de los ordenadores cuánticos. En esta tesis hemos estudiado tres temas relevantes en física cuántica de muchos cuerpos: la descripción de nuevos modelos exactamente solubles que describen la interacción de un sistema con su entorno, el avance en el método variacional de la matriz densidad reducida para calcular estados fundamentales de sistemas cuánticos cerrados y la caracterización de las fases y corrientes topológicas en aislantes topológicos.

Nuestra primera línea de trabajo ha consistido en encontrar soluciones exactas a sistemas cuánticos abiertos de muchos cuerpos. Cualquier sistema cuántico está conectado con su entorno y, aunque la interacción entre ambos frecuentemente es indeseada, muchas veces otorga al sistema un conjunto de propiedades que son fundamentales para el desarrollo de campos como la óptica cuántica, la información cuántica, la resonancia magnética nuclear, la nanotecnología u otras aplicaciones generales de la mecánica cuántica. Es por ello que el progreso en el estudio de las propiedades dinámicas de los sistemas cuánticos abiertos tiene gran importancia. Esta línea de trabajo se ha centrado, por una parte, en encontrar soluciones exactas a la evolución temporal de sistemas cuánticos de muchos cuerpos abiertos en el régimen de Lindblad-Gorini-Kossakowski-Sudarshan y, por otra, en la caracterización de las propiedades dinámicas de dichos sistemas.

La evolución temporal de un sistema cuántico abierto es descrita por el operador Liouvilliano, cuyos autovalores definen los posibles tiempos de decaimiento del sistema. En nuestro primer trabajo hemos propuesto un nuevo Liouvilliano basado en los sistemas de Richardson-Gaudin en el álgebra $SU(N)$, cuyos autoestados y autovalores se pueden resolver exactamente a través de un sistema de ecuaciones no lineales. Hemos conseguido demostrar que este Liouvilliano es una generalización de modelos anteriores exactamente solubles y hemos analizado las propiedades de los autoestados exactos y el

espectro completo del Liouvilliano. Además, hemos derivado un modelo de estado cuántico coherente capaz de describir el estado estable y los estados con el decaimiento más lento del Liouvilliano en el límite termodinámico.

En nuestro segundo estudio hemos propuesto una nueva familia de Liouvillianos exactamente solubles que interpola entre dos modelos de Richardson-Gaudin. Introduciendo a la vez saltos aleatorios entre el sistema y el entorno, hemos construido por primera vez un Liouvilliano que tiene una transición continua entre los regímenes integrable y caótico en función de un único parámetro. Hemos caracterizado dicha transición usando tanto la distribución de las distancias a primeros vecinos de los autovalores del Liouvilliano como los ratios complejos entre las distancias entre autovalores, encontrando una concordancia excelente entre ambos métodos y destacando la ventaja de usar los ratios complejos de los autovalores a la hora de caracterizar la transición al caos en sistemas cuánticos abiertos dada su sencillez.

Nuestra segunda línea de trabajo se ha centrado en el método variacional de la matriz densidad reducida (vRDM en inglés). Encontrar la solución de un problema cuántico de muchos cuerpos cuando no hay solución exacta es extremadamente complicado dado el crecimiento exponencial del espacio de Hilbert con el número de grados de libertad del sistema. El método vRDM propone evitar este problema centrándose en la matriz densidad reducida del sistema, que solo crece polinomialmente, en lugar de estudiar la función de onda. El método vRDM consiste en minimizar la energía del sistema a la vez que impone condiciones a la matriz densidad reducida para que sea física en todo momento. Estas condiciones son las llamadas condiciones de N-representabilidad y anteriormente a nuestro trabajo solo unas pocas habían sido descritas e impuestas en el método vRDM. En esta línea nos hemos centrado en encontrar más condiciones de N-representabilidad en el espacio de señoridad cero, o espacio DOCI, en el cual los niveles de energía están doblemente degenerados y las partículas se agrupan por pares.

En nuestros tres primeros trabajos hemos presentado nuevas condiciones de N-representabilidad que usamos para estudiar diversos sistemas de modelos de pares, física molecular y sistemas de magnetismo cuántico. Nuestros resultados muestran una gran mejora en la estimación de la energía del estado fundamental del sistema y su matriz densidad reducida cuando incrementamos el número de condiciones de N-representabilidad impuestas, con precisiones relativas del orden de $10^{-4} - 10^{-7}$ en la energía del estado fundamental. También hemos medido las escalas de tiempo asintóticas necesarias para encontrar el estado fundamental y hemos implementado un novedoso diseño de las condiciones de N-representabilidad que tiene en cuenta las simetrías del sistema para reducir su coste computacional. Esta implementación nos ha permitido estudiar el modelo de Heisenberg en 1 y 2 dimensiones alcanzando 256 sitios con una precisión relativa en la energía del estado fundamental del orden de 10^{-4}.

Nuestra tercera línea de trabajo se ha centrado en los aislantes topológicos. La clasificación de fases topológicas de la materia es un tema fascinante en la física cuántica de muchos cuerpos con multitud de aplicaciones en sistemas de información cuántica y en el diseño de nuevas tecnologías cuánticas. Las propiedades topológicas muestran una gran resiliencia ante pequeñas deformaciones del sistema y subyacen en los efectos Hall cuánticos entero y fraccional. Una clase particular de fases topológicas son los aislantes topológicos, sistemas de fermiones libres caracterizados por un invariante topológico. Este número cuántico relaciona la topología del núcleo del sistema, intrínsecamente aislante y protegido por un gap de energía, con la aparición de corrientes en la frontera del material.

En un primer estudio investigamos cómo afecta la presencia de interacciones al diagrama de fases topológico del modelo de Haldane, el primer modelo descubierto de aislantes topológicos. Considerando dos copias del modelo con espín y la acción de interacciones espín-espín en el sitio, aproximamos el estado fundamental del sistema combinando nuevas técnicas de campo medio y estados de producto de matrices, demostrando la supervivencia de las fases topológicas del modelo de Haldane hasta interacciones relativamente fuertes.

Nuestro siguiente trabajo se centró en el estudio de aislantes topológicos en presencia de potenciales inhomogéneos. Este trabajo revela la existencia de estados localizados y corrientes localizadas en el núcleo del sistema inducidos por los gradientes de potencial. Hemos sido capaces de explicar dichas corrientes usando teoría de perturbaciones sobre los autoestados del modelo de Haldane en un cilindro y, además, hemos mostrado las corrientes que aparecen considerando el sistema completo en el cilindro.

Finalmente, hemos realizado dos propuestas experimentales en sistemas de átomos fríos para implementar ambos trabajos, el modelo de Haldane con interacciones y el modelo de corrientes topológicas en el núcleo del aislante topológico. Ambos propuestas pueden ser implementadas experimentalmente con la tecnología disponible actual, incluyendo una novedosa técnica para observar y medir las corrientes de borde y de núcleo en un aislante topológico.

Selected topics in quantum many-body physics: integrable and open quantum systems, the variational reduced density matrix method and topological insulators

Abstract

The many-body problem is central and ubiquitous in quantum physics. Its applications are far reaching, varying from the design of new drugs to the research on novel nanotechnologies or building quantum computers. In this thesis we have studied three relevant topics of quantum many-body physics: the description of new exactly solvable models that describe the evolution of quantum systems in contact with the environment, the advance in the variational reduced density matrix method to compute ground states of closed quantum systems and the characterization of the topological phases and currents in topological insulators.

Our first line of work dealt with finding exact solutions of open quantum many-body systems. Every quantum system is connected to its environment and, while the interaction between them is often undesired, it also provides the system with a set of rich properties that are very important in the development of quantum optics, quantum information, nuclear magnetic resonance, nanotechnology and other applications of quantum physics. It is then of great importance to advance in the study of the dynamics of open quantum systems. This line of work has focused, on one part, on finding exact solutions to the time evolution of open quantum many-body systems under the Lindblad-Gorini-Kossakowski-Sudarshan approximation and, on the other, on the characterization of the dynamical properties of such systems.

The temporal evolution of an open quantum system is described by the Liouvillian operator, whose eigenvalues define the decay timescales of the system. In our first work we have proposed a new Liouvillian based on the $SU(N)$ Richardson-Gaudin models, whose exact eigenstates and eigenvalues we can find by solving a system of non linear equations. We found that this Liouvillian is a generalization of previous exactly solvable models and analysed the complete Liouvillian spectrum and the structure of the exact eigenstates. We also derived a coherent state ansatz capable of describing the steady state and slowest decaying eigenstates in the thermodynamic limit.

In our second work we proposed a new family of integrable Liouvil-

lians that can interpolate between two kinds of Richardson-Gaudin models. By introducing random interactions with the environment we constructed a novel Liouvillian that has a continuous transition between the integrable and chaotic regimes in terms of a single parameter. We characterized the transition using both the level spacing distribution of the eigenvalues and the complex spacing ratios, finding an excellent agreement between both approaches and affirming the advantages of using the complex spacing ratios to characterize chaos in open quantum systems.

Our second line of work dealt with the variational reduced density matrix (vRDM) method. Solving the quantum many-body problem when there is no exact solution is a hard problem due to the exponential growth of the Hilbert space with the number of degrees of freedom of the system. The vRDM method proposes to circumvent this problem by focusing on the reduced density matrix of the system, which only grows polynomially, instead of focusing on the wave function. The vRDM method minimizes the energy of the system while imposing constraints on the reduced density matrix to keep it physical. These constraints are called the N-representability conditions and, previous to our work, only a very limited set of conditions had been described and imposed. In our work we have focused on expanding these conditions in the seniority zero space, or DOCI space, where there is a double degeneracy of all single particle levels and all particles are paired.

In our first three works we presented new sets of N-representability conditions and we used them in the study of several pairing, molecular and quantum magnetism models. Our results show a good improvement in the estimation of the ground state energy and the computed reduced density matrices as more N-representability conditions are imposed, with approximate relative accuracies of order $10^{-4} - 10^{-7}$ in the ground state energy. We have also measured the asymptotical time scaling of vRDM and implemented a novel scheme to take advantage of the underlying symmetries of the system to reduce the computational cost. This implementation allowed us to study the 1D and 2D Heisenberg models with up to 256 lattice sites with a relative precision in the ground state energy of order 10^{-4}.

The third branch of our work studied topological insulators. The classification of topological phases of matter is a fascinating topic of quantum many-body physics with many applications in quantum information systems and in the design of new quantum technological devices. The topological properties are intrinsically resilient to smooth deformations of the Hamiltonian and underlie the Integer and Fractional Quantum Hall effects. Our study was centred on a particular class of topological phases, the topological insulators (TI), free fermionic systems characterized by a quantum topological invariant. This quantum number relates the topology of the bulk of the system, intrinsically insulating and protected by an energy gap, with the appearance of net currents along the boundaries of the material.

In a first study we have addressed how much does the presence of interactions affect the quantum topological phase diagram of the Haldane model, the first discovered example of a TI. Considering two spinful copies of the Haldane model and spin-spin on-site interactions we approximated the ground state of the model by combining novel techniques of mean-field and matrix product states, proving the survival of the topological phases of the Haldane model until relatively large interaction strengths.

Our next work focused on the study of TIs in the presence of inhomogeneous potentials. This work revealed the emergence of novel localized states and associated currents in the bulk of the system induced by the potential gradients. We were able to explain the origin of these bulk currents using perturbation theory on the Haldane eigenstates in a cylinder and we also analysed the bulk currents with the complete Hamiltonian in the cylinder.

Finally, we proposed two experimental implementations in ultracold atom experiments of both works, the interacting Haldane model and bulk currents in TI. The two proposals can be implemented using state-of-the-art methods and we designed a novel technique to observe and measure the topological edge and bulk currents in a topological insulator.

Publications

List of works by topic:

- Integrable and open quantum many-body systems:
    - Trigonometric $SU(N)$ Richardson-Gaudin models and dissipative multi-level atomic systems, *S Lerma-Hernández, A Rubio-García, J Dukelsky*, Journal of Physics A: Mathematical and Theoretical **53** (39), 395302 (2020)
    - From integrability to chaos in quantum Liouvillians, *A Rubio-García, RA Molina, J Dukelsky*, arXiv preprint arXiv:2102.13452 (2021)

- The variational reduced density matrix method:
    - Benchmarking the Variational Reduced Density Matrix Theory in the Doubly Occupied Configuration Interaction Space with Integrable Pairing Models, *A Rubio-García, DR Alcoba, P Capuzzi, J Dukelsky*, Journal of chemical theory and computation **14** (8), 4183-4192 (2018)
    - Variational reduced density matrix method in the doubly occupied configuration interaction space using three-particle N-representability conditions, *Diego R Alcoba, Pablo Capuzzi, Alvaro Rubio-García, Jorge Dukelsky, Gustavo E Massaccesi, Ofelia B Ona, Alicia Torre, Luis Lain*, The Journal of chemical physics **149** (19), 194105 (2018)
    - Variational reduced density matrix method in the doubly-occupied configuration interaction space using four-particle N-representability conditions: Application to the XXZ model of quantum magnetism, *A Rubio-García, Jorge Dukelsky, DR Alcoba, P Capuzzi, OB Oña, E Ríos, A Torre, L Lain*, The Journal of chemical physics **151** (15), 154104 (2019)
    - Variational determination of the two-particle reduced density matrix within the doubly occupied configuration interaction space: exploiting translational and reflection invariance, *GE Massaccesi, A Rubio-García, P Capuzzi, E Ríos, OB Oña, J Dukelsky, L Lain, A Torre, DR Alcoba*, Journal of Statistical Mechanics: Theory and Experiment **2021** (1), 013110 (2021)

- Topological insulators:
    - Topological phases in the Haldane model with spin-spin on-site interactions, *A Rubio-García, JJ García-Ripoll*, New Journal of Physics **20** (4), 043033 (2018)
    - Topological bulk states and their currents, *CN Self, A Rubio-García, JJ García-Ripoll, JK Pachos*, Physical Review B **102** (4), 045424 (2020)
    - Seeing topological edge and bulk currents in time-of-flight images, *A Rubio-García, CN Self, JJ García-Ripoll, JK Pachos*, Physical Review B **102** (4), 041123 (2020)

Chapter 1

Integrable models

1.1 Introduction

Open quantum systems are ubiquitous in nature, as it is often impossible to completely decouple a system under study from its environment. While the effects of this coupling are, in many cases, undesired, they have a big impact on the evolution of the system and they enrich it with novel properties that spread into many relevant fields of study, such as quantum optics [1, 2], quantum information [3, 4], nanotechnology [5], nuclear magnetic resonance [6] or general applications of quantum physics [7]. It is, therefore, of vital interest to advance in the understanding of the fundaments of open quantum systems.

In general, the interactions with the environment are extremely complex and the understanding of the dynamics can be very difficult, specially if the system retains memory about the quantum state of the system. Therefore, in the majority of works the dynamics of open quantum systems are treated in the Lindblad-Gorini-Kossakowski-Sudarshan (LGKS) regime [8, 9], which assumes that the environment is big enough that its quantum state is not affected by the system, that the interactions remain weak and that the environment is Markovian, i.e. that it does not retain memory about the quantum state of the system. These approximations enable us to study the system as a quantum density matrix whose time evolution is governed by the Lindblad master equation, which, in turn, is described by the Liouvillian superoperator [8, 9].

Solving the Lindblad master equation is as hard as solving its counterpart for closed systems, the Schrödinger equation, and so far only a few models are known that have an exact solution. These are classified into: linear fermionic and bosonic systems for which an analytical solution exists [10, 11], systems with pure particle gain or loss [12] and collective spin models that fall into the class of exactly solvable Richardson-Gaudin (RG) models [13, 14], which we will introduce later.

Aside from the exact solution, much knowledge would be gained by a better understanding of the dynamical properties of open quantum systems. In this area some work has been done on the static spectral properties of random Liouvillians [15, 16] and on the universal classification of the spectral properties according to the symmetries of the Liouvillian [17, 18], for which a near universal cubic repulsion of the Liouvillian eigenvalues has been found like the Ginibre ensemble of random non hermitian matrices [19]. However, still much work remains to be done into the classification of integrable and chaotic Liouvillians and the transition between the two regimes [20].

This Chapter is organized as follows. Section 1.2 introduces the general concept of integrable or exactly solvable quantum many-body systems and focusses on the special class of integrable RG models. It reports on the different classes of RG models, the Bethe ansatz eigenstates and how exact solutions with algebraic complexity can be found. Two particular examples of RG models are presented in Section 1.3: the reduced BCS model or constant pairing model and the topological Richardson-Gaudin-Kitaev Hamiltonian. In Section 1.4 the general theory of open quantum systems is introduced among a detailed analysis of the Liouvillian superoperator and its properties. The following sections are dedicated to the results of our work using Richardson-Gaudin models to study new families of exactly solvable Liouvillians. Section 1.5 is based on our article *Trigonometric $SU(N)$ Richardson–Gaudin models and dissipative multi-level atomic systems* [21] and introduces a general $SU(N)$ atomic system with collective interactions with the environment that is derived from the trigonometric $SU(N)$ RG model. The characteristics of the exact solution, the form of the spectrum and the thermodynamic limit are discussed. Section 1.6, based on our article *From integrability to chaos in quantum Liouvillians* [22], reports a novel Liouvillian that interpolates between a line of integrability and chaos. The spectral properties of this model are analysed using the level spacing distribution and complex spacing ratios and a complete characterization of the integrable to chaotic transition in open systems is found. Finally, conclusions are drawn in Section 1.7.

1.2 Richardson-Gaudin models

Solving the quantum many-body problem is hard. The dimension of the Hilbert space grows exponentially with the number of degrees of freedom and exact solutions are thus limited to small systems. While some state-of-the-art numerical methods are so sophisticated that the solution of medium and large size systems is within an acceptable accuracy range, the problem of finding the *exact* solution still persists. Fortunately, for some particular systems their exact solution can be found with algebraic complexity. Among these are systems that are solved using the Bethe ansatz, such as the 1D Heisenberg chain [23], the 1D Hubbard model [24] and Richardson-Gaudin (RG) models [25–29], to which the celebrated reduced BCS model of superconductivity [30] belongs.

While there is not yet a precise definition of what is an integrable quantum system [31–33], some authors define it as one for which there is a set of independent operators, called the integrals of motion (IOM), that commute among themselves and with the Hamiltonian and there are as many IOM as degrees of freedom in the system. An additional definition is that a system is exactly solvable if every one of its eigenstates can be found with algebraic complexity [33], e.g. if the exact solutions are found by solving a system of coupled non linear equations. These two definitions of quantum integrability are derived from classical integrability and, although they are commonly employed in the literature, are still under debate.

The first integrable system found was the Heisenberg XXX chain [23] of quantum magnetism. In his article, Bethe found that the exact eigenstates of the model are a product of one-body terms whose exact expression he could find by solving a system of non linear equations. These kind of eigenstates are called the Bethe ansatz. Nevertheless, while the eigenstates where early found, the exact IOM for the XXX chain proved to be a much more difficult task that could only be solved several decades later [34].

A case for which the IOM are restricted to simpler two-particle operators are the Richardson-Gaudin (RG) models. The first steps to their discovery were given when Richardson [35–38] found the exact solution of the reduced BCS model [30], which had offered the first description of superconductivity in terms of the pairing of fermionic particles. Unfortunately, his solution passed unnoticed for several decades. Later, Gaudin found similar expressions for the integrability of the Gaudin magnet spin model [39, 40]. Then, in the mid-90s, the research on ultra small metallic grains [41–43] attracted a renewed interest to the constant pairing model, for which, at the same time, Cambiaggio, Rivas and Saraceno [44] were the first to describe its IOM. Finally, at the beginning of the century, it all came together when Richardson's exact solution was rediscovered [45, 46]. These studies, together with the previous work in the Gaudin magnet, whose IOM are the large interaction strength limit of the RG IOM, served as the basis of a much broader set of integrable Hamiltonians, the Richardson-Gaudin models.

While RG models cannot serve as a basis of universal two-body Hamiltonians, they have allowed to study a rich variety of physically relevant quantum many-body systems: the reduced BCS model [28, 30, 47, 48], superconductivity in small metallic grains [27, 41, 46, 49, 50], bosonic systems [25], confined bosons systems [26], the quantum phases of $p_x + ip_y$ superconductors [51–53], the Richardson-Gaudin-Kitaev [54] model of topological superconductivity based on the topological Kitaev wire [55], central spin systems [39, 40, 56] and even matter-radiation models of quantum optics and cold atom physics [13, 14, 21].

1.2.1 Richardson-Gaudin models

Richardson-Gaudin models are defined by the particular form of its integrals of motion, composed of one- and two-body operators [44]. For a chain of L spins they are

$$R_i = S_i^z + g \sum_{j=1(\neq i)}^{L} \frac{X_{ij}}{2} \left(S_i^+ S_j^- + S_i^- S_j^+ \right) + Z_{ij} S_i^z S_j^z, \quad i = 1, \ldots, L, \tag{1.1}$$

with S_i^α the $SU(2)$ spin operator at site i of arbitrary magnitude s_i. In order to be integrable, the IOM have to commute among themselves $[R_i, R_j] = 0$, which is satisfied when [25, 27]

$$\begin{aligned} X_{ij} = -X_{ji}, \quad Z_{ij} = -Z_{ji} \\ X_{ij} X_{jk} - X_{ik} \left(Z_{ij} + Z_{jk} \right) = 0. \end{aligned} \tag{1.2}$$

The solutions of this set of equations are classified into three models defined by the sign of the constant $\Gamma = X_{ij}^2 - Z_{ij}^2$ [25, 27]:

- The rational or XXX model, $\Gamma = 0$:

$$X_{ij} = Z_{ij} = \gamma \frac{1}{\eta_i - \eta_j}, \tag{1.3}$$

  with η_i a set of arbitrary parameters.

- The hyperbolic or XXZ model, $\Gamma = -\gamma^2 < 0$:

$$X_{ij} = \gamma \frac{1}{\sinh \left(\eta_i - \eta_j \right)}, \quad Z_{ij} = \gamma \coth \left(\eta_i - \eta_j \right). \tag{1.4}$$

  or, in a simpler parametrization,

$$X_{ij} = 2\gamma \frac{\sqrt{\eta_i \eta_j}}{\eta_i - \eta_j}, \quad Z_{ij} = \gamma \frac{\eta_i + \eta_j}{\eta_i - \eta_j}. \tag{1.5}$$

- The trigonometric model, $\Gamma = \gamma^2 > 0$:

  $$X_{ij} = \gamma \frac{1}{\sin(\eta_i - \eta_j)}, \quad Z_{ij} = \gamma \cot(\eta_i - \eta_j) \,. \tag{1.6}$$

  This and the hyperbolic models are interchangeable by the mapping $\eta_j \to i\,\eta_j$.

In the following, we set $\gamma = 1$ without loss of generality. Note that also the IOM commute with the total magnetization operator $S^z = \sum_i S_i^z$, which is then an additional constant of motion of RG models.

In general, the Hamiltonian of a Richardson-Gaudin model is an arbitrary linear combination of the IOM

$$H = \sum_{i=1}^{L} \varepsilon_i R_i. \tag{1.7}$$

where ε_i are arbitrary parameters. This Hamiltonian commutes with the IOM and, therefore, there is a basis of eigenstates that simultaneously diagonalizes the Hamiltonian and all IOM, defining a set of $L+1$ constants of motion given by the expectation values of the IOM and the total magnetization S^z. The exact form of the eigenstates is given by a Bethe ansatz

$$|\Psi\rangle = \prod_{\alpha=1}^{M} \left(\sum_{i=1}^{L} X_{i\alpha} S_i^+ \right) |0\,\rangle, \tag{1.8}$$

with $|0\rangle$ a vacuum state and M the number of excitations corresponding to the eigenstate. The matrix $X_{i\alpha}$ corresponds to the X_{ij} matrix of the IOM (1.1) with $\eta_j \to E_\alpha$. These last parameters, E_α, are a set of M complex spectral parameters, usually called the rapidities or pair energies. This product state ansatz is an eigenstate of the magnetization operator with eigenvalue $M - L/2$.

For the Bethe ansatz eigenstate to be a simultaneous eigenstate of the IOM and the Hamiltonian, the pair energies E_α must satisfy a set of conditions given by the RG equations. These are found by acting with a generic

IOM onto the ansatz eigenstate

$$\begin{aligned} R_i|\Psi\rangle = {} & s_i \left(-1 + g \sum_{j(\neq i)} Z_{ij} s_j - g \sum_{\alpha} Z_{i\alpha} \right) |\Psi\rangle \\ & + \sum_{\alpha} \prod_{\beta(\neq\alpha)} \Lambda^{\dagger}_{\beta} X_{i\alpha} \left(1 + g \sum_{j} s_j Z_{j\alpha} + g \sum_{\gamma(\neq\alpha)} Z_{\alpha\gamma} \right) S_i^+ |0\rangle . \end{aligned} \tag{1.9}$$

with $Z_{i\alpha}$ also formed by replacing the corresponding j variable by E_α. In order for $|\Psi\rangle$ to be an eigenstate of R_i the second line must be zero, which can only happen when the pair energies satisfy the following system of non linear equations, the Richardson-Gaudin equations,

$$1 + g \sum_{i=1}^{L} s_j Z_{j\alpha} + g \sum_{\beta=1(\neq\alpha)}^{M} Z_{\alpha\beta} = 0, \quad \alpha = 1, \dots, M. \tag{1.10}$$

In principle there are many solutions to this equation, each one corresponding to a particular Hamiltonian eigenstate. Once a particular solution has been found, the eigenvalues r_i of the IOM for that eigenstate are

$$R_i|\Psi\rangle = r_i|\Psi\rangle = s_i \left(-1 + g \sum_{j=1(\neq i)}^{L} Z_{ij} s_j - g \sum_{\alpha=1}^{M} Z_{i\alpha} \right) |\Psi\rangle. \tag{1.11}$$

Because the RG Hamiltonian is written as a linear combination of the IOM, the Hamiltonian eigenstates are

$$E = \sum_{i=1}^{L} \varepsilon_i r_i = \sum_{i=1}^{L} \varepsilon_i s_i \left(-1 + g \sum_{j=1(\neq i)}^{L} Z_{ij} s_j - g \sum_{\alpha=1}^{M} Z_{i\alpha} \right) . \tag{1.12}$$

Solving the RG equations for $s_i = 1/2$

The exact eigenstates and eigenvalues of the RG Hamiltonian can be computed exactly with algebraic complexity by solving the RG equations (1.10), which can present a lot of singularities. Specifically, this is the case when two pair energies become degenerate, $E_\alpha \equiv E_\beta$, or when a pair energy crosses one of the parameters of the IOM, $E_\alpha \equiv \eta_i$. Fortunately, for systems of spin

$s_i = 1/2$, the pair energies can be mapped to other variables Λ_i in order to get rid of the singularities [57]

$$\Lambda_i = \sum_{\alpha=1}^{M} Z_{i\alpha}, \tag{1.13}$$

where the specific form of $Z_{i\alpha}$ depends on whether the integrable model is rational, trigonometric or hyperbolic. In terms of these parameters the RG equations (1.10) are transformed into a set of L coupled quadratic equations without singularities

$$\Lambda_i^2 = M(L-M)\Gamma - \frac{2}{g}\Lambda_i + \sum_{j(\neq i)}^{L} Z_{ij}\left(\Lambda_i - \Lambda_j\right), \quad i = 1, \ldots, L, \tag{1.14}$$

with $\Gamma \in \{0, \pm 1\}$ a constant depending on the integrability class (1.3). Once a set of valid Λ_i parameters has been found, the eigenstate energies of the IOM are

$$r_i = \frac{1}{2}\left(-1 - g\Lambda_i + \frac{g}{2}\sum_{j(\neq i)}^{L} Z_{ij}\right). \tag{1.15}$$

and the Hamiltonian eigenstates

$$E = \sum_i \varepsilon_i r_i = \frac{1}{2}\sum_{i=1}^{L}\varepsilon_i\left(-1 - g\Lambda_i + \frac{g}{2}\sum_{j(\neq i)}^{L} Z_{ij}\right). \tag{1.16}$$

Computing exact observables

The particular form of the RG integrals of motion makes it easy to extract the expectation values of S_i^z from the eigenvalues of the IOM. This is done by expressing the local z spin operators as

$$S_i^z = R_i - g\frac{\partial R_i}{\partial g}. \tag{1.17}$$

Using the Hellmann-Feynman theorem, the expectation value $\langle S_i^z \rangle$ is written in terms of derivatives of the expectation value of R_i (1.15)

$$\langle S_i^z \rangle = r_i - g\frac{\partial r_i}{\partial g} = -\frac{1}{2} + \frac{g^2}{2}\frac{\partial \Lambda_i}{\partial g}, \tag{1.18}$$

which can often be computed exactly from the exact solution of Λ_i.

Pairing models

Richardson-Gaudin models often correspond to pairing models, which are models that conserve the number of broken pairs in the system. One example of such is the reduced BCS Hamiltonian or constant pairing model [30]

$$H = \frac{1}{2}\sum_{i=1}^{L} \varepsilon_i \left(c_i^\dagger c_i + c_{\bar{i}}^\dagger c_{\bar{i}} \right) - g \sum_{ij}^{L} c_i^\dagger c_{\bar{i}}^\dagger c_{\bar{j}} c_j . \tag{1.19}$$

with ε_i the single particle levels and g the interaction strength. The interaction term of this Hamiltonian acts on pairs of degenerate particles $c_i^\dagger c_{\bar{i}}^\dagger$, but it does not act on broken pairs $c_i^\dagger$ or $c_{\bar{i}}^\dagger$. Therefore, the number of broken pairs in the system is a symmetry of the model measured by the seniority operator

$$\Omega = \sum_{i=1}^{L} \left(c_i^\dagger c_i - c_{\bar{i}}^\dagger c_{\bar{i}} \right)^2 . \tag{1.20}$$

These models can be written in a simpler form by mapping the explicit pair operators into single $SU(2)$ operators, like the spin operators

$$S_i^+ = c_i^\dagger c_{\bar{i}}^\dagger = \left(S_i^- \right)^\dagger , \quad S_i^z = \frac{n_i + n_{\bar{i}}}{2} - \frac{1}{2} \tag{1.21}$$

or the hard-core boson representation

$$b_i^\dagger = c_i^\dagger c_{\bar{i}}^\dagger = (b_i)^\dagger , \quad n_i = \frac{n_i + n_{\bar{i}}}{2} . \tag{1.22}$$

In this form, the Hamiltonian reflects better the conservation of the number of broken pairs

$$H = \sum_{i=1}^{L} \varepsilon_i \, n_i - g \sum_{ij}^{L} b_i^\dagger b_j . \tag{1.23}$$

1.3 Examples of RG models

In this section we introduce the reduced BCS or constant pairing and the Richardson-Gaudin-Kitaev Hamiltonians.

1.3.1 The reduced BCS model

The celebrated BCS paper [30] gave the first description of superconductivity. In their work, Bardeen Cooper and Schrieffer approximated the electron-phonon interaction as an effective s-wave pairing model and showed that its ground state consists of a condensate of Cooper pairs, which is able to carry electricity with infinite conductivity. While the mean field BCS solution is correct in the thermodynamic limit [47], it presents limitations for small and medium system sizes because the state ansatz does not conserve the particle number. Fortunately, the reduced BCS model is a RG model and its exact eigenstates can be found by solving the RG equations. Using this exact solution it has been found that the phase diagram describes a smooth crossover from a BCS superconductor to a BEC condensate [58].

The reduced BCS Hamiltonian is

$$H = \frac{1}{2}\sum_k \varepsilon_k \left(c_k^\dagger c_k + c_{-k}^\dagger c_{-k} \right) - g \sum_{kk'} c_k^\dagger c_{-k}^\dagger c_{-k'} c_{k'}, \tag{1.24}$$

which can be derived from the linear combination of the rational IOM $H = \sum_i \varepsilon_i R_i$ with $\eta_k = \varepsilon_k$. The Hamiltonian eigenstates are

$$|\psi\rangle = \prod_{\alpha=1}^{M} \left(\sum_k \frac{1}{\varepsilon_k - E_\alpha} c_k^\dagger c_{-k}^\dagger \right) |0\rangle, \tag{1.25}$$

with M the number of pairs of the eigenstate and E_α the pair energies. The Hamiltonian eigenvalues are

$$E = \sum_\alpha E_\alpha. \tag{1.26}$$

One observable of interest of this model is the canonical gap Δ_c, which measures the pair mixing across the Fermi level

$$\Delta_c = \ g \sum_k \sqrt{\langle c_k^\dagger c_{-k}^\dagger c_{-k} c_k \rangle - \langle c_k^\dagger c_k \rangle \langle c_{-k}^\dagger c_{-k} \rangle}. \tag{1.27}$$

This observable coincides in the thermodynamic limit of the mean field BCS solution with that from the exact solution. Additionally, for the mean field solution in finite systems, the critical interaction strength g_c at which the ground state transitions from a metallic gapless phase to a superconducting phase with a finite gap is

$$g_c = \left[\sum_k \frac{1}{\varepsilon_k - \mu} \right]^{-1}, \tag{1.28}$$

with μ the chemical potential, approximated by $\mu = (\varepsilon_{\mathrm{F}} + \varepsilon_{\mathrm{F}+1})/2$, with ε_{F} the Fermi level.

1.3.2 The Richardson-Gaudin-Kitaev model

The Richardson-Gaudin-Kitaev (RGK) model [54] is variation of the 1D topological Kitaev wire [55]. In a similar way, it has topologically non-trivial phases, but the model is extended to include interactions and it is number conserving. The RGK Hamiltonian belongs to the hyperbolic integrability class [51–53] and its exact eigenstates can be calculated for either periodic or antiperiodic boundary conditions. As such, it is an excellent platform to study many-body interacting topological superconductors.

The Hamiltonian of the RGK model is

$$H = \frac{1}{2} \sum_{k \in \mathcal{S}^\phi} \varepsilon_k n_k - g \sum_{kk' \in \mathcal{S}^\phi_+} \sqrt{\eta_k \eta_{k'}}\, c^\dagger_k c^\dagger_{-k} c_{-k'} c_{k'} \tag{1.29}$$

with g the interaction strength, $\mathcal{S}^\phi$ the set of allowed momenta, which depends on the boundary conditions, $\mathcal{S}^\phi_+$ the subset of momenta with $k > 0$ and

$$\varepsilon_k = -2t_1 \cos k - 2t_2 \cos k, \quad \eta_k = \sin(k/2) \sqrt{t_1 + 4t_2 \cos^2(k/2)}, \tag{1.30}$$

where the η_k parameters are antisymmetric $\eta_k = -\eta_{-k}$, corresponding to a model of p-wave superconductivity. For $t_1 = 0$ and $t_2 \neq 0$ there is only nearest neighbour pairing in real space, while for $t_1 \neq 0$ and $t_2 = 0$ there is long range pairing that slowly decays with the distance between the lattice points $1/|i-j|$. With respect to the boundary conditions, for periodic ones the particles with momenta $k = \{0, \pi\}$ become decoupled from the chain and behave as Majorana fermions.

The RGK Hamiltonian is written as a linear combination of the RG hyperbolic IOM

$$H = \sum_{k \in \mathcal{S}^\phi} \eta_k R_k = \sum_{k \in \mathcal{S}^\phi} \eta_k S^z_k - g \sum_{kk' \in \mathcal{S}^\phi} \sqrt{\eta_k \eta_{k'}} \frac{1}{2} \left(S^+_k S^-_{k'} + S^-_k S^+_{k'} \right), \tag{1.31}$$

where the S_k^α operators correspond to the spin representation of the pair operators of degenerate levels $(k,-k)$ (1.21). The eigenstates of the RGK model are

$$|\psi\rangle = \prod_{\alpha=1}^{M}\left(\sum_{k\in\mathcal{S}^\phi} X_{k\alpha} S_k^+\right)|0\rangle \propto \prod_{\alpha=1}^{M}\left(\sum_{k\in\mathcal{S}^\phi} \frac{\sqrt{\eta_k}}{\eta_k - E_\alpha} S_k^+\right)|0\rangle \tag{1.32}$$

with M the number of pairs in the system, related to the total eigenstate magnetization by $\langle S^z\rangle = M - L/2$.

The RGK ground state has two points of interest: the Moore-Read (MR) [51, 59–61] and Read-Green [62] points. At the Read-Green point, $g_{\mathrm{RG}} = 1/(L-2M+2)$, the model undergoes a third order quantum phase transition from a weakly coupled topologically non trivial phase to a trivial strongly coupled one where all Cooper pairs are bounded. In the thermodynamic limit $g_{\mathrm{RG}} \to 1/(L-2M)$ and, thus, there is no phase transition above half filling, $M/L \geq 1/2$.

At the Moore-Read point $g_{\mathrm{MR}} = 1/(L-M+1)$ all pair energies collapse to zero in the ground state $E_\alpha = 0$, independent on the value of η. Thus, the ground state becomes a much simpler pair condensate wave function

$$|\psi_{\mathrm{MR}}\rangle = \left(\sum_{k=1}^{L} \frac{1}{\sqrt{\eta_k}} S_k^+\right)^M |0\rangle, \tag{1.33}$$

which is also know as antisymmetric geminal power (AGP) in quantum chemistry and number projected BCS (PBCS) in nuclear physics.

Similar to the reduced BCS model, one observable of interest of the RGK model is the canonical gap Δ_c

$$\Delta_c = g \sum_{k\in\mathcal{S}^\phi} \sqrt{\eta_k \left(\langle c_k^\dagger c_{-k}^\dagger c_{-k} c_k\rangle - \langle c_k^\dagger c_k\rangle\langle c_{-k}^\dagger c_{-k}\rangle\right)} \tag{1.34}$$

In the thermodynamic limit the canonical gap coincides with the mean field BCS gap [30]

$$\frac{1}{g} = \sum_k \frac{\eta_k}{\sqrt{(\eta_k-\mu)^2 + \eta_k \Delta^2}}, \tag{1.35}$$

with μ the chemical potential. For finite sizes, the system will be in a superconducting phase when there is a finite gap and it will have a phase transition to a metallic phase with $\Delta = 0$ at the critical point

$$g_c = \left[\sum_k \frac{\eta_k}{|\eta_k - \mu|} \right]^{-1}. \tag{1.36}$$

1.4 Open quantum many-body systems

The understanding of open quantum many-body systems is of paramount importance for the study of many relevant physical systems of quantum optics, quantum information, nanotechnology and for general applications of quantum physics. Essentially, all physical systems are in contact with their environment and, while the evolution of a closed quantum system is well described by the Schrödinger equation, open quantum systems are much more convoluted. A complete description would involve treating the system and its environment as a whole and their joint evolution, but this approach is in many cases impracticable, as it involves knowing the exact quantum state of the environment, which is in almost all cases unknown or impossible to compute. Therefore, the usual approach is to work on the LGKS approximation [8, 9] and exclusively focus on the quantum state of the system while also taking into account its interactions with the environment.

The quantum state of the system is described by its density matrix

$$\rho = \sum_i p_i |\psi_i\rangle\langle\psi_i|, \tag{1.37}$$

where the conditions that it must satisfy to be a physical density matrix are: it must have trace one, $\mathrm{tr}(\rho) = \sum_i p_i = 1$; the coefficients must be non negative, $p_i \geq 0$; and the density matrix must be hermitian, $\rho = \rho^\dagger$. Once the initial density matrix of the system is known, the description of the system in contact with its environment can be done done through the Lindblad master equation [8, 9]

$$\dot{\rho} = \mathcal{L}(\rho), \tag{1.38}$$

with $\mathcal{L}$ the Liouvillian superoperator acting on the space of density matrices. This description assumes that the system is in contact with an environment with an infinite number of degrees of freedom and that the interaction between the system and its environment is weak, which leads to Markovian dynamics, i.e. the environment retains no memory of previous quantum states of the system [9, 63]. A non Markovian description of the quantum system is usually much harder to solve than the Lindblad master equation.

As we have seen, the density matrix must satisfy several conditions to be a physical density matrix. Thus, the Lindblad description of the time evolution of the system must preserve these conditions over time, i.e. it has to be trace preserving and a completely positive map, meaning that it maps positive coefficients p_i into positive numbers. Gorini-Kossakowski-Sudarshan [8] on one hand and Lindblad [9] on the other found that the most general form of the master equation that satisfies these conditions is

$$\mathcal{L}(\rho) = -i\,[H,\,\rho] + \sum_j \mathcal{D}_j(\rho), \tag{1.39}$$

with H the Hamiltonian of the system and $\mathcal{D}_j$ a set of dissipation operators acting on the density matrix

$$\mathcal{D}_j(\rho) = L_j^\dagger \rho L_j - \frac{1}{2}\rho L_j^\dagger L_j - \frac{1}{2} L_j^\dagger L_j \rho, \tag{1.40}$$

with L_j the Lindblad jump operators that describe the interaction of the system with its environment. The Hamiltonian commutator $-i[H, \rho]$ describes the unitary evolution of a closed system, while the dissipative part is non unitary. In general, L_j can be any operator describing the interaction with the system. For example, it could describe the absorption of pairs of photons inside a cavity with rate γ, $L = \sqrt{\gamma} a^\dagger a^\dagger$, or the spontaneous collective spin lowering of a set of spins in a chain with rate Γ, $L = \sqrt{\Gamma}\sum_i \sigma_i^-$.

1.4.1 The Liouvillian superoperator

The evolution of the density matrix of an open quantum many-body system is given by the Lindblad master equation, which is completely described by the Liouvillian superoperator $\mathcal{L}$. This is a linear map acting on the space of density matrices and its spectrum is given by [63, 64]

$$\mathcal{L}\left(\rho_i\right) = \lambda_i \rho_i. \tag{1.41}$$

The time evolution of a particular eigenvalue is then

$$e^{\mathcal{L}t}\rho_i = e^{\lambda_i t}\rho_i = e^{\mathrm{Re}(\lambda_i)t} e^{i\mathrm{Im}(\lambda_i)t}\rho_i \tag{1.42}$$

and the evolution of a general density matrix is given by its decomposition into the different Liouvillian eigenvalues

$$\rho = \sum_i c_i \rho_i \to e^{\mathcal{L}t}\rho = \sum_i c_i \, e^{\lambda_i t}\rho_i, \tag{1.43}$$

It can be shown [63, 65] that all Liouvillian eigenvalues have a non positive real part $\mathrm{Re}(\lambda_i) \leq 0$. Thus, in the large time limit, the evolution of a general density matrix will converge into eigenstates whose eigenvalues have a zero real part, $\mathrm{Re}(\lambda_i) = 0$.

Every Liouvillian has at least one eigenstate with zero eigenvalue, the steady state ρ_{SS}, to which the system decays in the infinite time limit

$$\lim_{t\to\infty} e^{\mathcal{L}t}\rho = \rho_{\mathrm{SS}}, \tag{1.44}$$

with ρ a general density matrix at some initial time. If the eigenvalue $\lambda_i = 0$ is degenerate, then there are multiple steady states into which the system will evolve in time depending on its initial configuration. For particular open quantum systems there can also be eigenvalues with zero real part but an imaginary value, so that the system describes oscillations between several eigenstates in the infinite time limit, although these cases are unusual. Apart from the steady state, another state of physical relevance is the one whose eigenvalue has highest non zero real part. This real part, called the dissipative gap, sets the timescale of the slowest relaxation dynamics of the quantum system under the Lindblad evolution

$$\Delta = \min_{\lambda_i:\ \mathrm{Re}(\lambda_i)\neq 0} |\mathrm{Re}(\lambda_i)|. \tag{1.45}$$

Because the trace of the density matrix for long time evolutions must be equal to the trace of the initial density matrix, the trace of the Liouvillian eigenstates ρ_i will depend on the real part of its eigenvalues λ_i

$$\mathrm{tr}(\rho_i) = \begin{cases} 1, & \text{if} \quad \mathrm{Re}(\lambda_i) = 0 \\ 0, & \text{otherwise.} \end{cases} \tag{1.46}$$

Thus, the eigenstates with $\mathrm{Re}(\lambda_i) \neq 0$ have zero trace and do not belong to physical density matrices.

With respect to the full spectrum of the Liouvillian, all eigenstates come in complex conjugate pairs $(\rho_i,\, \lambda_i)$, $(\rho_i^\dagger,\, \lambda_i^*)$. This is shown by complex conjugating the action of the Liouvillian upon the density matrix (1.39)

$$(\lambda_i \rho_i)^\dagger = [\mathcal{L}(\rho)]^\dagger = \mathcal{L}\big(\rho_i^\dagger\big) = \lambda_i^* \rho_i^\dagger. \tag{1.47}$$

From here it can be derived that every eigenstate with real eigenvalue must be hermitian.

While the Liouvillian is a linear operator and has an eigenvalue spectrum, this is not easy to compute in the form of Equation (1.39). In practice, it is easier to map the density matrix space into a vectorial space, so that the action of the Liouvillian operator on the density matrix is written as a matrix-vector product. This is done by mapping the bra and ket spaces to a product space

$$\rho = \sum_{ij} c_{ij} |i\rangle\langle j| \rightarrow |\rho\rangle = \sum_{ij} c_{ij} |i\rangle \otimes |j\rangle. \tag{1.48}$$

Thus, the vectorized space of density matrices has a Hilbert space dimension of $\mathcal{H} \times \mathcal{H}$, with $\mathcal{H}$ the dimension of the original space. In the same way, one can map the operators acting on the left or on the right of the density matrix to operators in the original and a dual spaces, respectively

$$\begin{aligned} O\,\rho &\rightarrow O \otimes \mathbb{I}\,|\rho\rangle \\ \rho\, O &\rightarrow \mathbb{I} \otimes O^T |\rho\rangle. \end{aligned} \tag{1.49}$$

In this form the Liouvillian superoperator is mapped to a matrix form

$$\begin{aligned} &\mathcal{L}|\rho\rangle = \\ &\quad \left[-i \left(H \otimes \mathbb{I} - H^T \otimes \mathbb{I} \right) + \sum_j L_j^\dagger \otimes L_j^T - \frac{1}{2} L_j^\dagger L_j \otimes \mathbb{I} - \frac{1}{2} \mathbb{I} \otimes L_j^T L_j^* \right] |\rho\rangle \end{aligned} \tag{1.50}$$

and standard numerical methods can be used to compute its spectrum.

Liouvillian symmetries

There are two kinds of Liouvillian symmetries: strong and weak symmetries, which will determine its spectral properties [66, 67]. For closed systems, a symmetry operator is usually defined as an operator that commutes with the Hamiltonian $[H, O] = 0$. This symmetry divides the Hilbert space into blocks characterized by the eigenvalues of O. In a similar way, for an open quantum system a strong symmetry is defined by an operator that commutes with both the Hamiltonian and the jump operators $[H, O] = [H, L_j] = 0, \forall j$. This symmetry is a symmetry of the Liouvillian and also divides the vectorized space $\mathcal{H} \times \mathcal{H}$ into blocks. Interestingly, it can be shown that each of these blocks must contain a steady state.

A relaxed condition is that the symmetry operator in the vectorized space commutes with the Liouvillian $[\mathcal{L}, \mathcal{O}] = 0$ but, as $\mathcal{O}$ is a superoperator in the vectorized space, it does not commute with neither the Hamiltonian nor the Lindblad jump operators. This operator defines a weak symmetry of the Liouvillian and, while it also divides the space into different blocks, in general only one of such blocks contains a steady state.

Integrable open quantum systems

An interesting question is whether the exact time evolution of an open quantum system in the LGKS regime can be found exactly. Indeed, some exactly solvable models have been found based on the Bethe ansatz [12] or RG models [13, 14], although its number is very low. However, the full potential of RG models for open quantum systems has not yet been explored. While such models are, in general, hermitian, contrary to the non hermiticity of the Liouvillian superoperator, their integrability properties are kept intact when the parameters of the IOM (1.1), such as the interaction strength g, become complex. This leaves the door open to the study of open quantum systems based on RG models, two examples of which will be studied in the following sections.

1.5 Trigonometric $SU(N)$ RG models and dissipative multilevel atomic systems

The results from this section are reported in our article: *Trigonometric $SU(N)$ Richardson-Gaudin models and dissipative multi-level atomic systems* [21].

In this section we introduce a RG model to study the dynamics of a system of N-level atoms with collective dissipation using the $SU(N)$ RG integrals of motion. We derive the Liouvillian superoperator from a generic set of jumps and analyze in what cases it can be brought to a $SU(N)$ Richardson-Gaudin integrable model. Our results show that this model is a generalization of a previous integrable Liouvillian model [14] for 2-level systems. We also analyze the exact solution of a more complex system of 3-level atoms that has a more interesting spectrum. We show the form of the spectral parameters of the RG equations and study the full spectrum of the model. Finally, we introduce a condensate state ansatz that allows us to study the dissipation gap and lowest decaying modes in the thermodynamic limit.

We start with a system of L atoms with N levels each. The Hamiltonian is

$$H = \sum_{\alpha=1}^{N} \varepsilon_\alpha K_{\alpha\alpha}, \tag{1.51}$$

with $K_{\alpha\beta}$ the generators of the group $U(N)$

$$K_{\alpha\beta} = \sum_{i=1}^{L} |i,\, \alpha\rangle\langle i,\, \beta|, \quad [K_{\alpha\beta},\, K_{\gamma\delta}] = \delta_{\beta\gamma} K_{\alpha\delta} - \delta_{\alpha\delta} K_{\gamma\beta}. \tag{1.52}$$

where $\alpha = 1, \ldots, N$ are the atom levels and i the index of each of the L atoms so that the $K_{\alpha\beta}$ operators represent collective motions of the atomic levels. The linear Casimir $C^1 = \sum_{\alpha=1}^{N} K_{\alpha\alpha} = L$ is a conserved quantity of the system and reduces the number of $K_{\alpha\beta}$ operators from N^2 to $N^2 - 1$, so that they satisfy the $SU(N)$ algebra. This algebra additionally contains the quadratic Casimir

$$C^2 = \sum_{\alpha\beta=1}^{N} K_{\alpha\beta} K_{\beta\alpha} = L^2 + (N-1)L. \tag{1.53}$$

As an example, for a system of $N = 2$ level atoms, the algebra is $SU(2)$ and its corresponding operators are

$$S_+ = K_{21},\ S_- = K_{12},\ S_z = \frac{1}{2}\left(K_{22} - K_{11}\right) \tag{1.54}$$

with S_α the collective operators of the spin chain. The Hamiltonian in this case would correspond to an homogeneous magnetic field

$$H = \varepsilon_1 K_{11} + \varepsilon_2 K_{22} = \frac{L}{2}\left(\varepsilon_1 + \varepsilon_2\right) + \left(\varepsilon_2 - \varepsilon_1\right) S^z. \tag{1.55}$$

We assume that the system is weakly coupled to its environment, satisfying Markovian conditions. Its evolution is thus given by the Lindblad master equation

$$\mathcal{L}(\rho) = -i\left[H, \rho\right] + \sum_{\alpha\beta=1}^{N} \left[W_{\alpha\beta} \rho W_{\alpha\beta}^\dagger - \frac{1}{2} \rho W_{\alpha\beta}^\dagger W_{\alpha\beta} - \frac{1}{2} W_{\alpha\beta}^\dagger W_{\alpha\beta} \right], \tag{1.56}$$

with the collective jump operators $W_{\alpha\beta} = \sqrt{x_{\alpha\beta}} K_{\alpha\beta}$. In the vectorized space (1.48), the Liouvillian reads

$$\mathcal{L} = -i \sum_{\alpha=1}^{N} \varepsilon_\alpha \left(K_{\alpha\alpha} - \overline{J}_{\alpha\alpha} \right) + \sum_{\alpha,\beta=1}^{N} x_{\alpha\beta} \left[K_{\alpha\beta} \overline{J}_{\alpha\beta} - \frac{1}{2} \left(K_{\beta\alpha} K_{\alpha\beta} + \overline{J}_{\beta\alpha} \overline{J}_{\alpha\beta} \right) \right]. \tag{1.57}$$

with $\overline{J}_{\alpha\beta} = I \otimes K_{\alpha\beta}$ the operators in the dual space. In order to translate the Liouvillian into a RG model it is helpful to perform the canonical mapping of the dual operators $J_{\alpha\beta} = -\overline{J}_{\beta\alpha}$, for which the Liouvillian becomes

$$\mathcal{L} = -i \sum_{\alpha=1}^{N} \varepsilon_\alpha \left(K_{\alpha\alpha} + J_{\alpha\alpha} \right) - \sum_{\alpha,\beta=1}^{N} x_{\alpha\beta} \left[K_{\alpha\beta} J_{\beta\alpha} + \frac{1}{2} \left(K_{\beta\alpha} K_{\alpha\beta} + J_{\beta\alpha} J_{\alpha\beta} \right) \right]. \tag{1.58}$$

This Liouvillian has a set of N conserved quantities that define N weak symmetries of the system, $[\mathcal{L}, S_\alpha] = 0$, given by the operators

$$S_\alpha = K_{\alpha\alpha} - \overline{J}_{\alpha\alpha} = K_{\alpha\alpha} + J_{\alpha\alpha}, \quad \alpha = 1, \ldots, N. \tag{1.59}$$

Their eigenvalues s_α are bounded by the constraints $-L \leq s_\alpha \leq L$ and $\sum_\alpha s_\alpha = 0$ and label the different subspaces in which the density matrix subspace is divided.

The Liouvillian (1.56) is, in general, non integrable. However, for a specific set of jump operators we will prove that it belongs to the family of $SU(N)$ RG models

$$x_{\alpha\beta} = \begin{cases} \Gamma_0 & \text{for } \alpha = \beta \\ \Gamma\,(1-p) & \text{for } \alpha > \beta, \\ \Gamma\,(1+p) & \text{for } \alpha < \beta \end{cases} \tag{1.60}$$

with Γ and Γ_0 real positive numbers that define the dissipation rate and $p \in [-1, 1]$ represents an imbalance in the raising and lowering operators. This set of jumps leaves the Liouvillian as a sum of a conserved part and a RG term

$$\mathcal{L} = \mathcal{L}_{\mathrm{C}} + \mathcal{L}_{\mathrm{RG}}, \tag{1.61}$$

with

$$\mathcal{L}_{\mathrm{C}} = -\mathrm{i} \sum_{\alpha} \varepsilon_\alpha \left(K_{\alpha\alpha} + J_{\alpha\alpha} \right) - \Gamma C^2 + \frac{\Gamma - \Gamma_0}{2} \sum_{\alpha} \left(K_{\alpha\alpha} + J_{\alpha\alpha} \right)^2 \tag{1.62}$$

and

$$\begin{aligned}\mathcal{L}_{\mathrm{RG}} = \frac{\Gamma p}{2}\sum_{\alpha}\left(N+1-2\alpha\right)\left(K_{\alpha\alpha}-J_{\alpha\alpha}\right) - \Gamma\sum_{\alpha}K_{\alpha\alpha}J_{\alpha\alpha} \\ -\Gamma\left(1-p\right)\sum_{\alpha>\beta}K_{\alpha\beta}J_{\beta\alpha} - \Gamma\left(1+p\right)\sum_{\alpha<\beta}K_{\alpha\beta}J_{\beta\alpha}.\end{aligned} \tag{1.63}$$

The former term is a conserved quantity that depends on the values of the operators S_α and the quadratic Casimir C^2, while the latter, as we will see in the next section, can be written as a linear combination of the IOM of the trigonometric $SU(N)$ RG models.

1.5.1 Trigonometric $SU(N)$ RG models

For M copies of the $SU(N)$ algebra, the IOM of the Richardson-Gaudin $SU(N)$ model are

$$\begin{aligned}R_m = \sum_{\alpha=1}^{N}\chi_\alpha K_{\alpha\alpha m} + \sum_{n(\neq m)}^{M}\Bigg[Z_{nm}\sum_{\alpha=1}^{M}K_{\alpha\alpha m}K_{\alpha\alpha n} \\ + \sum_{\beta>\alpha}\left(X_{nm}K_{\alpha\beta m}K_{\beta\alpha n} + X^*_{nm}K_{\beta\alpha m}K_{\alpha\beta n}\right)\Bigg],\end{aligned} \tag{1.64}$$

with χ_α a set of N free parameters, $K_{\alpha\beta m}$ the generators $K_{\alpha\beta}$ of the m-th copy and the matrices X, Z

$$X_{mn} = \frac{e^{i(z_n - z_m)}}{\sin\left(z_n - z_m\right)}, \quad Z_{mn} = \cot\left(z_n - z_m\right), \tag{1.65}$$

where z_m is a set of M free parameters. These IOM commute with each other, $[R_m,\, R_m] = 0$, with the two Casimirs of each copy of $SU(N)$ and with the conserved quantities

$$S_\alpha = \sum_{\alpha=1}^{M}K_{\alpha\alpha m}. \tag{1.66}$$

In the case of $M = 2$, for which one copy can be made to belong to the original space and the other to the dual space, these operators correspond to the conserved quantities $S_\alpha = \sum_\alpha K_{\alpha\alpha} + J_{\alpha\alpha}$ (1.59).

The different Liouvillian eigenstates can be found after defining the irreducible representation of the $SU(N)$ group (a vector space where each element represents an element of the group). For a single copy of $SU(N)$ the basis space vectors are $|k_1, k_2, \ldots, k_N\rangle$, with k_i the number of atoms in the level i. These states can be derived from a reference state $|\Lambda_m\rangle = |L, 0, \ldots, 0\rangle$ with all atoms in the lowest level

$$|k_1, k_2, \ldots, k_N\rangle = \frac{1}{\sqrt{\mathcal{N}_{k_1 \ldots k_N}}} K_{21}^{k_2} K_{31}^{k_3} \cdots K_{N1}^{k_N} \, |L, 0, \ldots, 0\rangle \tag{1.67}$$

with the constraints $0 \leq \sum_{\alpha=2}^{N} k_\alpha \leq L$ and $k_\alpha \geq 0$ and $\mathcal{N}_{k_1 \ldots k_N}$ a normalization constant. For each copy m of the $SU(N)$ algebra, its reference state satisfies

$$K_{\alpha\beta m}|\Lambda_m\rangle = 0, \quad \forall \alpha < \beta. \tag{1.68}$$

It is helpful to analyze the action of the Cartan operator $K_{\alpha\alpha m}$ on the reference state. It is intermediately seen that $|\Lambda_m\rangle$ is an eigenstate of that operator $K_{\alpha\alpha m}|\Lambda_m\rangle = \lambda_{\alpha m}|\Lambda_m\rangle$ and, for the particular reference state that we have chosen, $\lambda_{\alpha m} = \delta_{\alpha,1}$.

The Liouvillian eigenvalues using the above representation for the M copies of $SU(N)$ are

$$r_m = \sum_{\alpha=1}^{N} \chi_\alpha \lambda_{\alpha m} + \sum_{n(\neq m)}^{M} \cot\left(z_n - z_m\right) \sum_{\alpha=1}^{M} \lambda_{\alpha m} \lambda_{\alpha n} + \sum_{\alpha=1}^{N} \left(\lambda_{\alpha m} - \lambda_{\alpha+1,m}\right) \sum_{i=1}^{M_a} \cot\left(z_m - E_i^a\right), \tag{1.69}$$

with E_i^a the pair energies or rapidities of the eigenstates. These are found by solving the RG equations, which, in this case, is a set of $N-1$ coupled equations

$$\sum_{b=1}^{N-1} \sum_{j=1}^{M_b} {}' A_{ba} \cot\left(E_j^b - E_i^a\right) - \sum_{m=1}^{M} \left(\lambda_{am} - \lambda_{a+1,m}\right) \cot\left(z_m - E_i^a\right) = \chi_a - \chi_{a+1}, \quad a = 1, \ldots, N-1, \tag{1.70}$$

with $A_{ab} = 2\delta_{ab} - \delta_{a+1,b} - \delta_{a-1,b}$ and where the primed sum excludes the terms $i = j$ when $a = b$. The number of rapidities E_j^a inside each set a is

$$M_a = \sum_{\beta=1}^{a} \left(\sum_{m=1}^{L} \lambda_{\beta m} - s_\beta \right), \tag{1.71}$$

with s_α the expectation values of the conserved quantity S_α (1.66).

Deriving the $SU(N)$ Liouvillian from the integrals of motion

If there are two copies of the $SU(N)$ algebra, $M = 2$, the $SU(N)$ Liouvillian (1.56) can be written as a linear combination of the IOM with one copy belonging to the original space and the other to the dual space. Because the z_m are a set of free parameters of the IOM (1.64), we choose $(z_1,\, z_2) = (0,\, z)$ and the two IOM are

$$\begin{aligned} R_1 = &\sum_{\alpha=1}^{N} \chi_\alpha K_{\alpha\alpha 1} + \cot z \sum_{\alpha=1}^{N} K_{\alpha\alpha 1} K_{\alpha\alpha 2} \\ &+ \sum_{\beta>\alpha}^{N} \frac{1}{\sin z} \left(e^{iz} K_{\alpha\beta 1} K_{\beta\alpha 2} + e^{-iz} K_{\beta\alpha 1} K_{\alpha\beta 2} \right) \\ R_2 = &\sum_{\alpha=1}^{N} \chi_\alpha K_{\alpha\alpha 2} - \cot z \sum_{\alpha=1}^{N} K_{\alpha\alpha 1} K_{\alpha\alpha 2} \\ &- \sum_{\beta>\alpha}^{N} \frac{1}{\sin z} \left(e^{iz} K_{\alpha\beta 1} K_{\beta\alpha 2} + e^{-iz} K_{\beta\alpha 1} K_{\alpha\beta 2} \right) \end{aligned} \tag{1.72}$$

with the correspondence to the vectorized space $K_{\alpha\beta 1} = K_{\alpha\beta},\ K_{\alpha\beta 2} = J_{\alpha\beta}$. The RG Liouvillian (1.56) is then the following linear combination

$$\mathcal{L}_{\text{RG}} = g \sin{(z)} \left(R_1 - R_2 \right). \tag{1.73}$$

with the parameters

$$\cot z = \frac{i}{p}, \quad g = \frac{\Gamma\sqrt{1-p^2}}{2}, \quad \chi_\alpha = i\left(2\alpha - N - 1\right). \tag{1.74}$$

The eigenvalues of the RG terms of the Liouvillian (1.56) are

$$l_{\text{RG}} = g\sin{(z)}\left(r_1 - r_2\right) = -i\frac{L\Gamma p}{2}\left[\sum_{i=1}^{M_1} \cot E_i^1 + \sum_{i=1}^{M_{N-1}} \cot\left(z - E_i^{N-1}\right)\right], \tag{1.75}$$

which, together with the constant terms, define the complete eigenvalue spectrum of the Liouvillian in terms of the rapidities E_i^a

$$l = l_{\text{C}} + l_{\text{RG}} = -i\sum_\alpha \varepsilon_\alpha s_\alpha - \Gamma C^2 + \frac{\Gamma - \Gamma_0}{2}\sum_\alpha s_\alpha^2 + l_{\text{RG}}. \tag{1.76}$$

1.5.2 $SU(2)$ Richardson-Gaudin models

For $N = 2$ level atom systems the Liouvillian is related to the integrable model derived by Ribeiro and Prosen [14] for a $SU(2)$ collective spin under a local magnetic field

$$H = -hS^z \tag{1.77}$$

and collective jump operators

$$W_0 = \sqrt{4\Gamma_0} S_z, \quad W_\pm = \sqrt{\Gamma\,(1 \mp p)} S_\pm. \tag{1.78}$$

The Ribeiro-Prosen Liouvillian in the vector representation is

$$\begin{aligned}\mathcal{L}_{\mathrm{RP}} = ih(S_z - \bar{J}_z) &+ 4\Gamma_0 \left[S_z \bar{J}_z - \frac{1}{2}\left(S_z^2 + \bar{J}_z^2\right)\right] \\ &+ \Gamma(1-p)\left[S_+\bar{J}_+ - \frac{1}{2}\left(S_-S_+ + \bar{J}_-\bar{J}_+\right)\right] \\ &+ \Gamma(1+p)\left[S_-\bar{J}_- - \frac{1}{2}\left(S_+S_- + \bar{J}_+\bar{J}_-\right)\right].\end{aligned} \tag{1.79}$$

with the spin operators related to the $SU(2)$ generators by

$$S_+ = K_{21},\ S_- = K_{12},\ S_z = \frac{1}{2}\left(K_{22} - K_{11}\right)$$

This Liouvillian is equivalent to the $SU(2)$ Liouvillian (1.61) for $(\varepsilon_1,\, \varepsilon_2) = (-h/2,\, h/2)$ and a constant energy shift of the symmetry sectors s_α

$$\mathcal{L}_{\mathrm{RP}} = \mathcal{L}_{SU(2)} + \Gamma_0 s_1 s_2. \tag{1.80}$$

Thus, the Liouvillian derived in this work is the generalization of the Ribeiro-Prosen model for higher $SU(N)$ algebras.

1.5.3 $SU(3)$ Richardson-Gaudin models

For $N = 3$ there are two sets of rapidities E_i^1 and E_i^2, which are the solution of the RG equations (1.70)

$$\begin{aligned}-2i &= \sum_{j(\neq i)}^{M_1} \cot\left(E_j^1 - E_i^1\right) - \sum_{j}^{M_2} \cot\left(E_j^2 - E_i^1\right) + L\cot\left(E_i^1\right) \\ -2i &= \sum_{j(\neq i)}^{M_2} \cot\left(E_j^2 - E_i^2\right) - \sum_{j}^{M_1} \cot\left(E_j^1 - E_i^2\right) - L\cot\left(z - E_i^2\right),\end{aligned} \tag{1.81}$$

with $M_1 = L - s_1$ and $M_2 = L + s_3$. By mapping $e_i = \cot E_i^1$, $\omega_i = \cot E_i^2$, the RG equations are written in a simpler form

$$
\begin{aligned}
0 &= \sum_{j(\neq i)}^{M_1} \frac{2}{e_i - e_j} - \sum_{j}^{M_2} \frac{1}{e_i - \omega_j} + \frac{Q_+^e}{e_i - i} + \frac{Q_-^e}{e_i + i} \\
0 &= \sum_{j(\neq i)}^{M_2} \frac{2}{\omega_i - \omega_j} - \sum_{j}^{M_1} \frac{1}{\omega_i - e_j} + \frac{Q_+^\omega}{\omega_i - i} + \frac{Q_-^\omega}{\omega_i + i} - \frac{L}{\omega_i - i/p},
\end{aligned}
\tag{1.82}
$$

where the effective charges Q are

$$
\begin{aligned}
Q_+^e &= 2 + \frac{s_1 - s_2}{2}, \quad Q_-^e = \frac{s_1 - s_2}{2} \\
Q_+^\omega &= 2 + \frac{s_2 - s_3}{2}, \quad Q_-^\omega = \frac{s_2 - s_3}{2}.
\end{aligned}
\tag{1.83}
$$

These equations can be interpreted in terms of an electrostatic-like problem in the complex plane, where the sets of parameters e_i and ω_i would represent two sets of particles with opposite charge. These particles are either repelled from or attracted to the quasi-charges $Q_\pm^{e,\omega}$ depending on the sign of the charge, which are located at the points $(0, \pm 1)$ in the plane. In addition, the ω_i particles are attracted to another charge of magnitude L at position $(0, 1/p)$. It is interesting to note that p is the only Liouvillian parameter that appears in the RG equations.

Steady state of the $SU(3)$ RG model

As we have seen, the steady state of a Liouvillian belongs to a physical density matrix and is thus hermitian. The only subspace defined by the weak Liouvillian symmetries (s_1, s_2, s_3) that has hermitian density matrices is the one with every $s_\alpha = 0$, so the steady state must belong to the $(0, 0, 0)$ sector. For the spectral parameters of the RG equations, this implies that, for a system of size L, the number of parameters e_i, ω_i is $M_1 = M_2 = L$ and the effective charges are $Q_+^e = Q_+^\omega = 2$ and $Q_-^e = Q_-^\omega = 0$

Figure 1.1 shows the spectral parameters e_i, ω_i of the steady state for a system of size $L = 40$ with respect to different values of $p = (0.1, 0.2, 0.25)$. The spectral parameters are distributed around a circle with center at the charge of magnitude $+L$ located at $(0, 1/p)$. The radius r of this circle is given by the distance between its center and the charges $Q_+^{e,\omega}$, $r = |1 - 1/p|$.

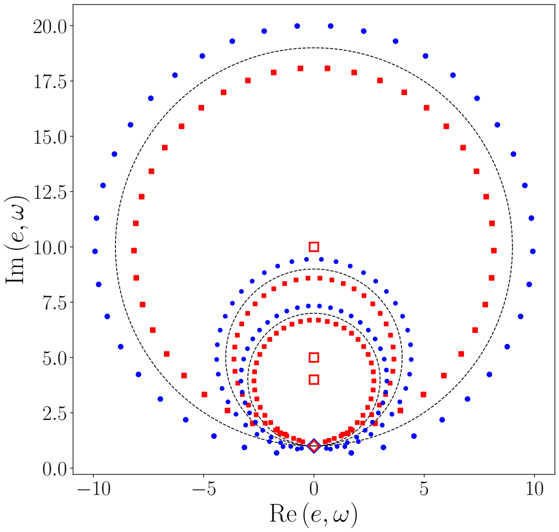

Figure 1.1: Spectral parameters e_i (blue dots) and ω_i (red squares) of the steady state of the $SU(3)$ Liouvillian with respect to $p = (0.1,\, 0.2,\, 0.25)$. The circle around which the spectral parameters are positioned is illustrated by the dashed line and its center is positioned at $(0,\, 1/p)$, marked by the red hollow squares. The charges $Q_+^{e,\omega} = +2$ are shown as blue and red diamonds, while the charges $Q_-^{e,\omega} = 0$ are not shown.

At the base of the circle the parameters are repelled by these charges, with magnitude $Q_+^{e,\omega} = +2$, although this is a small repulsion compared with the central charge $+L$ and, thus, all parameters are positioned almost uniformly around the circle.

We note that the distribution of the spectral parameters is universal in the sense that it only depends on the Liouvillian parameter p, which determines the radius and center of the circle. In the limit $p \to 1$, this circle shrinks to the point $(0,\, 1)$ and all parameters collapse to $e_i = \omega_i = 1$, while, in the limit $p \to 0$, the circle grows unbounded and the parameters have infinite modulus.

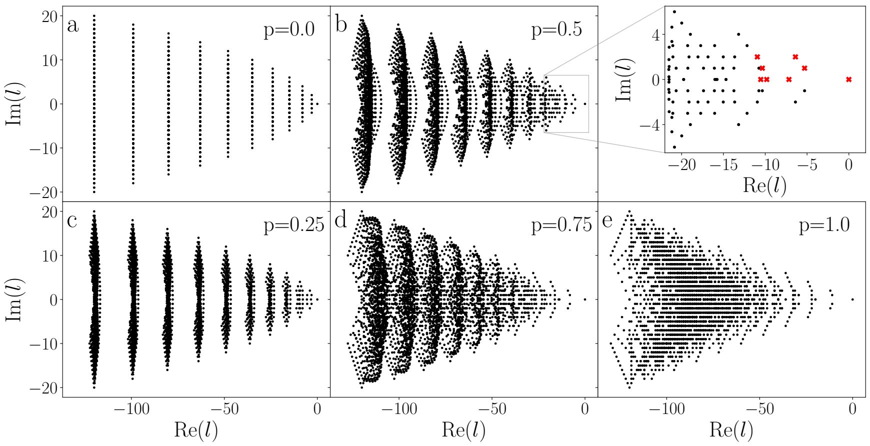

Figure 1.2: Full Liouvillian spectrum with respect to different values of p. (Inset of b) Eigenvalues near the line $\mathrm{Re}\{l\} = 0$. The red crosses mark the analysed eigenstates shown in Figure 1.3.

Full Liouvillian spectrum

The Liouvillian eigenvalues of each symmetry sector $(s_1,\, s_2,\, s_3)$ are determined by the eigenvalues of the two Liouvillian terms $\mathcal{L} = \mathcal{L}_{\mathrm{C}} + \mathcal{L}_{\mathrm{RG}}$ (1.61). The second term is a real non symmetric operator, so its eigenvalues are either real or complex conjugate pairs, while the first term is a constant term and displaces the eigenvalues by a constant imaginary term $\mathrm{Im}\{\mathcal{L}_{\mathrm{C}}\} = -i\sum_\alpha \varepsilon_\alpha s_\alpha$. Therefore, the eigenvalues of each symmetry sector are located around horizontal lines in the complex plane with a mean imaginary part given by $\mathrm{Im}\{\mathcal{L}_{\mathrm{C}}\}$.

The complete spectrum consists of complex conjugate pairs of eigenvalues, where the eigenvalues of the sector $(s_1\, s_2,\, s_3)$ correspond to the conjugate eigenvalues of the sector $(-s_1,\, -s_2,\, -s_3)$. This reinforces the argument that the steady state is in the sector $(0, 0, 0)$. In addition, our computations show that the dissipative gap or the slowest decaying eigenstate is always in the sector with $\max\{s_\alpha\} = 1$.

We show in Figure 1.2 the full Liouvillian spectrum with $L = 10$, $\Gamma = \Gamma_0 = 1$, $(\varepsilon_1,\, \varepsilon_2,\, \varepsilon_3) = (-1,\, 0,\, 1)$ and with respect to different values of the parameter p. At $p = 0$ there is an additional symmetry given by the quadratic

Casimir operator $C^2 = \sum_{\alpha\beta} \left(K_{\alpha\beta} + J_{\alpha\beta}\right) \left(K_{\beta\alpha} + J_{\beta\alpha}\right)$ and the Liouvillian is

$$\mathcal{L} = -i \sum_{\alpha} \varepsilon_\alpha s_\alpha + \frac{\Gamma - \Gamma_0}{2} \sum_{\alpha} S_\alpha^2 - \Gamma \frac{C^2}{2}. \tag{1.84}$$

For $\Gamma = \Gamma_0$, the real part of the eigenvalues is defined only by the total Casimir and, as can be seen in Figure 1.2(a), it divides the spectrum into vertical columns whose real value is given by the Casimir eigenvalues $c^2 = 2\left(\lambda^2 + 2\lambda\right),\ \lambda = 0, 1, \ldots, L$. As the value of p is increased, these columns are no longer defined by a symmetry operator and their eigenvalues start to break apart.

The Liouvillian spectrum can also be understood with the spectral parameters e, ω that define its eigenstates. We show in Figure 1.3 the spectral parameters corresponding to each of the eigenstates indicated in the Inset of Figure 1.2(b) for a system of size $L = 10$ with $\Gamma = \Gamma_0 = 1$, $\varepsilon_\alpha = (-1, 0, 1)$ and $p = 0.5$. These eigenstates are slow decaying modes and their spectral parameters are close to the ones of the steady state, shown in Figure 1.3(a). As the sectors s_α start to diverge from zero, the effective charges $Q_-^{e,\omega}$ acquire a non zero magnitude, which either attracts the spectral parameters, as in Figures 1.3(b,f,h), or repels them, as in Figures 1.3(b,c,f,h). As the absolute value of s_α becomes larger, some parameters can even collapse in the neighbourhood of an effective charge, like in Figure 1.3(h).

Thermodynamic limit of N-level atom systems

We can compute the steady state and dissipative gap of the Liouvillian for a system of N-level atoms in the thermodynamic limit by mapping the $SU(N)$ generators to Schwinger bosons [68, 69]

$$K_{\alpha\beta} = a_\alpha^\dagger a_\beta, \quad \overline{J}_{\alpha\beta} = b_\alpha^\dagger b_\beta, \tag{1.85}$$

with the restriction that

$$\sum_{\alpha} a_\alpha^\dagger a_\alpha = \sum_{\alpha} b_\alpha^\dagger b_\alpha = L. \tag{1.86}$$

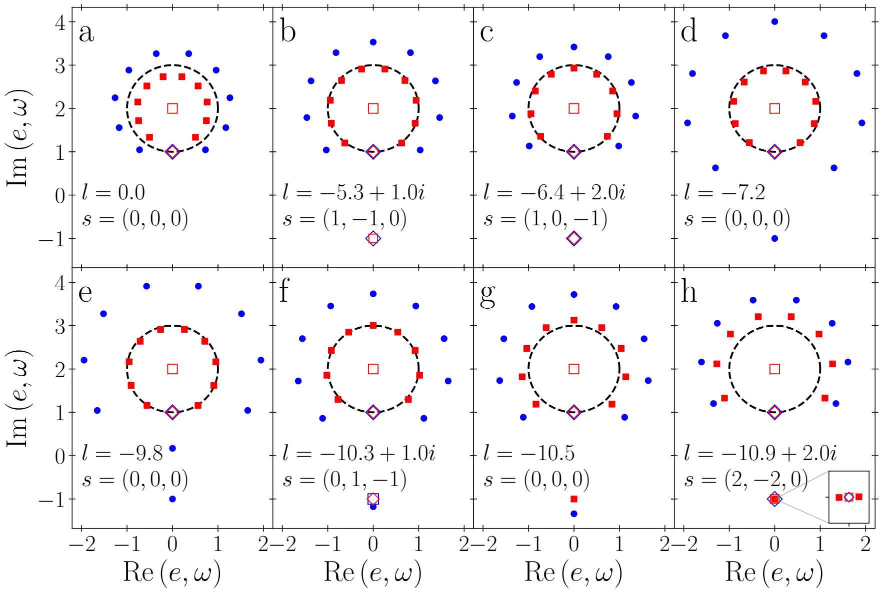

Figure 1.3: Spectral parameters e_i (blue dots) and ω_i (red squares) of the slow decaying eigenstates shown in the Inset of Figure 1.2(b). The effective charges are illustrated by hollow squares (attractive) and diamonds (repulsive). The effective charges seen by the e_i parameters are blue, while the charges seen by ω_i are red. (Inset of h) Zoom around the neighbourhood of a charge at $(0,-1)$.

In terms of the Schwinger bosons, the Liouvillian is

$$\begin{aligned}\mathcal{L} = &-\sum_{\alpha=1}^{N}\left(i\varepsilon_\alpha + \mu_a\right) a_\alpha^\dagger a_\alpha + \sum_{\alpha=1}^{N}\left(i\varepsilon_\alpha - \mu_b\right) b_\alpha^\dagger b_\alpha - \frac{\gamma}{L} C^2 \\ &+ \frac{\gamma-\gamma_0}{2L}\sum_\alpha \left(a_\alpha^\dagger a_\alpha - b_\alpha^\dagger b_\alpha\right)^2 + \frac{\gamma}{L}\sum_\alpha a_\alpha^\dagger a_\alpha b_\alpha^\dagger b_\alpha \\ &+ \frac{\gamma}{L}\left(1-p\right)\sum_{\alpha>\beta} a_\alpha^\dagger a_\beta b_\alpha^\dagger b_\beta + \frac{\gamma}{L}\left(1+p\right)\sum_{\alpha<\beta} a_\alpha^\dagger a_\beta b_\alpha^\dagger b_\beta \\ &+ \frac{\gamma p}{2L}\sum_\alpha \left(N+1-2\alpha\right)\left(a_\alpha^\dagger a_\alpha + b_\alpha^\dagger b_\alpha\right),\end{aligned} \tag{1.87}$$

where $\gamma = \Gamma L$ and $\gamma_0 = \Gamma_0 L$ are the rescaled dissipation strengths and the chemical potential $\mu_{a,b}$ preserves the total number of particles for each copy of $SU(N)$.

For the steady state in the thermodynamic limit we propose a coherent state ansatz

$$\begin{aligned} |\Psi\rangle =& \exp\left[\sqrt{L}\sum_{\alpha=1}^{N}\left(A_\alpha a_\alpha^\dagger + B_\alpha b_\alpha^\dagger\right)\right]|0\rangle \\ \langle\overline{\Psi}| =& \langle 0|\exp\left[\sqrt{L}\sum_{\alpha=1}^{N}\left(\overline{A}_\alpha a_\alpha + \overline{B}_\alpha b_\alpha\right)\right], \end{aligned} \tag{1.88}$$

with $|\Psi\rangle$ and $\langle\overline{\Psi}|$ the right and left Liouvillian eigenstates, respectively. The parameters A_α, $\overline{A}_\alpha$, B_α, $\overline{B}_\alpha$ are a set of variational parameters that are chosen so that the eigenvalue of the steady state is zero in the thermodynamic limit, $\lim_{L\to\infty}\langle\overline{\Psi}|\mathcal{L}|\Psi\rangle = 0$. These two coherent states are the vacuum of the shifted boson operators

$$c_\alpha|\Psi\rangle = d_\alpha|\Psi\rangle = 0, \quad \langle\overline{\Psi}|\overline{c}_\alpha = \langle\overline{\Psi}|\overline{c}_\alpha = 0, \quad [c_\alpha, \overline{c}_\beta] = \left[d_\alpha, \overline{d}_\beta\right] = 0, \tag{1.89}$$

with

$$\begin{aligned} a_\alpha &= \sqrt{L}A_\alpha + c_\alpha, & a_\alpha^\dagger &= \sqrt{L}\overline{A}_\alpha + \overline{c}_\alpha \\ b_\alpha &= \sqrt{L}B_\alpha + d_\alpha, & b_\alpha^\dagger &= \sqrt{L}\overline{B}_\alpha + \overline{d}_\alpha. \end{aligned} \tag{1.90}$$

Note that the hatted creation operators are not the hermitian conjugate of the annihilation operators because the Liouvillian is not hermitian.

The Liouvillian (1.87) written in terms of the shifted boson operators can be expanded in orders of L

$$\mathcal{L} = L\mathcal{L}_1 + \sqrt{L}\mathcal{L}_{1/2} + \mathcal{L}_0 + \mathcal{O}\left(L^{-1/2}\right). \tag{1.91}$$

It is easy to show that the choice A_α, $\overline{A}_\alpha$, B_α, $\overline{B}_\alpha = \delta_{\alpha,\eta}$ with $\eta = 1, \ldots, N$ an arbitrary atomic level and $\mu_a = \gamma - i\varepsilon_\eta$, $\mu_b = \gamma + i\varepsilon_\eta$ makes the first two terms zero, $\mathcal{L}_1 = \mathcal{L}_2 = 0$. The other term left, $\mathcal{L}_0$, is

$$
\begin{aligned}
\mathcal{L}_0 = & \sum_{\alpha(\neq\eta)} \left(i\varepsilon_\alpha - i\varepsilon_\eta - \gamma\right) \overline{d}_\alpha d_\alpha - \sum_{\alpha(\neq\eta)} \left(i\varepsilon_\alpha - i\varepsilon_\eta + \gamma\right) \overline{c}_\alpha c_\alpha - \gamma\left(N-1\right) \\
& + \gamma p \left(N + 1 - 2\eta\right) + \gamma\left(1-p\right) \sum_{\alpha(>\eta)} \overline{c}_\alpha \overline{d}_\alpha + \gamma\left(1+p\right) \sum_{\alpha(<\mu)} \overline{c}_\alpha \overline{d}_\alpha \\
& + \gamma\left(1-p\right) \sum_{\alpha(<\eta)} c_\alpha d_\alpha + \gamma\left(1+p\right) \sum_{\alpha(>\eta)} c_\alpha d_\alpha,
\end{aligned}
\tag{1.92}
$$

which has only quadratic operators and, therefore, can be diagonalized with a non unitary Bogoliubov transformation

$$
\begin{aligned}
e_\alpha &= u_\alpha c_\alpha - v_\alpha \overline{d}_\alpha, \quad & f_\alpha &= u_\alpha d_\alpha - v_\alpha \overline{c}_\alpha \\
\overline{e}_\alpha &= \overline{u}_\alpha \overline{c}_\alpha - \overline{v}_\alpha d_\alpha, \quad & \overline{f}_\alpha &= \overline{u}_\alpha \overline{d}_\alpha - \overline{v}_\alpha c_\alpha,
\end{aligned}
\tag{1.93}
$$

with $u_\alpha \overline{u}_\alpha - v_\alpha \overline{v}_\alpha = 1$. These operators define the quasiparticle excitations on top of the coherent state. The diagonalized Liouvillian is

$$
\mathcal{L}_0 = C_\eta + \sum_{\alpha(\neq\eta)} \overline{e}_\alpha e_\alpha \Big[-i\left(\varepsilon_\alpha - \varepsilon_\eta\right) - |p|\gamma \Big] + \overline{f}_\alpha f_\alpha \Big[i\left(\varepsilon_\alpha - \varepsilon_\eta\right) - |p|\gamma \Big], \tag{1.94}
$$

with $C_\eta = 0$ if $p > 0$ and $\eta = 1$ or if $p < 0$ and $\eta = N$. For the coherent state ansatz

$$
\langle \overline{\Psi} | \mathcal{L}_0 | \Psi \rangle = C_\eta. \tag{1.95}
$$

Therefore, if the conditions for $C_\eta \equiv 0$ are met, the coherent state (1.88) is the steady state and its eigenvalue is zero in the thermodynamic limit. The slowest decaying eigenstates are built by adding one e_α or f_α quasiparticle to the coherent state, and their energy is $-|p|\gamma \pm i\left(\varepsilon_\alpha - \varepsilon_\eta\right)$. Thus, the dissipative gap Δ of the $SU(N)$ model in the thermodynamic limit is $|p|\gamma$. Interestingly, all quasiparticle excitations have the same real gap, so there are $2(N-1)$ slowest eigenstates that decay at the same rate.

We show in Figure 1.4 the extrapolation to the thermodynamic limit of the rescaled dissipative gap Δ/L for finite system sizes L with $N = 3$ computed with exact diagonalization. The computations are done with $\Gamma = \Gamma_0 = 1$, $p = \{0.25,\, 0.5,\, 0.75\}$ and in two symmetry sectors $(1,-1,0)$, $(1,0,-1)$. The extrapolation is done by fitting the results to a second order polynomial $f(L) = \sum_{m=0}^{2} c_m (1/L)^m$. The fitted polynomial for the two analysed

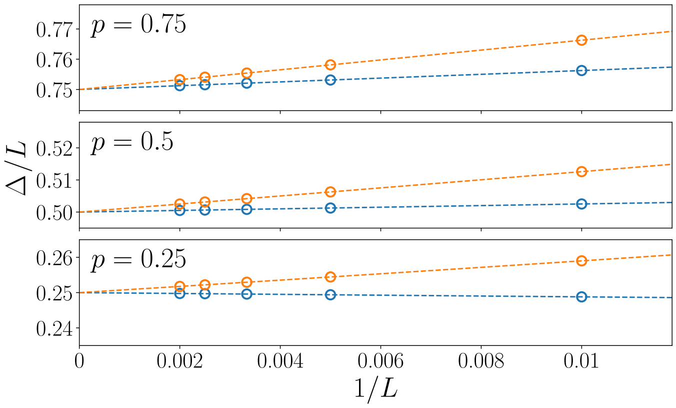

Figure 1.4: Rescaled dissipative gap with respect to the inverse system size $1/L$. The gaps are shown for $p = \{0.25,\, 0.5,\, 0.75\}$ and inside different symmetry sectors $s_\alpha = (1,-1,0)$ (blue) and $(1,0,-1)$ (orange). The dashed lines illustrate the fitting polynomial.

symmetry sectors are

$$\begin{aligned} s = (1,-1,0): &\quad \frac{\Delta}{L} = p\,\Gamma - \frac{\Gamma}{L}\left(\frac{1}{2} - \frac{3p}{2}\right) + \mathcal{O}\left(\frac{1}{L^2}\right) \\ s = (1,0,-1): &\quad \frac{\Delta}{L} = p\,\Gamma - \frac{\Gamma}{L}\left(-\frac{1}{2} - \frac{3p}{2}\right) + \mathcal{O}\left(\frac{1}{L^2}\right). \end{aligned} \tag{1.96}$$

This confirms our derivation of $\Delta = |p|\gamma$ in the thermodynamic limit using coherent states.

1.5.4 Conclusions

Using the $SU(N)$ Richardson-Gaudin integrals of motion we derived an novel integrable Liouvillian for collective systems of N-level atoms. Interestingly, this Liouvillian represents the generalization to $SU(N)$ of the previously derived Ribeiro-Prosen [14] Liouvillian. We analysed the more complex case of $SU(3)$ systems and showed the electrostatic interpretation of the RG equations and the spectral parameters of the exact eigenstates. We studied the general form of the complete spectrum and were able to derive a coherent state ansatz that lets us study the thermodynamic limit behaviour of the model.

1.6 From integrability to chaos in quantum Liouvillians

The results from this section are reported in our article: *From integrability to chaos in quantum Liouvillians* [22].

The topic of quantum chaos is of great relevance for its connections with quantum thermalization, quantum information and non equilibrium dynamics [70–74]. For closed quantum systems, described by hermitian Hamiltonians, the dynamics of the system can be classified through its spectral statistics [75]. The eigenvalues of integrable closed systems are dispersed independent of each other and their spacing distribution, or the distribution of the first neighbour distances between eigenvalues, is a 1D Poisson distribution $P(s) = e^{-s}$. On the other hand, chaotic systems have spectral statistics characterized by level repulsion and the spacing distribution is close to the Wigner surmise of Random Matrix Theory, although their distribution also depends on the symmetry class of the system, with $P(s) \sim s^{\beta}$ and $\beta = 1, 2, 4$ for orthogonal, unitary and symplectic matrices [76]. This conjecture, the Bohigas-Gianoni-Schmit (BGS) conjecture, has been extensively tested for closed quantum systems [77–79] and is well founded in semiclassical theory [74, 80, 81]. With respect to the transition from integrable to chaotic dynamics, it depends on the characteristics of the system and is non universal.

While in open quantum systems the first studies of the spectral statistics [82] came shortly after the BGS conjecture, the theory is not so well developed. In their early work, Grobe *et al.* [82] studied a system where the Hamiltonian transitioned from integrability to chaos, while the jumps remained independent. They found that the spacing distribution in the integrable regime was close to a 2D Poisson distribution, while the chaotic regime presented cubic repulsion of the eigenvalues $P(s) \sim s^3$. Similar level repulsions are also found in the Ginibre ensemble of non hermitian random matrices [19], although their details depend on the symmetry class of the matrices [17, 18]. Recently, this transition has been studied on an open spin chain that is Bethe ansatz integrable in one of its limits [20] and the other limits belonged to the Ginibre class of non hermitian matrices. The spectral statistics were fitted by a static 2D Coulomb gas with harmonic confinement, whose level repulsion is given by the inverse temperature, showing fractional level repulsion inside the transition.

The discovery of new integrable Liouvillians [13, 14] paves the way to the study of the dynamics in open quantum systems. While the spectral statistics of random Liouvillians has been studied in several works [15, 16], the transition from integrable systems has not yet been extensively studied. The inclusion of new classes of integrable Liouvillians and transition Liouvillians can help bridge this knowledge.

In this section we will introduce a Richardson-Gaudin Liouvillian that can transition between two classes of integrability. We will also interpolate this with a Liouvillian with random Lindblad jumps that presents chaotic level statistics. The interpolation between both regimes in terms of only one parameter allows us to study the complete transition between integrable and chaotic statistics, which is characterized using the level spacing distribution of the Liouvillian eigenvalues and the average values of the complex spacing ratios [83]. Our results show a good agreement of the integrable spacing distribution with the 2D Poisson distribution and also a good agreement of the chaotic spectra with the distribution of the $AI^\dagger$ universality class of non hermitian random matrices [17, 18], which is the one to which our Liouvillians belong. These results are corroborated by the spacing distribution and the complex spacing ratios measurements. Finally, using these measurements we are also able to characterize the complete transition between the two dynamic regimes.

1.6.1 Family of integrable and chaotic Liouvillians

We study a chain of L spins of arbitrary magnitude s_i inside an inhomogeneous magnetic field

$$H = \sum_{i=1}^{L} h_i S_i^z, \tag{1.97}$$

with an interaction with the environment mediated by collective jumps of the form

$$L_z^a = \sqrt{2\Gamma_0} \sum_{i=1}^{L} z_i^a S_i^z, \quad L_\pm = \sqrt{\Gamma_\pm} \sum_{i=1}^{L} x_i S_i^\pm, \tag{1.98}$$

where there are several dephasing jumps S^z labelled by the index a. The dissipation strengths of the gain and loss operators $L_\pm$ must be equivalent $\Gamma_+ = \Gamma_- = \Gamma$ in order to result in an integrable Liouvillian, although this condition can be relaxed for a single collective spin [14]. With this choice, the jumps are hermitian $(L_z^a)^\dagger = L_z^a$ and $(L_+)^\dagger = L_-$, which results in a trivial steady state $\rho_{\mathrm{SS}} = \mathbb{I}$. The Liouvillian in the vector representation after a rotation of π in the y axis of the dual space is

$$\begin{aligned}\mathcal{L} = &- i\sum_i h_i \left(S_i^z + J_i^z\right) - \Gamma_0 \sum_{a=1}^{n_j} \sum_{ij} z_i^a z_i^a \left(S_i^z + J_i^z\right)\left(S_j^z + J_j^z\right) \\ &- \Gamma \sum_{ij} x_i x_j \frac{1}{2}\left[\left(S_i^+ + J_i^+\right)\left(S_j^- + J_j^-\right) + h.c.\right],\end{aligned} \tag{1.99}$$

where the symmetry of the original S and dual J space spin operators is due to the equivalence of the gain and loss dissipation strengths $\Gamma_+ \equiv \Gamma_-$. This symmetry allows us to define a composite spin operator $K = S + J$, with which the Liouvillian is written as

$$\begin{aligned}\mathcal{L} = &- i\sum_i h_i K_i^z - \Gamma \sum_i x_i^2 \left(K_i\right)^2 + \sum_i \left[\Gamma x_i^2 - \Gamma_0 \sum_a \left(z_i^a\right)^2\right]\left(K_i^z\right)^2 \\ &- \Gamma_0 \sum_{a,i\neq j} z_i^a z_i^a K_i^z K_j^z - \Gamma \sum_{i\neq j} x_i x_j \frac{1}{2}\left(K_i^+ K_j^- + K_i^- K_j^+\right).\end{aligned} \tag{1.100}$$

Because the dual operators J are a copy of S, their magnitudes at each site are equivalent $j_i = s_i$ and, therefore, the magnitude of K at site i can take the values $k_i = 0, 1, \ldots, 2s_i$.

The Liouvillian has a set of $L + 1$ weak symmetries [67] defined by the total angular momentum operator $K^z = \sum_i K_i^z$ and the L $SU(2)$ Casimirs at each site

$$K_i^2 = \left(K_i^z\right)^2 + \frac{1}{2}\left(K_i^+ K_i^- + K_i^- K_i^+\right) = k_i\left(k_i + 1\right). \tag{1.101}$$

The symmetry operators commute among themselves $[K_i^2,\, K_z] = 0$ and, thus, the Liouvillian space is divided into diagonal blocks labelled by the magnetization k_z and the L quantum numbers k_i. In addition, the symmetry of the Liouvillian terms make that its action on a singlet state $k_i = 0$ annihilates that state. Thus, singlets are effectively removed from the system, from which it is derived that the steady state is the one with all singlet spins.

This Liouvillian has an additional symmetry $F = \mathcal{C}e^{i\pi K^x}$, such that $[\mathcal{L},\, F] = 0$, which is possible due to the Hamiltonian being a magnetic field aligned in the z direction. The $e^{i\pi K^x}$ term rotates the spin along x by an angle π and changes the spin sign along the y and z directions, while $\mathcal{C}$ is the complex conjugation operator $\mathcal{C}\, i\, \mathcal{C}^{-1} = -i$. The symmetry operator F, however, does not commute with the K^z operator and, thus, cannot be used to divide the Liouvillian space into further symmetry sectors.

The operator F can be used to understand the form of the Liouvillian spectrum. This operator acting on a Liouvillian eigenstate $|\psi\rangle$ results in another Liouvillian eigenstate $|F\psi\rangle$ with conjugate eigenvalue

$$\mathcal{L}|F\psi\rangle = \mathcal{L}F|\psi\rangle = F\mathcal{L}|\psi\rangle = F\lambda_i|\psi\rangle = \lambda_i^*|F\psi\rangle. \tag{1.102}$$

For eigenstates with real eigenvalue, $\lambda_i \in \mathbb{R}$, the operator F maps the eigenstate onto itself $|F\psi\rangle = |\psi\rangle$. On the other hand, the eigenstate $|F\psi\rangle$ has opposite angular momentum with respect to $|\psi\rangle$

$$\langle F\psi|K^z|F\psi\rangle = \langle\psi|F^\dagger K^z F|\psi\rangle = \langle\psi|(-K^z)|\psi\rangle. \tag{1.103}$$

Thus, the complete Liouvillian spectrum is characterized by pairs of complex conjugate eigenvalues $(\lambda_i,\, \lambda_i^*)$ that correspond to subspaces with opposite angular momentum $(k_{z,i},\, -k_{z,i})$. The subspaces with $k_z = 0$ are already composed of complex pair conjugates.

Integrable and chaotic Liouvillians

The Liouvillian (1.100) can be derived from the Richardson-Gaudin integrals of motion (1.1)

$$R_i = K_i^z - G \sum_{j(\neq i)=1}^{L} \frac{X_{ij}}{2}\left(K_i^+K_j^- + K_j^+K_i^-\right) + Z_{ij}K_i^zK_j^z, \tag{1.104}$$

where the magnitude of the spins k_i is arbitrary. We choose the X, Z matrices to be [58]

$$\begin{aligned} X_{ij} &= \frac{\sqrt{(1-\alpha)+\alpha\,\eta_i^2}\sqrt{(1-\alpha)+\alpha\,\eta_j^2}}{\eta_i-\eta_j} \\ Z_{ij} &= \frac{(1-\alpha)+\alpha\,\eta_i\eta_j}{\eta_i-\eta_j}, \end{aligned} \tag{1.105}$$

where $\alpha \in [0,1]$ is an interpolation variable that ranges from the constant pairing Hamiltonian solved by Richardson [36], $\alpha = 0$, to the separable pairing Hamiltonian [56], $\alpha = 1$. Thus, for $\alpha = \{0,1\}$ the model belongs to the rational or XXX RG family and, between both limits, the Liouvillian belongs to the hyperbolic or XXZ RG family. The Liouvillian is, therefore, integrable for the whole range of α. On the other hand, the $L+1$ parameters $(G,\, \eta_i)$ of the IOM can be chosen arbitrarily and we set $G = ig$ with $g \in \mathbb{R}$ as pure imaginary, so that it results in the unitary evolution part of the Liouvillian $-iK^z$. This choice of G makes the IOM and the Liouvillian non hermitian, but this does not affect its integrability properties and the exact eigenstates can still be solved. The RG Liouvillian with that choice of parameters is

$$\begin{aligned}\mathcal{L}_{\mathrm{RG}} = -i\sum_{i=1}^{L}\eta_i R_i = -i\sum_{i}^{L}\eta_i K_i^z - \frac{g}{2}\sum_{i\neq j}^{L}\left[(1-\alpha)+\alpha\,\eta_i\eta_j\right]K_i^z K_j^z \\ -\frac{g}{2}\sum_{i\neq j}^{L}\sqrt{(1-\alpha)+\alpha\,\eta_i^2}\sqrt{(1-\alpha)+\alpha\,\eta_j^2}\,\frac{1}{2}\left(K_i^+K_j^- + K_i^-K_j^+\right). \quad (1.106)\end{aligned}$$

This Liouvillian can be derived from a spin chain inside an inhomogeneous magnetic field $H = \sum_i \eta_i S_i^z$ and jumps of the form

$$L_\pm = \sqrt{\frac{g}{2}}\sum_{i=1}^{L}\sqrt{(1-\alpha)+\alpha\,\eta_i^2}\,S_i^\pm \qquad (1.107)$$

and

$$L_z^1 = \sqrt{(1-\alpha)\,\frac{g}{2}}\sum_{i=1}^{L}S_i^z, \quad L_z^2 = \sqrt{\alpha\,\frac{g}{2}}\sum_{i=1}^{L}\eta_i S_i^z, \qquad (1.108)$$

where two dephasing jumps are needed in order to construct the Liouvillian.

We can study the spectral properties of the integrable to chaotic transition by interpolating the integrable Liouvillian with a chaotic one built from random Lindblad jumps

$$L_\pm^a = \sqrt{\Gamma}\sum_{i=1}^{L}w_i^a S_i^\pm, \quad a = 1,\ldots,n_j, \qquad (1.109)$$

where $\mathbf{w}^a$ are a set of n_j random orthonormal vectors that are also orthonormal to the gain and loss jumps of the integrable Liouvillian, leading to a

Liouvillian with chaotic statistics

$$\begin{aligned}\mathcal{L}_{\text{chaotic}} =& - i\sum_i h_i K_i^z + \Gamma\sum_{a=1}^{n_j}\sum_i (w_i^a)^2\left[(K_i^z)^2 - (K_i)^2\right] \\ &- \Gamma\sum_{a=1}^{n_j}\sum_{i\neq j} w_i^a w_j^a \frac{1}{2}\left(K_i^+ K_j^- + K_i^- K_j^+\right),\end{aligned} \tag{1.110}$$

Our results show that, in general, a very high or low number of jumps n_j leads to intermediate behaviour in the spectral statistics, while n_j shows the most chaotic statistics.

With the integrable and chaotic limits of the Liouvillian in hand, we can now define the transition Liouvillian using two interpolation parameters $(\alpha,\,\beta)$

$$\mathcal{L}(\alpha,\beta) = (1-\beta)\mathcal{L}_{\text{RG}}(\alpha) + \beta\,\mathcal{L}_{\text{chaotic}}, \tag{1.111}$$

where $\alpha \in [0,1]$ interpolates between the different integrable RG models and $\beta \in [0,1]$ interpolates between the integrable $\beta = 0$ and chaotic $\beta = 1$ limits.

1.6.2 Spectral statistics of the Liouvillian transition

As we have seen, the Liouvillian space is divided into the symmetry sectors determined by its $L+1$ weak symmetries. To study the spectral statistics in the integrable and chaotic regimes we have chosen to focus on the subspace with $k_z = 1$, $k_i = 1$, which is the one with maximal number of eigenvalues. In the particular case of the total angular momentum symmetry, the subspace with $k_z = 0$ has the additional symmetry F and is divided into two smaller diagonal subspaces. Therefore, the subspaces with $k_z = \pm 1$, have a bigger number of eigenvalues than $k_z = 0$. Aside from selecting these subspaces, we have focused on studying spin 1/2 chains.

We show in Figure 1.5(a-c) the spectrum of the constant pairing Liouvillian limit $(\alpha,\beta) = (0,0)$ (a), the rational separable limit $(1,0)$ (b) and the chaotic limit $(0,1)$ (c) for a chain of $L = 6$ spins with $\Gamma = \Gamma_0 = 1/L = 1/6$ and, in the case of the chaotic Liouvillian, $n_j = 3$ random jumps. The single particle levels η_i are chosen as $\eta_i = 1/2 + i/L + \omega_i$, with ω_i drawn from the uniform distribution $\omega_i \in [-1/L,\, 1/L]$. This distribution of the single particle levels has mean value around 1 and, thus, its relative strength can be kept comparable to the dissipation strength for any given size. The two

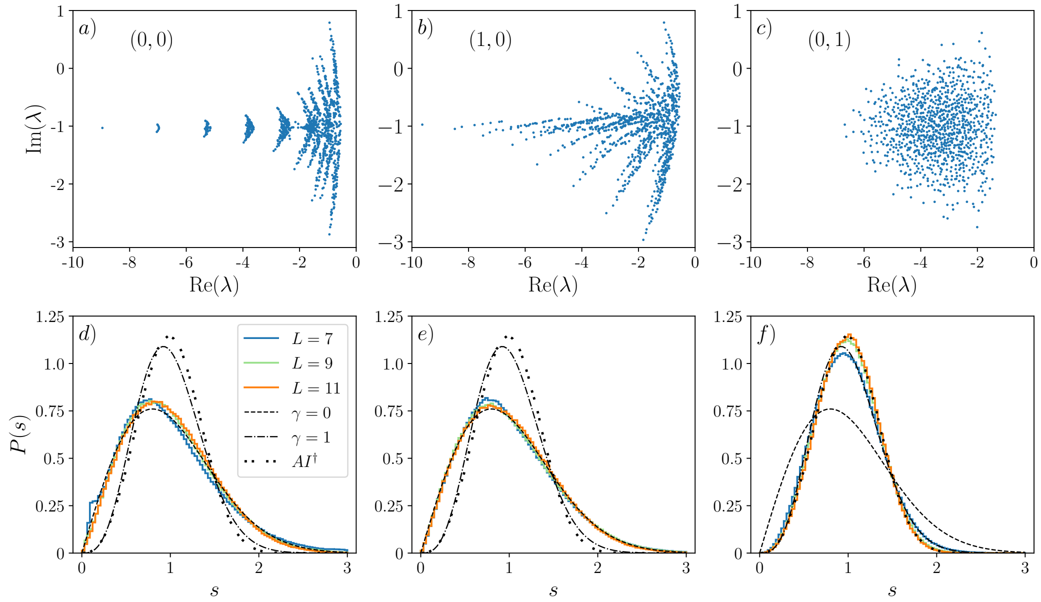

Figure 1.5: (a-c) Eigenvalue spectrum of the transition Liouvillian (1.111) in the constant pairing (a), rational separable (b) and chaotic (c) limit for a system size $L = 6$. (d-f) Level spacing distribution of a sample of several Liouvillians with the same parametrizations as (a-c) but different sizes $L = 7, 9, 11$. The dashed and dot-dashed lines represent the fitting distribution (1.113) for $\gamma = 0$ and $\gamma = 1$, respectively. The dotted line illustrates the level spacing distribution of the $AI^\dagger$ class of non hermitian matrices.

spectra of the integrable limits present level clustering, as we will see below, while the chaotic spectrum presents cubic level repulsion.

We characterize the integrable to chaos transition using the nearest neighbour distribution of the Liouvillian eigenvalues. To do it, we must previously apply an unfolding method to the eigenvalues in order to rescale the local density to an uniform value. This unfolding maps the first neighbour distances to adimensional values that can be compared to Random Matrix Theory results [75]. The method we use works by rescaling each distance by its local density, computed as the inverse area of a circle with a fixed number n of levels inside it

$$S_i = \sqrt{\frac{n}{\pi d_{i,n}^2}}\, d_{i,1}, \tag{1.112}$$

with $d_{i,m}$ the distance of the i-th level to its m-th nearest neighbour. After all levels have been rescaled, the vector **S** is rescaled by its mean, which results in the unfolded spacings s_i. The number of neighbours n must be high enough so that it avoids local fluctuations, while low enough so that it can capture the local spectral properties of the spectrum. We have found $n = 20$ as a good compromise that satisfies both requirements and the distribution results are stable around that number.

The nearest neighbour level statistics of integrable Liouvillians follows the Poisson distribution in the plane (also called 2D Poisson distribution) $P(s) = \frac{\pi}{2}\, s\, e^{-\frac{\pi}{4}s^2}$. On the contrary, the chaotic Liouvillian limit (1.110) is symmetric and non hermitian and, thus, its level statistics belong to that of the $AI^\dagger$ universality class of non hermitian matrices [18] that has been shown by Reference [17] to present $P(s) \sim s^3 \log s$ level repulsion. In a similar way as the Brody distribution [84] maps the transition from integrable to chaotic dynamics in closed hermitian systems, we fit the level spacing distribution to one given by the parameter γ

$$P(s;\, \gamma) = A(\gamma)\, s^{2\gamma+1}\, e^{-B(\gamma)s^2}, \quad \gamma \in [0,1]\,, \tag{1.113}$$

with $A(\gamma)$ and $B(\gamma)$ chosen to satisfy

$$\int_0^\infty P(s)ds = \int_0^\infty s\, P(s)ds = 1 \tag{1.114}$$

For $\gamma = 0$ this distribution reproduces the 2D Poisson and for $\gamma = 1$, while the distribution is not exactly the same as that of the $AI^\dagger$ for large matrices, we will see below that both distributions are sufficiently close that $\gamma = 1$ can be considered a good indicator of a chaotic Liouvillian.

We show the level spacing distribution of the two integrable and chaotic limits of the transition Liouvillian (1.111) in Figures 1.5(d-f). The Liouvillians have different sizes $L = 7, 9, 11$ and their respective Hilbert space dimensions are $d_{\mathrm{H}} = 357, 2907, 24068$, all of them with a dissipation strength of $\Gamma = \Gamma_0 = 1/L$. To compute a good approximation to the exact level statistics, we calculate for each system size L a sample of several Liouvillians so that there are more than 700.000 eigenvalues to compute the level spacing distribution. These distributions are compared to the fitting distribution $P(s;\, \gamma)$ with $\gamma = 0$ (dashed line), $\gamma = 1$ (dash dotted line) and to the distribution of the $AI^\dagger$ universality class (dotted line). As we can see in the Figure, the distributions $AI^\dagger$ and $\gamma = 1$ are very similar and, at the same, time, different from $\gamma = 0$, so we consider $P(s;\, 1)$ a good characterization

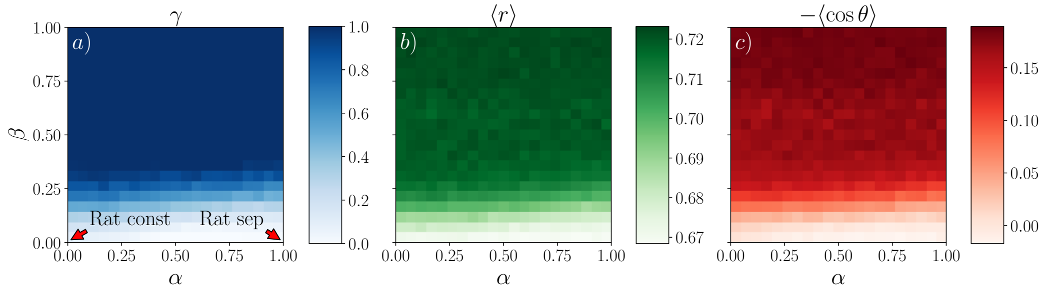

Figure 1.6: Characterization of the integrable to chaotic transition in Liouvillians with the γ fitting parameters (a) and the averages $\langle r\rangle$ (b), $-\langle\cos\theta\rangle$ (c) of the complex spacing ratios.

of the chaotic Liouvillian limit. We find that the integrable Liouvillians of Figures 1.2(d,e) have distributions very close to the 2D Poisson, while the chaotic limit of (c) is similar to the distribution of the $AI^\dagger$ universality class (dotted line). We also find a convergence towards a better fit of the Poisson and $AI^\dagger$ distributions for systems with growing size L.

The fitted interpolation parameter γ is shown in Figure 1.6(a) for intermediate values of (α,β) (1.111). Each point in the Figure results from fitting the level spacing distribution of a sample of 20 Liouvillians with size $L=10$ and $\Gamma=\Gamma_0=1/10$, which have 8350 eigenvalues each. For Liouvillians with $\beta>0$, the number of random jumps is half of the system's size $n_j=5$. The Figure shows that the level spacing distribution of Liouvillians in the integrability line $\beta=0$ are close to the 2D Poisson $\gamma=0$, while the distribution of pure chaotic Liouvillians, $\beta=1$, follow the statistics of the $AI^\dagger$ universality class $\gamma\approx 1$. The transition between both regimes is smooth and integrability is lost at low values of β.

Aside from studying the transition using the level spacings of the eigenvalue spectrum, we have also measured the average absolute and phase values of the complex spacing ratios [83]

$$z_k = r_k e^{i\theta_k} := \frac{\lambda_k^{\mathrm{NN}}-\lambda_k}{\lambda_k^{\mathrm{NNN}}-\lambda_k}, \tag{1.115}$$

where r_k and θ_k are the absolute and phase values of the ratios, λ_k is the k-th Liouvillian eigenvalue and λ_k^{NN}, λ_k^{NNN} its nearest and next to nearest neighbours, respectively. Contrary to the level spacings $d_{i,m}$, the complex ratios

z_k are adimensional quantities where an unfolding procedure is not needed. These ratios represent a generalization for complex spectra of the equivalent quantity introduced in Reference [85], which is extensively used as no unfolding is needed. They have only been computed for a few examples [16, 83, 86] in open quantum systems and it is important to compare their results to those of more standard methods, such as the level spacing distribution.

Figures 1.6(b,c) show the average absolute and phase values of the complex spacing ratios. These have been shown in Reference [83] to be good indicators of the spectral statistics regime and also show a dependence on the symmetries of the model. The authors find in the case of integrable Liouvillians the average values $(\langle r \rangle, -\langle \cos\theta \rangle) = (2/3, 0)$ in the large size limit $L \to \infty$ and $\approx (0.72, 0.2)$ for the $AI^{\dagger}$ universality class of non hermitian matrices. Our results quantitatively coincide with the previous values, although the average phase $-\langle \cos\theta \rangle$ has lower results than those indicated, which is due to the finite size effect present in systems of the size studied in this work, although for $\langle r \rangle$ these finite size effects are no longer appreciable. Aside from this, the average values of the complex spacing ratios show an excellent agreement with the measurements of the $P(s;\, \gamma)$ distribution.

1.6.3 Conclusions

We have introduced a novel family of integrable Liouvillians based on RG models that interpolates between the rational and hyperbolic integrable models. This family has a physical interpretation in terms of a system with complex gain, loss and dephasing interactions with its surrounding environment and represents a new direction in the study of the dynamical properties of open quantum systems, of which only a few specific integrable models are yet known.

Using the integrable Liouvillian we have defined an interpolation model that can transition from the integrable limit to a chaotic one that arises from the system having several random gain and loss jump operators. We have studied the transition from integrability to chaos using the spectral statistics of the Liouvillian's eigenvalues and the complex spacing ratios. This last method has an advantage over the spacing distribution in that it does not require a previous unfolding of the eigenvalues, which can, sometimes, modify the level spacing distribution.

In the integrable line we have found a good agreement between the spacing distribution of the eigenvalues and the 2D Poisson distribution, while in the chaotic regime we found a good agreement with the spacing distribution of the $AI^{\dagger}$ universal class of non hermitian matrices. Using this, we were able to derive a very simple interpolation formula that can classify between the integrable and chaotic regimes. While it is not able to distinguish between the different symmetry classes of Liouvillians, it is a very simple indicator of integrability. On the other hand, the characterization of the chaos with the complex spacing ratios shows an excellent agreement with that of the interpolation function, while it is also able to classify the $AI^{\dagger}$ symmetry class of the chaotic Liouvillian. This indicates the major advantage of the complex spacing ratios as a tool for the identification of integrability and chaos in open quantum systems, as its implementation is simpler than the level spacing distribution.

1.7 Conclusions

Richardson-Gaudin models represent a rich class of integrable systems with many applications in superconductivity, topological systems and spin models. While these were initially applied to closed quantum systems, we have shown its versatility in the modelling of open quantum systems under the LGKS formalism. Our main lines of work have been the derivation of two novel families of Liouvillians that belong to integrable Richardson-Gaudin models.

The first line of work is the description of a Liouvillian applicable to the collective behaviour of atom systems with a general number of levels. We have found that this Liouvillian generalizes a previous existing model in the literature and we analysed the Liouvillian spectral properties in a more complex model with 3-level atoms. By solving the RG equations as an electrostatic problem we were able to study the exact solutions of the system. Furthermore, we have studied its complete spectrum and proposed a coherent state ansatz capable of reproducing the steady state and slowest decaying modes in the thermodynamic limit.

The second line of work focused on a new family of spin-1/2 integrable Liouvillians that can be written as long ranged rational or hyperbolic interacting models. By defining a chaotic Liouvillian with random jumps we were able to derive a Liouvillian that smoothly transitions from the integrable to the chaotic regime with a single parameter. We studied the transition with the level spacing distribution and the average values of the complex spacing ratios and our results show an excellent agreement with the results of

Random Matrix Theory for non hermitian matrices.

Our work opens up a new line of investigation on the properties of open quantum many-body systems, as it introduces two new families of integrable Liouvillians with a direct physical interpretation in terms of the LGKS approximation. New directions could focus on the several possibilities that Richardson-Gaudin models lay out for novel Liouvillians, such as central spin models or open versions of the interacting Kitaev wire. On the other hand, our work represents a new impulse in the employment of the complex spacing ratios as a simple tool to characterize quantum chaos in open quantum systems.

Chapter 2

The vRDM method

2.1 Introduction

As we have seen in the previous Chapter, some particular models have an exact solution for its eigenstates with algebraic complexity. However, these are, in general, restricted to a rich but narrow class of Hamiltonians and, in the majority of cases, slightly deforming the Hamiltonian outside of the region of integrability quickly renders the exact solution useless. In these cases, the exact solution, computed with exact diagonalization of the Hamiltonian matrix, is only available for systems with a maximum Hilbert space dimension of around tens of thousands of states and studying larger systems immediately faces the so called exponential wall problem. Namely, the dimension of the Hilbert space grows exponentially with the number of degrees of freedom of the system and, therefore, computing the wave function of a large system quickly becomes intractable.

There are several ways to overcome the exponential wall problem. One of these families of numerical methods starts with a simple mean field approximation to the wave function and then tries to improve it by adding small perturbations. To this family belong Coupled Cluster Methods [87, 88], Many-Body Perturbation Theory [89] and Random Phase Approximation [90]. These methods, however, start to break up when the system correlation becomes large. Another family are variational theories, in which one proposes a complex wave function that depends on a series of parameters and then looks for the specific set of parameters that minimize the energy of the system. Examples of such methods are the Density Matrix Renormalization Group [91] and the related Tensor Network methods [92], and Variational quantum Monte Carlo [93]. One last family of methods is related to the embedding of some small fragment of the system treated with high precision into a system environment treated with low precision, such as Dynamical Mean Field theory [94, 95] or Density Matrix Embedding Theory [96]. All these families work with a clever form of the *wave function* that tries to capture as much information about the system as possible and many of them can produce very accurate results for some particular medium to large quantum many-body systems. Nevertheless, being able to compute any result within the desired precision in a reasonable amount of time is still a very hard ongoing problem.

A very different approach to study quantum many-body systems that does not rely on computing the wave function is the variational reduced density matrix (vRDM) method [97–100]. This method focusses on the p-particle reduced density matrix (p-RDM) [101, 102] of the quantum state instead of on the full wave function. Its advantage is that the p-RDM is a very compact object with a polynomial number of elements that contains all relevant information about most relevant physical observables of interest. The method works by choosing a set of p-RDMs, generally the 1-RDM, 2-RDM, ..., and so on, and expressing the energy of the system in terms of the 1- and 2-RDMs. It then tries to minimize the system's energy while also enforcing constraints on the p-RDMs, called the N-representability conditions [103–105], so that the p-RDMs belong to a physical quantum state (either pure or not). Examples of some simple N-representability conditions are: enforcing the Pauli exclusion principle or enforcing the system to have a non negative particle number at some position. While imposing all N-representability conditions to all p-RDMs ensures the complete physicality of the solution, this is in general a very hard computational problem and one usually imposes a truncated set of the most relevant conditions. However, this truncation automatically lets some degree of non physicality in the p-RDMs and the computed ground state energy will always lie below the exact one. As such, the vRDM method outputs a lower bound to the ground state energy.

For some systems with exact or approximate pair symmetry 1.2.1, e.g. systems with spin degeneracy, we can greatly improve the vRDM method efficiency by working in the Doubly Occupied Configuration Interaction (DOCI) space, where all particles are coupled in degenerate pairs. In these systems it has been shown that the greatest contribution to the static correlation of the ground state usually comes from the DOCI space [106–109]. Other spaces with a low number of unpaired particles can also have an important, although not the greatest, contribution to the static correlation. It is thus a great advantage that the p-RDMs become highly sparse in the DOCI space, which can then be used to lower the computational cost of the vRDM method and increase the number of enforced N-representability conditions. This use of the symmetries of the DOCI space is referred to as the vRDM-DOCI method.

This Chapter is structured as follows. In Section 2.2 the vRDM method will be introduced. The N-representability conditions, central to the vRDM method, are analysed in Section 2.3 and their particular form in the seniority zero subspace, or DOCI space, is described in Section 2.4. There, the different conditions are classified according to the particle number of the operators that make them, generating the so called p-particle N-representability conditions, which we abbreviate to p-POS conditions. In the following sections the vRDM method is applied to different integrable pairing and molecular models using different p-POS conditions in the DOCI space. Section 2.5, based on our article *Benchmarking the Variational Reduced Density Matrix Theory in the Doubly Occupied Configuration Interaction Space with Integrable Pairing Models* [110], studies several integrable pairing models using the 2-POS conditions, which are able to return the exact ground state energies for several, although not all, configurations of the integrable Hamiltonians. In Section 2.6, based on our article *Variational reduced density matrix method in the doubly occupied configuration interaction space using three-particle N-representability conditions* [111], the 3-POS conditions are applied for the first time to a set of small molecular Hamiltonians and integrable pairing models with repulsive interactions. The results of this section show a clear improvement over the 2-POS conditions for all models. Moreover, it demonstrates that the integrability of the model does not guarantee that vRDM will find the exact ground state energy. Section 2.7, based on our article *Variational reduced density matrix method in the doubly-occupied configuration interaction space using four-particle N-representability conditions: Application to the XXZ model of quantum magnetism* [112], applies a new set of conditions, the 4-POS ones, to the integrable 1D Heisenberg XXZ chain and shows a new improvement of the ground state energy results over using only the 2- and 3-POS conditions. The vRDM computed p-RDM is also compared with the exact one, demonstrating that the precision with which the p-RDM is computed is comparable to the precision achieved in the ground state energy. To further test the vRDM method in integrable models, Section 2.8 studies the Inozemtsev model, which is a continuous integrable parametrization between the Haldane-Shastry model and the Heisenberg chain. While all of these sections show results computed with the 2-, 3- and 4-POS conditions, they become very computationally expensive as the number of particles of the conditions is increased. This is analysed using the Heisenberg XXZ chain in Section 2.9. To accelerate the computations, Section 2.10 shows how the different Hamiltonian symmetries can be incorporated in the vRDM method to reduce the number of independent matrix elements it has to compute and Section 2.11, based on our article *Variational determination of the two-particle reduced density matrix within the doubly occupied configuration interaction space: exploiting translational and reflection invariance* [113], studies the 1D and 2D Heisenberg XXZ chains applying these symmetries. The results show the great increase in computational power allowed by making use of the symmetries, enabling us to study bigger lattice systems. Finally, conclusions are drawn in Section

2.12.

2.2 The variational Reduced Density Matrix method.

We start with the most general fermionic two-body Hamiltonian in the second quantization formalism for a chain of L sites

$$H = \sum_{\alpha\beta=1}^{L} T_{\alpha\beta}\, a_\alpha^\dagger a_\beta + \sum_{\alpha\beta\gamma\delta=1}^{L} V_{\alpha\beta\gamma\delta}\, a_\alpha^\dagger a_\beta^\dagger a_\delta a_\gamma \tag{2.1}$$

with $a_\alpha^\dagger$, a_α the fermionic creation and annihilation operators at lattice site α, the matrix T describes the hoppings between two sites of the system and V the two-body interactions. To study the physical properties of this system, e.g. its ground state, the standard approach is to first compute the wave function of that state

$$H|\Psi_0\rangle = E_0|\Psi_0\rangle \tag{2.2}$$

Once this is done, a possible approach to extract information from it is to compute its p-RDM, which is defined as the expectation values of all p-particle operators

$${}^p\Gamma_{\vec{\alpha},\vec{\beta}} = \langle\Psi_0|a_{\alpha_1}^\dagger a_{\alpha_2}^\dagger \dots a_{\alpha_p}^\dagger a_{\beta_p} a_{\beta_{p-1}} \dots a_{\beta_1}|\Psi_0\rangle. \tag{2.3}$$

However, in many cases one is only interested in computing the one-particle reduced density matrix (1-RDM)

$${}^1\Gamma_{\alpha,\beta} = \langle\Psi_0|a_\alpha^\dagger a_\beta|\Psi_0\rangle \tag{2.4}$$

and the two-particle reduced density matrix (2-RDM)

$${}^2\Gamma_{\alpha\beta,\delta\gamma} = \langle\Psi_0|a_\alpha^\dagger a_\beta^\dagger a_\gamma a_\delta|\Psi_0\rangle. \tag{2.5}$$

from which the majority of observables of interest can be computed.

The variational reduced density matrix (vRDM) method represents a different approach to the quantum many-body problem by computing first the p-RDM without computing the wave function. It treats all p-RDM elements as variational parameters and aims to minimize the energy of the system while also imposing constraints that ensure the physicality of the density matrix, i.e. that it can be decomposed into a positive linear combination of physical wave functions like Equation (1.37). These constraints are the N-representability conditions:

- Hermiticity of the p-RDMs
$$^{p}\Gamma_{\vec{\alpha},\vec{\beta}} = ({}^{p}\Gamma_{\vec{\beta},\vec{\alpha}})^{\dagger}. \tag{2.6}$$
- Symmetry (antisymmetry) with respect to particle interchange for bosonic (fermionic) systems. As an example, for the 2-RDM of a fermionic system
$$^{2}\Gamma_{\alpha\beta,\delta\gamma} = -{}^{2}\Gamma_{\beta\alpha,\delta\gamma} = {}^{2}\Gamma_{\beta\alpha,\gamma\delta} = -{}^{2}\Gamma_{\alpha\beta,\gamma\delta}. \tag{2.7}$$
- The trace of the full density matrix is equal to one, so the trace of the different p-RDMs must be a finite number.
- Semipositivity of the p-RDM against every N-particle operator $\hat{O}$
$$\langle \hat{O} \rangle = \mathrm{tr}({}^{p}\Gamma \cdot \hat{O}) \geq E_0^O, \quad \forall \hat{O}, \tag{2.8}$$
  with E_0^O the ground state energy of the operator $\hat{O}$. We refer to these conditions as the *semipositivity conditions*. As an example, for the 2-RDM and two-body operators of the form of Equation (2.1), these conditions enforce
$$\langle H \rangle = \sum_{\alpha\beta=1}^{L} T_{\alpha\beta}\, {}^{1}\Gamma_{\alpha\beta} + \sum_{\alpha\beta\gamma\delta=1}^{L} V_{\alpha\beta\gamma\delta}\, {}^{2}\Gamma_{\alpha\beta\gamma\delta} \geq E_0^H, \quad \forall H \tag{2.9}$$
  Note that in this condition it is not imposed that the expectation value of H is smaller than its largest eigenvalue, as this condition is equivalent to imposing the semipositivity of $-H$.

The first three conditions: hermiticity, antisymmetry and finite trace are easy to impose on the density matrix. The semipositivity conditions, however, are not and usually one can only impose semipositivity with respect to a finite subset of q-particle operators, which can let some degree of non physicality in the p-RDM. For example, the Pauli exclusion principle for fermions is usually imposed as a semipositivity condition on the elements of the 1-RDM
$$\mathrm{tr}({}^{1}\Gamma \cdot a_i^{\dagger} a_i) = \langle a_i^{\dagger} a_i \rangle \leq 1.$$

Not imposing this condition to the 1-RDM elements means that, when the vRDM algorithm tries to minimize the energy of an arbitrary Hamiltonian, it will probably output a lower energy than the exact one and a non physical 1-RDM that violates the Pauli exclusion principle. We will later see a full example of this non physicality. Of course, as more semipositivity conditions are imposed on the p-RDMs, the vRDM results will improve. In principle, by imposing all conditions one is guaranteed to get the exact p-RDMs of the ground state and its energy.

2.3 The semipositivity conditions

We begin this section by defining the semipositivity of a general matrix. A $n \times n$ hermitian matrix A is said to be positive semidefinite, $A \succeq 0$, if, for every vector $\mathbf{x} \in \mathbb{C}^n$,

$$\mathbf{x}^\dagger A\,\mathbf{x} \geq 0. \tag{2.10}$$

We use the symbol $\succeq 0$ to denote a positive semidefinite matrix. Its properties are:

- Its eigenvalues are non negative

$$\lambda_i(A) \geq 0, \quad \forall i. \tag{2.11}$$

- Its diagonal elements are non negative

$$A_{ii} \geq 0, \quad \forall i. \tag{2.12}$$

- It can be decomposed as the product of two matrices

$$A = B^\dagger B. \tag{2.13}$$

  From this property the semipositivity condition can be proven

$$\mathbf{x}^\dagger A\,\mathbf{x} = \mathbf{x}^\dagger B^\dagger B\mathbf{x} = |B\mathbf{x}\,|^2 \geq 0. \tag{2.14}$$

Interestingly, the semipositivity conditions (2.8) of the p-RDM can be reformulated as a group of matrices taken from the p-RDM being positive semidefinite. This is seen by lifting every N-particle operator by its ground state energy

$$\langle \hat{O} \rangle = \mathrm{tr}\left[\left(\hat{O} - \mathbb{I}\,E_0^O\right) \cdot {}^2\Gamma\right] \geq 0, \quad \forall \hat{O}. \tag{2.15}$$

Thus, imposing semipositivity with respect to an operator $\hat{O}$, whose ground state energy is zero, is equivalent to imposing semipositivity with respect to every operator $\hat{O} + \alpha\mathbb{I}$, with α any real number. To build the entire set of positive semidefinite operators with zero ground state energy we use the decomposition property of positive semidefinite matrices and define a positive semidefinite operator as

$$\hat{O} = B^{\dagger}B \tag{2.16}$$

with B a generic operator

$$B = \sum_i \alpha_i O_i \tag{2.17}$$

and O_i a set of string operators. Thus, the semipositivity condition (2.15) becomes

$$\langle \hat{O} \rangle = \mathrm{tr}\left(B^{\dagger}B \cdot {}^{2}\Gamma\right) = \sum_{ij} \alpha_i \; \mathrm{tr}\left(O_i^{\dagger}O_j \cdot {}^{2}\Gamma\right) \alpha_j \geq 0. \tag{2.18}$$

This condition is very similar to the condition of a matrix being positive semidefinite (2.10), where the matrix in this case is

$$M_{ij} = \mathrm{tr}\left(O_i^{\dagger}O_j \cdot {}^{2}\Gamma\right) \tag{2.19}$$

and

$$\sum_{ij} \alpha_i \, M_{ij} \, \alpha_j \geq 0 \quad \text{implies} \quad M \succeq 0. \tag{2.20}$$

Thus, by defining all operators B of the form of (2.17) one can impose the complete set of semipositivity conditions on the p-RDM. It also becomes clear that the parameters α_i can be chosen at will, because, if M is semidefinite positive, then, for every set of α_i the condition (2.20) holds. Therefore, without loss of generality we will set $\alpha_i = \pm 1$.

Before dwelling into the details of the semipositivity conditions, we note that the set of all possible p-particle B operators is a very large set and, thus, finding all semipositivity conditions is a challenging task. To classify them one usually labels them depending on the number of particles of the O_i string operators and calls them, e.g. the p-particle N-representability conditions if O_i are p-particle operators. This defines a hierarchy of conditions given by their particle number. In general, one starts imposing the 1-particle conditions and then goes up the ladder with the 2- and 3-particle ones.

2.3.1 The 1-particle N-representability conditions

Let us focus on a chain of L spinless fermions with particle number symmetry. The most general 1-particle N-representability conditions are given by the operator

$$B = \sum_{i=1}^{L} a_i^\dagger + a_i. \tag{2.21}$$

with $a_i^\dagger$, a_i the fermion creation and annihilation operators at site i. The element operators inside $B^\dagger B$ that break the particle number symmetry must be zero, which separates the 1-particle B operators into two terms that will result only in number conserving observables: one operator

$$B_P = \sum_{i=1}^{L} a_i, \tag{2.22}$$

which results in the following positive semidefinite $L \times L$ matrix

$$P_{ij} = \langle (B_P^\dagger B_P)_{ij} \rangle = \langle a_i^\dagger a_j \rangle = \ {}^1\Gamma_{ij}, \quad P \succeq 0, \tag{2.23}$$

with ${}^1\Gamma$ the 1-RDM and a second operator

$$B_Q = \sum_{i=1}^{L} a_i^\dagger, \tag{2.24}$$

which results in another $L \times L$ matrix of the form

$$Q_{ij} = \langle (B_Q^\dagger B_Q)_{ij} \rangle = \langle a_i a_j^\dagger \rangle = \delta_{ij} - \langle a_j^\dagger a_i \rangle = \delta_{ij} - \ {}^1\Gamma_{ij}, \quad Q \succeq 0. \tag{2.25}$$

2.3.2 A very simple example of the vRDM method

We have explained above the complete toolset of the vRDM method. Let us see how does it work in a very simple example: a chain of spinful fermions with $L = 3$ sites. We will use the 1-RDM as the variational parameters and impose the 1-particle N-representability conditions described in the section above. The Hamiltonian has only local and first-neighbour hoppings terms

$$H = \sum_{i=1}^{3} \omega_i \, n_i + t \sum_{i=1}^{2} \left(a_i^\dagger a_{i+1} + \text{h.c.} \right), \tag{2.26}$$

with $n_i = a_i^\dagger a_i$, ω_i and t are real numbers and where h.c. stands for hermitian conjugate. For this example the elements of the 1-RDM are used as the variational parameters

$$^1\Gamma = \begin{pmatrix} \langle a_1^\dagger a_1 \rangle & \langle a_1^\dagger a_2 \rangle & \langle a_1^\dagger a_3 \rangle \\ \langle a_2^\dagger a_1 \rangle & \langle a_2^\dagger a_2 \rangle & \langle a_2^\dagger a_3 \rangle \\ \langle a_3^\dagger a_1 \rangle & \langle a_3^\dagger a_2 \rangle & \langle a_3^\dagger a_3 \rangle \end{pmatrix} \to \begin{pmatrix} \rho_{11} & \rho_{12} & \rho_{13} \\ \rho_{21} & \rho_{22} & \rho_{23} \\ \rho_{31} & \rho_{32} & \rho_{33} \end{pmatrix} . \tag{2.27}$$

Note the change in notation $^1\Gamma_{ij} \to \rho_{ij}$. In the next section we will redefine all p-RDM terms into simpler notations.

We start by imposing the first three N-representability conditions described in Section 2.2, namely: antisymmetry of the wave function, finite trace and hermiticity of the p-RDM. For the 1-RDM given above, the hermiticity condition requires $\rho_{ij} = \rho_{ji}$ and the finite trace condition can be related to the $U(1)$ particle conservation symmetry of the Hamiltonian

$$\sum_{i=1}^{3} \rho_{ii} = M, \tag{2.28}$$

with M the number of particles. The antisymmetry conditions do not play a role in the 1-RDM, although they are important for p-RDMs with $p \geq 2$. With these conditions set, the vRDM method consists of finding the set of parameters

$$\{\rho_{11},\, \rho_{22},\, \rho_{33},\, \rho_{12},\, \rho_{13},\, \rho_{23},\, \}$$

such that they minimize the expectation value of the Hamiltonian

$$E = \mathrm{tr}\,(H\rho) = \sum_{i=1}^{3} \omega_i \, \rho_{ii} + 2t \sum_{i=1}^{2} \rho_{i,i+1}, \tag{2.29}$$

and the following constraints are met

$$\begin{aligned} &\rho_{11} + \rho_{22} + \rho_{33} = M \\ P = &\begin{pmatrix} \rho_{11} & \rho_{12} & \rho_{13} \\ \rho_{12} & \rho_{22} & \rho_{23} \\ \rho_{13} & \rho_{23} & \rho_{33} \end{pmatrix} \succeq 0 \\ Q = &\begin{pmatrix} 1-\rho_{11} & -\rho_{12} & -\rho_{13} \\ -\rho_{12} & 1-\rho_{22} & -\rho_{23} \\ -\rho_{13} & -\rho_{23} & 1-\rho_{33} \end{pmatrix} \succeq 0, \end{aligned} \tag{2.30}$$

The solution of this system of equations will always return a lower bound for the exact ground state energy. Moreover, according to the properties of positive semidefinite matrices, the diagonal values of P, Q must be non negative. Therefore, the most basic assumptions: the Pauli exclusion principle and non negative particle number are met

$$0 \leq \rho_{ii} \leq 1. \tag{2.31}$$

Note that, if the semipositivity of P would not have been imposed, then for any $\omega_i > 0$ the method would return a lower bound for the energy of $E \to -\infty$ at the cost of having a negative occupation number $\rho_{ii} < 0$. Thus, the most basic principle of the vRDM method can be observed here: imposing more N-representability conditions will always return a more accurate result.

2.3.3 The 2-particle N-representability conditions

We can build the 2-particle N-representability conditions with the following number conserving operators

$${}^2B_P = \sum_{i<j=1}^{L} a_i a_j, \quad {}^2B_Q = \sum_{i<j=1}^{L} a_i^\dagger a_j^\dagger, \quad {}^2B_G = \sum_{i<j=1}^{L} a_i^\dagger a_j. \tag{2.32}$$

and the positive semidefinite operators that they give rise to are

$$\begin{aligned} P_{ijkl} &= \langle a_i^\dagger a_j^\dagger a_l a_k \rangle, \quad P \succeq 0 \\ Q_{ijkl} &= \langle a_i a_j a_l^\dagger a_k^\dagger \rangle, \quad Q \succeq 0 \\ G_{ijkl} &= \langle a_i^\dagger a_j a_l^\dagger a_k \rangle, \quad G \succeq 0. \end{aligned} \tag{2.33}$$

These N-representability conditions and the $\mathcal{T}_1$ and $\mathcal{T}_2$ conditions, which will be presented later, have enjoyed great success [97, 99, 100, 114–116] in finding accurate descriptions of the ground state of a wide variety of systems. However, the sizes of these semipositivity matrices are of order $L^2 \times L^2$, which sets a fundamental limit in what sizes the vRDM method can compute. For systems with more than $\sim$ 20 sites, the present computational capacity cannot cope with the huge matrix sizes that these semipositivity conditions require. Therefore, N-representability conditions of more than 2-particles are intractable for systems with medium to large sizes, except in the case where we can reduce the size of the p-RDMs, as we will see later.

2.3.4 The vRDM method as a semidefinite program

Semidefinite programming (SDP) is a field of convex optimization that has attracted a lot of interest due to its connections with combinatorial optimization, automatic control theory and operations research. This method tries to minimize a linear function over a set of parameters while maintaining positive semidefinite constraints on them. It is formally written as a pair of related systems, the primal and the dual SDPs

$$\begin{cases} \text{primal:} & \begin{cases} \text{minimize} & \sum_{i=1}^{m} c_i x_i \\ \text{subject to} & X = \sum_{i=1}^{n} F_i x_i - F_0 \succeq 0 \end{cases} \\ \text{dual:} & \begin{cases} \text{maximize} & F_0 \cdot Y \\ \text{subject to} & F_i \cdot Y = c_i, \quad Y \succeq 0, \end{cases} \end{cases} \tag{2.34}$$

with x_i the set of m variables to minimize, c_i a set of constant parameters, F_0, F_i a set of symmetric constraint matrices related to the semipositivity conditions and X, Y a pair of symmetric positive semidefinite matrices. The notation $A \cdot B$ denotes the inner product $A \cdot B = \sum_{ij} A_{ij} B_{ij}$. Under the weak duality theorem, the primal value $\sum_i c_i x_i$ is always larger than the dual one $F_0 \cdot Y$, so solving both problems at once returns an estimation of the primal value and a lower bound for it (the dual value).

SDP problems are usually solved with interior-point methods. Basically, they start in a region (x, X, Y) where all constraints are satisfied, the so called feasibility region. Then it moves $\vec{x}$ in the direction $-\vec{c}$ and makes minor corrections in the displacement so that the solution remains in the feasibility region. The algorithm then tries to keep moving in the same direction until the gap between the primal and dual values is closed as much as possible. It can be shown [117] that both the objective function of the primal SDP system $\sum_i c_i x_i$ and the constraint X are convex functions. Therefore, it is guaranteed that the feasibility region of the SDP problem is convex and there are no local minima other than the global one.

In a crucial observation, Nakata *et al.* [98] showed that the problem of finding the p-RDM that minimizes the energy with a set of N-representability conditions can be written as a SDP problem. To do so, they pointed out that the expectation value of any operator is a linear function of the p-RDM terms, e.g. as in Equation (2.29). This allowed them to formulate the vRDM method as a dual SDP problem (2.34) where the matrix Y is a block-diagonal matrix containing all semidefinite conditions on the p-RDMs. In the example of the above Section 2.3.2, Y would correspond to

$$Y = \begin{pmatrix} P & 0 \\ 0 & G \end{pmatrix} = \begin{pmatrix} {}^1\Gamma & 0 \\ 0 & \mathbb{I} -^1 \Gamma \end{pmatrix} \tag{2.35}$$

with ${}^1\Gamma$ the 1-RDM. Note that a block-diagonal matrix is positive semidefinite if its block matrices are all positive semidefinite. It suffices now to identify F_0 with the Hamiltonian elements

$$F_0 = \begin{pmatrix} H & 0 \\ 0 & 0 \end{pmatrix} \tag{2.36}$$

and F_i with the different system constraints. In this simple example, the only equality constraint is the conservation of particle number $\sum_i \rho_{ii} = N$. Therefore, we would choose

$$F_1 = \begin{pmatrix} \mathbb{I} & 0 \\ 0 & 0 \end{pmatrix}, \quad c_1 = N. \tag{2.37}$$

With this choice of matrices solving the p-RDMs that minimizes the energy is formulated as a SDP problem.

2.3.5 Software

Due to the broad interest on SDP problems there are several numerical solvers available for public use based on primal-dual interior-point methods, such as SeDuMi, MOSEK, SDPT3 and the Semidefinite Programming Algorithm (SDPA) [118, 119]. There are two main families of algorithms for solving the SDP problem: primal-dual interior-point methods and interior-point methods. The former are considered to be the most robust, but for many applications the algorithm has a bottleneck in that it has to solve a very large linear system of equations, which limits the size of the problems they are able to solve. On the other hand, interior-point methods have gained a lot of attention, since they tend to be 10-20 faster than their counterpart [120], but they usually suffer from numerical instabilities. Therefore, we have chosen to perform all computations using the more numerically stable primal-dual interior-point SDPA solver [119].

While the method to write the vRDM algorithm into a SDP problem has been described before, we note that the SDPA solver does not allow for the introduction of equality constraints on the p-RDMs. However, we can introduce these constraints by relaxing them into semipositivity conditions. As an example, for the conservation of particle number in the example of Section 2.3.2, we choose a sufficiently small δ so that

$$\Big|\sum_{i=1}^{3}\rho_{ii}-N\Big|\leq\delta. \tag{2.38}$$

In that case, by expanding the absolute value, the condition is written as two semidefinite conditions

$$\begin{aligned}\delta+\sum_{i=1}^{3}\rho_{ii}-N\geq 0\\ \delta-\sum_{i=1}^{3}\rho_{ii}+N\geq 0.\end{aligned} \tag{2.39}$$

In general, we choose $\delta=10^{-7}$ for our computations. This means that, if we were able to impose all semipositivity conditions needed to compute the exact p-RDMs of the system, the maximum level of precision of any p-RDM would be of order $\delta=10^{-7}$.

2.4 N-representability in the DOCI subspace

Many systems in nuclear [121, 122], molecular [106–108] and condensed matter physics [30] present an approximate or exact double degeneracy in the single particle levels in the Hamiltonian, e.g. opposite spin particles $(i\uparrow, i\downarrow)$ or opposite momenta $(+k,-k)$ [See Section 1.2.1]. The Hamiltonians of these systems commute with the seniority operator Ω [107, 123], which counts the number of broken pairs in the state

$$\Omega=\sum_{i=1}^{L}\left(a_i^\dagger a_i-a_{\bar{i}}^\dagger a_{\bar{i}}\right)^2, \tag{2.40}$$

with $(i,\bar{i})$ a generic pair of degenerate levels. This symmetry operator, thus, divides the Hilbert space into sectors with different seniority numbers.

For systems where such symmetry is exact, for example in $SU(2)$ spin chains [23] or in pairing systems [30], one is usually interested in the subspace where all particles are paired, $\Omega=0$. This subspace is usually referred to as the Doubly Occupied Configuration Interaction (DOCI) space. For systems where seniority symmetry is approximate, as is often the case in nuclear and molecular physics, it has been show [106–109] that splitting the Hilbert space into different seniority subspaces and constraining the ground state to lie in the lowest seniority sectors $\Omega = 0, 2, 4$ can, in most cases, restore the most significant part of the correlation energy within an acceptable precision. It would then be an interesting path to constrain the vRDM method to compute the p-RDMs in the subspaces in the lowest seniority sectors and tossing out the others. However, while non zero seniority sectors can be taken into consideration, the size of the p-RDM still grows very fast for $\Omega > 0$ and we have chosen to focus exclusively on the DOCI space, $\Omega = 0$. Keeping only this subspace makes sense, as it has the greatest contribution to the exact ground state in systems with approximate seniority symmetry and it is the most physically relevant space when the symmetry is fully conserved.

The basis states of the DOCI space are

$$|\vec{i}\rangle = \prod_{j=1}^{M} a^\dagger_{i_j} a^\dagger_{\bar{i}_j} |0\rangle = \prod_{j=1}^{M} b^\dagger_{i_j} |0\rangle, \tag{2.41}$$

with M the number of pairs and $b^\dagger_{i_j} = a^\dagger_{i_j} a^\dagger_{\bar{i}_j}$ a pair creation operator in the $SU(2)$ hard-core boson representation (1.22). In the DOCI space any observable that changes the seniority number, i.e. breaks one pair, has zero expectation value. Thus, the p-RDMs in the *complete* Hilbert space basis are highly sparse and one can define more compact p-RDMs in the DOCI space. Moreover, this sparsity will help to reach new p-particle N-representability conditions beyond 2-particle ones. In the following sections we will explore the new set of smaller N-representability conditions introduced by the DOCI method.

Notation: we refer to the number of pairs in the DOCI space with M, which corresponds to $2N$ single fermionic particles.

2.4.1 The DOCI 1-particle N-representability conditions

We start by rewriting the 1-particle B operator for a system with pairwise level degeneracy $(i, \bar{i})$

$$\begin{aligned} {}^1B_P &= \sum_{i=1}^{L} a_i + a_{\bar{i}} \\ {}^1B_Q &= \sum_{i=1}^{L} a_i^\dagger + a_{\bar{i}}^\dagger . \end{aligned} \tag{2.42}$$

The conditions arising from these operators will impose restrictions on the 1-RDM in the DOCI space, whose elements we define as

$$\rho_i := \langle n_i \rangle = \langle a_i^\dagger a_i \rangle = \langle a_{\bar{i}}^\dagger a_{\bar{i}} \rangle . \tag{2.43}$$

There are no off diagonal elements, as they would imply a change in the seniority number, so their expectation value is zero. The ${}^1B_P$, ${}^1B_Q$ operators can then be divided into operators that respect the seniority number

$$\begin{aligned} {}^1B_P &= \sum_{i=1}^{L} a_i, \quad {}^1\bar{B}_P = \sum_{i=1}^{L} a_{\bar{i}} \\ {}^1B_Q &= \sum_{i=1}^{L} a_i^\dagger, \quad {}^1\bar{B}_Q = \sum_{i=1}^{L} a_{\bar{i}}^\dagger . \end{aligned} \tag{2.44}$$

From them, the resulting DOCI 1-particle N-representability conditions expressed in terms of the 1-RDM are

$$\begin{aligned} {}^1P_{ij} &= \delta_{ij}\, \rho_i \geq 0 \\ {}^1Q_{ij} &= \delta_{ij}\, (1 - \rho_i) \geq 0, \end{aligned} \tag{2.45}$$

which can be summed up as

$$0 \leq \langle n_i \rangle \leq 1, \quad \forall i. \tag{2.46}$$

In addition, if the system conserves the particle number, another condition can be imposed onto the DOCI 1-RDM, related to the diagonal of the matrix P

$$\sum_i \rho_i = M. \tag{2.47}$$

2.4.2 The DOCI 2-particle N-representability conditions

In this case the operators used to construct the N-representability conditions are

$$\begin{aligned}
{}^2B_P &= \sum_{i<j} a_i a_j + a_{\bar{i}} a_{\bar{j}} + \sum_{ij} a_i a_{\bar{j}} \\
{}^2B_Q &= \sum_{i<j} a_i^\dagger a_j^\dagger + a_{\bar{i}}^\dagger a_{\bar{j}}^\dagger + \sum_{ij} a_i^\dagger a_{\bar{j}}^\dagger \\
{}^2B_G &= \sum_{ij} a_i^\dagger a_j + a_{\bar{i}}^\dagger a_{\bar{j}} + \sum_{ij} a_i^\dagger a_{\bar{j}} + a_{\bar{i}}^\dagger a_j .
\end{aligned} \tag{2.48}$$

This set of operators will impose conditions on the form of the DOCI 2-RDM, whose elements we define as

$$\begin{aligned}
\Pi_{ij} &:= \langle b_i^\dagger b_j \rangle \\
D_{ij} &:= \langle n_i n_j \rangle .
\end{aligned} \tag{2.49}$$

The 2-RDM elements are related to the 1-RDM by

$$\rho_i \equiv D_{ii} = \Pi_{ii} \tag{2.50}$$

$$\sum_{j=1}^{L} D_{ij} = M \rho_i , \tag{2.51}$$

with M the number of pairs.

The conditions created by the different ${}^2B_x$ operators are:

- Operator: ${}^2B_P$:
  - Blocks: $\sum_{i<j} a_i a_j$ and $\sum_{i<j} a_{\bar{i}} a_{\bar{j}}$. They result in the following condition
$$D_{ij} = \langle n_i n_j \rangle \geq 0, \quad \forall\ i < j. \tag{2.52}$$
  - Block: $\sum_i a_i a_{\bar{i}}$. This is called the $\mathcal{P}$ condition:
$$P_{ij} = \langle a_i^\dagger a_{\bar{i}}^\dagger a_{\bar{j}} a_j \rangle = \langle b_i^\dagger b_j \rangle = \Pi_{ij}, \quad P \succeq 0. \tag{2.53}$$
- Operator: ${}^2B_Q$:

  - Blocks: $\sum_{i<j} a_i^\dagger a_j^\dagger$ and $\sum_{i<j} a_{\bar{i}}^\dagger a_{\bar{j}}^\dagger$:

    $$1 - \rho_i - \rho_j + D_{ij} \geq 0, \quad \forall\; i < j. \tag{2.54}$$

  - Block: $\sum_i a_i^\dagger a_{\bar{i}}^\dagger$. This is called the $\mathcal{Q}$ condition:

    $$Q_{ij} = \langle a_i a_{\bar{i}} a_{\bar{j}}^\dagger a_j^\dagger \rangle = \langle b_i b_j^\dagger \rangle = \Pi_{ij} + \delta_{ij}\left(1 - 2\rho_i\right), \quad Q \succeq 0. \tag{2.55}$$

- Operator: ${}^2B_G$:

  - Blocks: $\sum_{i \neq j} a_i^\dagger a_{\bar{j}}$ and $\sum_{i \neq j} a_{\bar{i}}^\dagger a_j$. The positive semidefinite matrix created by these operators is highly sparse and its elements are

    $$\langle a_i^\dagger a_{\bar{j}} a_{\bar{l}}^\dagger a_k \rangle = \delta_{jl}\delta_{ik}\left(\rho_i - D_{ij}\right) - \delta_{il}\delta_{jk}\Pi_{ij}, \quad \forall\; i \neq j, \tag{2.56}$$

    The order of the elements can be rearranged so that the semipositivity condition is mapped to the semipositivity of a set of $L(L-1)/2$ matrices of size 2×2, the so called $\mathcal{G}$ conditions:

    $$G_{ab} = \begin{pmatrix} \rho_a - D_{ab} & -\Pi_{ab} \\ -\Pi_{ab} & \rho_b - D_{ab} \end{pmatrix} \succeq 0, \quad \forall\; a < b. \tag{2.57}$$

  - Blocks: $\sum_{ij} a_i^\dagger a_i + a_{\bar{i}}^\dagger a_{\bar{i}}$. For $i = j$ this gives the semipositivity of the D matrix

    $$D_{ij} = \langle n_i n_j \rangle, \quad D \succeq 0. \tag{2.58}$$

Other blocks not listed above are either zero in the DOCI space or result in the same conditions.

Note that the diagonal elements of any positive semidefinite matrix are always non negative. Therefore, the semipositivity of the P and Q matrices necessarily means that $P_{ii} = \rho_i \geq 0$ and $Q_{ii} = 1 - \rho_i \geq 0$, which correspond to the DOCI 1-particle conditions.

2.4.3 The DOCI 3-particle N-representability conditions

For these conditions, the necessary B operators are

$$\begin{aligned}
{}^3B_Q &= \sum_{i<j<k} a_i^\dagger a_j^\dagger a_k^\dagger + a_{\bar{i}}^\dagger a_{\bar{j}}^\dagger a_{\bar{k}}^\dagger + \sum_{i<j,k} a_i^\dagger a_j^\dagger a_{\bar{k}}^\dagger + a_k^\dagger a_{\bar{i}}^\dagger a_{\bar{j}}^\dagger \\
{}^3B_D &= \sum_{i<j<k} a_i a_j a_k + a_{\bar{i}} a_{\bar{j}} a_{\bar{k}} + \sum_{ijk} a_i a_j a_{\bar{k}} + a_k a_{\bar{i}} a_{\bar{j}} \\
{}^3B_F &= \sum_{i<j,k} a_i^\dagger a_j^\dagger a_k + a_i^\dagger a_j^\dagger a_{\bar{k}} + a_{\bar{i}}^\dagger a_{\bar{j}}^\dagger a_k + a_{\bar{i}}^\dagger a_{\bar{j}}^\dagger a_{\bar{k}} \\
&\quad + \sum_{ijk} a_i^\dagger a_{\bar{j}}^\dagger a_k + a_i^\dagger a_{\bar{j}}^\dagger a_{\bar{k}} + \sum_i a_i^\dagger + a_{\bar{i}}^\dagger \\
{}^3B_E &= \sum_{i,j<k} a_i^\dagger a_j a_k + a_i^\dagger a_{\bar{j}} a_{\bar{k}} + a_{\bar{i}}^\dagger a_j a_k + a_{\bar{i}}^\dagger a_{\bar{j}} a_{\bar{k}} \\
&\quad + \sum_{ijk} a_i^\dagger a_j a_{\bar{k}} + a_{\bar{i}}^\dagger a_j a_{\bar{k}} + \sum_i a_i + a_{\bar{i}}
\end{aligned} \tag{2.59}$$

Note that there are several single particle terms in these operators, which help to impose constraints on the elements of the 3-RDM that will result in a better lower bound of the ground state energy. Before computing the N-representability conditions, we define the DOCI 3-RDM elements as

$${}^3D_{ijk} = \langle n_i n_j n_k \rangle, \quad \forall\ i \neq j \neq k \tag{2.60}$$

$${}^3\Pi^i_{jk} = \langle b_j^\dagger n_i b_k \rangle, \quad \forall\ i \neq j, k. \tag{2.61}$$

The relations of the 3-RDM elements with the 2-RDM are:

$$\begin{aligned}
D_{ij} \equiv D_{iij} &= \Pi^i_{jj} = \Pi^j_{ii} \\
\sum_{k(\neq ij)} \Pi^k_{ij} &= (M-1)\Pi_{ij}, \quad \forall\ i<j \\
\sum_{k(\neq ij)} D_{ijk} &= (M-2)D_{ij}, \quad \forall\ i<j.
\end{aligned} \tag{2.62}$$

A full account of the DOCI 3-particle conditions is given in Appendix A.1.

2.4.4 The lifting conditions

In principle, all p-particle conditions can be derived from the (p+1)-particle conditions through the lifting conditions. They are made up by adding the diagonal elements of the positive semidefinite matrices of the (p+1) conditions so that they result in a number operator. If the system preserves particle number, this number operator can be extracted out of the representability condition and computed as a C number. This effectively lowers the order of the operator to p-particles. As an example, consider the following addition of 3-particle condition elements

$$\sum_{a=1}^{L} \Pi^a_{ij} = \sum_{a=1}^{L} \langle b_i^\dagger n_a b_j \rangle = (M-1)\langle b_i^\dagger b_j \rangle = (M-1)P_{ij}. \tag{2.63}$$

Because the sum of a set of positive semidefinite matrices, in this case $\Pi^a \succeq 0$ from the 3-particle conditions, is a positive semidefinite matrix, then, $P \succeq 0$, which is a 2-particle condition. Another example of a lifting condition that is a bit more convoluted is the $\mathcal{G}$ condition

$$\sum_{c(\neq ab)} {}^3\mathcal{E}_{abc} = (M-1)\mathcal{G}_{ab}, \tag{2.64}$$

which imposes the semipositivity of the 2-particle $\mathcal{G}$ conditions based solely on the semipositivity of the 3-particle $\mathcal{G}$ conditions.

2.4.5 The DOCI (2, 3) conditions

It is very interesting to note that, due to the fermionic anticommutation relations, several matrices of the 3-particle conditions can be added up that result in conditions without any 3-RDM elements. These new conditions are called the DOCI (2, 3) N-representability conditions or, more often, the $\mathcal{T}_1$ and $\mathcal{T}_2$ conditions. They offer an enormous computational advantage, as they can improve the accuracy of the 2-RDM of a ground state by several orders of magnitude with respect to the 2-particle conditions [110] and they work only with the 2-RDM, which reduces the computational effort of the vRDM method with respect to taking into account the 3-RDM.

The (2, 3) N-representability conditions are:

- The two $\mathcal{T}^1$ conditions. Adding the 3-particle diagonal conditions (A.4) and (A.5) results in

$$1 - \rho_i - \rho_j - \rho_k + D_{ij} + D_{jk} + D_{ki} \geq 0, \quad \forall\, i < j < k. \tag{2.65}$$

Also, adding the 3-$\mathcal{P}$ and 3-$\mathcal{Q}$ conditions (A.6) and (A.7)

$$\left(T^1\right)^a_{ij} = \Pi_{ji} + \delta_{ij}\left(1 - 2\rho_i - \rho_a + 2D_{ia}\right) \succeq 0, \quad \forall\ a, \quad ij \neq a. \tag{2.66}$$

- The two $\mathcal{T}^2$ conditions. Adding the ${}^3\mathcal{E}_{abc}$ and ${}^3\mathcal{F}_{abc}$ conditions (A.9) and (A.10) results in

$$T^2_{abc} = \begin{pmatrix} t(a) & \Pi_{ac} & \Pi_{ab} \\ \Pi_{ac} & t(b) & \Pi_{bc} \\ \Pi_{ab} & \Pi_{bc} & t(c) \end{pmatrix} \succeq 0 \forall\ a < b < c. \tag{2.67}$$

with $t(x) = \rho_x - D_{xy} - D_{xz} + D_{yz},\ x \in \{a, b, c\}$.

The other T^2 matrix is

$$T^2_a = \begin{pmatrix} \delta_{ij}\rho_i + D_{ij} & -\delta_{ij}\Pi_{ia} & D_{ia} & \rho_i - D_{ia} \\ -\delta_{ij}\Pi_{ia} & \delta_{ij}\left(\rho_a - 2D_{ia}\right) + \Pi_{ij} & \Pi_{ia} & -\Pi_{ia} \\ D_{ia} & \Pi_{ia} & \rho_a & 0 \\ \rho_i - D_{ia} & -\Pi_{ia} & 0 & 1 - \rho_a \end{pmatrix} \succeq 0, \quad \forall\ a, ij \neq a. \tag{2.68}$$

2.4.6 The DOCI 4-particle N-representability conditions

The B operator for these conditions is much more complex and we will omit writing it down. It includes all possible 4-particle operators with all possible spin combinations. Before computing the N-representability conditions, we define the elements of the 4-RDM as

$$\begin{aligned} \Pi_{ijkl} &= \langle b_i^\dagger b_j^\dagger b_l b_k \rangle, \quad \forall\ i \neq j \neq k \neq l \\ \Pi_{ij}^{kl} &= \langle b_i^\dagger b_j n_k n_l \rangle, \quad \forall\ i \neq j \neq k \neq l \\ D_{ijkl} &= \langle n_i n_j n_k n_l \rangle, \quad \forall i \neq j \neq k \neq l. \end{aligned} \tag{2.69}$$

The relations of the 4-RDM with the 3-RDM are

$$\begin{aligned} \sum_{j \neq l} \Pi_{kl}^{ij} &= (M-2)\Pi_{kl}^{i} \\ \sum_{i \neq jkl} D_{ijkl} &= (M-3)D_{jkl} \\ \Pi_{ikkj} = \Pi_{ij}^{k}\ &, \quad \Pi_{ijij} = D_{ij} \\ \Pi_{kk}^{ij} = D_{ijk}\ &, \quad D_{ijkk} = D_{ijk}. \end{aligned} \tag{2.70}$$

For the sake of simplicity we report the expression of the DOCI 4-particle conditions to Appendix A.2.

Notation: We will usually denote the DOCI p-particle conditions as p-POS. When we want to distinguish between the 2-POS and (2, 3)-particle conditions, we will also denote them as $\mathcal{PQG}$ and $\mathcal{PQGT}$ conditions, respectively.

2.5 Benchmarking the vRDM in the DOCI space with integrable pairing models

The results from this section are reported in our article: *Benchmarking the Variational Reduced Density Matrix Theory in the Doubly Occupied Configuration Interaction Space with Integrable Pairing Models* [110].

As we have seen in Chapter 1, for integrable pairing models we can compute their exact ground state wave function, its energy and occupation numbers. Therefore, these models serve as an excellent platform to benchmark the vRDM-DOCI method with large systems where exact diagonalization becomes no longer possible. In this section, we will study the ground state of the RGK (1.29) and reduced BCS (1.24) Hamiltonians using the vRDM-DOCI method with the $\mathcal{PQG}$ and $\mathcal{PQGT}$ conditions. As a benchmark we will employ the ground state energy and the canonical gap (1.34) of the models. Our results show that the $\mathcal{PQGT}$ conditions offer a great improvement in the accuracy of the method over the $\mathcal{PQG}$ conditions. Moreover, we find several configurations of integrable Hamiltonians in the attractive interaction regime for which the method becomes exact.

2.5.1 The Richardson-Gaudin-Kitaev Hamiltonian

We start with the Richardson-Gaudin-Kitaev Hamiltonian of a chain of $L = 50$ pairwise degenerate fermionic levels

$$H = \frac{1}{2} \sum_{k \in \mathcal{S}^{\phi}} \eta_k \left(n_k + n_{-k} \right) - g \sum_{kk' \in \mathcal{S}^{\phi}} \sqrt{\eta_k \eta_{k'}}\, c_k^{\dagger} c_{-k}^{\dagger} c_{-k'} c_{k'} \tag{2.71}$$

The chain is half filled, so there are $M = 25$ pairs. The dimension of the Hilbert space for this configuration is of order $\sim 10^{14}$ states and an exact diagonalization approach to the ground state is computationally unfeasible, so the ground state must be computed using the RG equations as explained in Section 1.2. The ground state of the RGK Hamiltonian has two critical points: Moore-Read $g_{\mathrm{MR}} = 1/(L - M + 1) = 1/26$ and Read-Green $g_{\mathrm{RG}} = 1/(L - 2M + 2) = 1/2$. The Read-Green point is at a very large value of the interaction, so we will focus instead on benchmarking the vRDM-DOCI method in the attractive region around the Moore-Read point.

At the Moore-Read point the ground state becomes a PBCS state (1.33). These states have the property that they are annihilated by a set of L^2 two-body operators, commonly referred to as the killers,

$$B_{kk'} = \sqrt{\eta_{k'}} c_k^\dagger c_{k'} - \sqrt{\eta_k} c^\dagger_{-k'} c_{-k}, \quad B_{kk'}|\psi_{\mathrm{MR}}\rangle = 0, \quad \forall\, kk'. \tag{2.72}$$

Interestingly, at the Moore-Read point the RGK Hamiltonian can be written as a positive linear combination of projectors onto the killers, which individually are positive semidefinite operators,

$$\begin{aligned} H(g_{\mathrm{MR}}) &= \frac{1}{2L + 2 - 2M} \sum_{kk'} B^\dagger_{kk'} B_{kk'} = \\ &= \frac{1}{2} \sum_k \eta_k \left(n_k + n_{-k}\right) - g_{\mathrm{MR}} \sum_{kk'} \sqrt{\eta_k \eta_{k'}}\, c_k^\dagger c^\dagger_{-k\bar{k}} c_{-k\bar{k}'} c_{k'}. \end{aligned} \tag{2.73}$$

Thus, the ground state energy at Moore-Read is $H|\psi_{\mathrm{MR}}\rangle = 0$. Because the Hamiltonian is written as a sum of two-body semidefinite positive operators, imposing the 2-POS conditions guarantees that the vRDM-DOCI method will find the exact ground state energy at the MR point.

We show in Figure 2.1(a) the absolute difference of the exact ground state energy with respect to the energy of the vRDM-DOCI method with both the $\mathcal{PQG}$ and $\mathcal{PQGT}$ conditions and a variational PBCS state (1.33) of the form

$$|\psi(\vec{\alpha})\rangle = \left(\sum_k \alpha_k c_k^\dagger c_{-k}^\dagger\right)|0\rangle, \tag{2.74}$$

with $\vec{\alpha}$ a set of variational parameters. Because the vRDM-DOCI method provides a lower energy bound, while the variational PBCS ansatz returns an upper bound, we show the absolute energy differences with respect to the exact ground state energy. As we have seen above, the $\mathcal{PQG}$ N-representability conditions and the PBCS ansatz correctly capture the ground state energy at the Moore-Read point, as the exact ground state becomes a PBCS state at that point. However, outside that region the $\mathcal{PQG}$ conditions achieve an

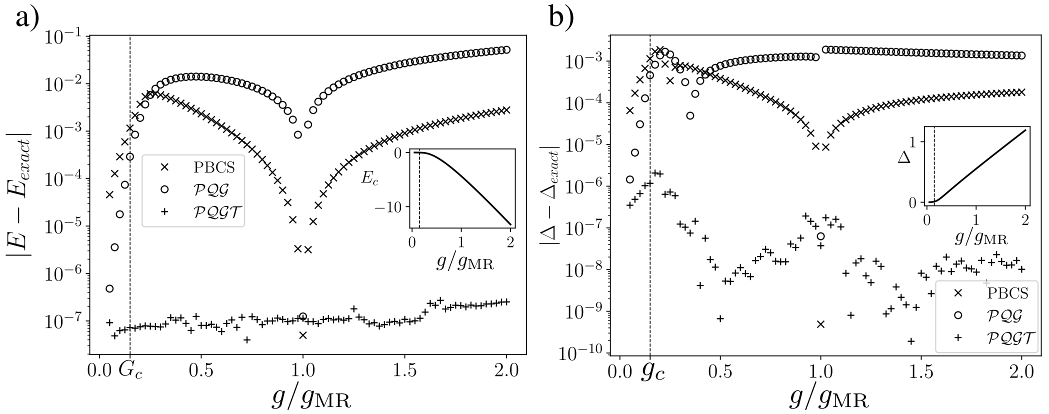

Figure 2.1: (a) Absolute energy difference of the exact ground state energy of the RGK Hamiltonian with $L = 50$, $M = 25$ with respect to the vRDM-DOCI computed with the $\mathcal{PQG}$ and $\mathcal{PQGT}$ conditions and a variational PBCS ansatz. (Inset of a) Exact correlation energy. (b) Absolute difference with respect to the exact canonical gap. (Inset of b) Exact canonical gap.

accuracy around two orders of magnitude lower than PBCS. Both methods achieve great accuracy in the weak coupling region $g < g_c$ below the critical interaction g_c [See Section 1.3.2]. In contrast, imposing the $\mathcal{PQGT}$ conditions returns the exact energy within the numerical error $\delta = 10^{-7}$ of the method for all values of the interaction. In the Inset of Figure 2.1(a) we show the correlation energy

$$E_c = \langle\psi|H|\psi\rangle - \langle\phi_0|H|\phi_0\rangle \tag{2.75}$$

with $|\phi_0\rangle$ the ground state of the non interacting Hamiltonian $H(g = 0)$.

In Figure 2.1(b) we show the absolute difference of the canonical gap (1.34) computed with the vRDM-DOCI method and the PBCS ansatz with respect to the exact one computed with the RG equations

$$\Delta_c = g \sum_k \sqrt{\eta_k} \sqrt{P_{kk}\left(1 - P_{kk}\right)}. \tag{2.76}$$

As in the case of the energy, both the $\mathcal{PQG}$ conditions and the PBCS ansatz perform poorly in the strong coupling regime $g > g_c$, while the $\mathcal{PQGT}$ conditions are able to capture the exact value of the gap within vRDM-DOCI precision. The Inset of Figure 2.1(b) shows the exact canonical gap, which is

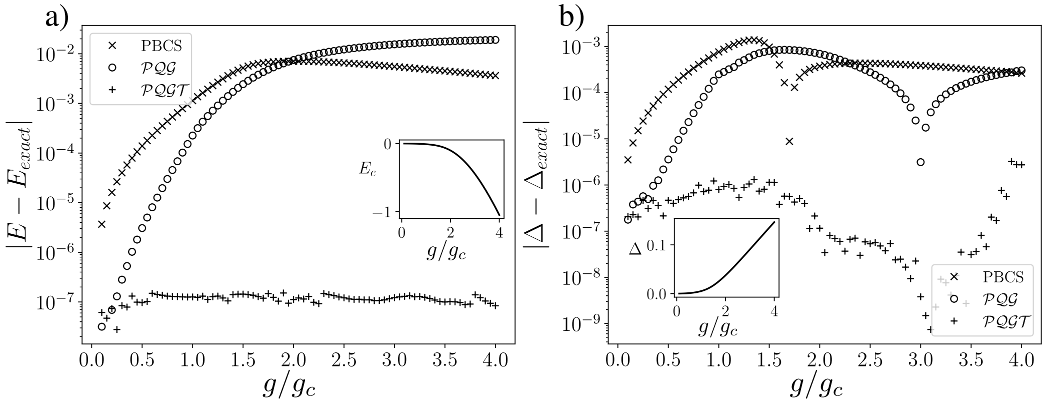

Figure 2.2: (a) Absolute energy difference of the exact ground state energy of the reduced BCS Hamiltonian with $L = 50$, $M = 25$ with respect to the vRDM-DOCI computed with the $\mathcal{PQG}$ and $\mathcal{PQGT}$ conditions and a variational PBCS ansatz. (Inset of a) Exact correlation energy. (b) Absolute difference of the exact canonical gap. (Inset of b) Exact canonical gap.

zero in the weak coupling regime and becomes finite in the superconducting phase $g > g_c$.

2.5.2 The reduced BCS Hamiltonian

We can also benchmark the vRDM-DOCI method by studying the ground state energy and canonical gap of the reduced BCS Hamiltonian or constant pairing model (1.24). We focus on a variation of this Hamiltonian used to study superconductivity in ultra small metallic grains [42, 43]

$$H = \sum_{i=1}^{L} \varepsilon_i \frac{n_i + n_{\bar{i}}}{2} - g \sum_{ij=1}^{L} c_i^\dagger c_{\bar{i}}^\dagger c_{\bar{i}} c_i \tag{2.77}$$

with $(i, \bar{i})$ a set of degenerate levels and $\varepsilon_i = i/L$ a set of equidistant single particle levels. The chain has $L = 50$ sites and we study its ground state at half filling $M = 25$.

We show in Figure 2.2(a) the absolute energy difference with respect to the pairing strength around the critical point g_c of the reduced BCS model in the attractive regime. The computations are done with the $\mathcal{PQG}$ and $\mathcal{PQGT}$ conditions and a variational PBCS ansatz. As in the case of the RGK model,

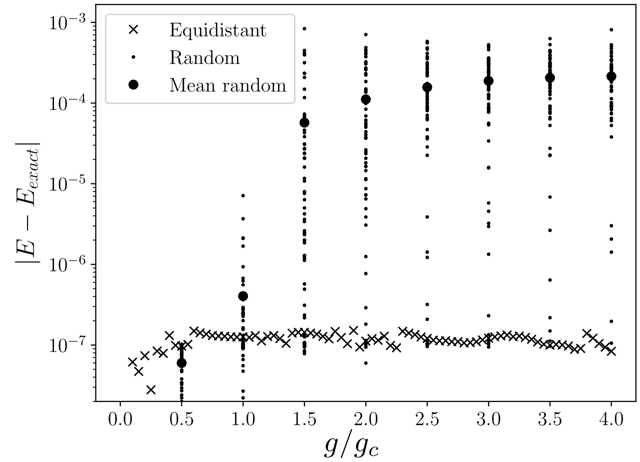

Figure 2.3: Absolute energy difference of the ground state of the reduced BCS model with respect to the pairing interaction for equidistant single particle levels (crosses) and random levels (dots). Results are computed with the $\mathcal{PQGT}$ conditions for a system with $L = 50$ sites and $M = 25$ pairs.

both the $\mathcal{PQG}$ and variational PBCS perform badly in the strong attractive regime, while achieving a high precision in the weak interaction regime. On the other hand, the $\mathcal{PQGT}$ conditions are able to capture the exact energy within the method's precision. We show in the Inset of Figure 2.2(a) the exact correlation energy (2.75). It shows a change of curvature around the critical BCS point that signals the transition from a phase dominated by pairing fluctuations to a superconducting one with condensed Cooper pairs.

Figure 2.2(b) shows the absolute difference of the exact canonical gap computed with respect to the vRDM-DOCI method and the PBCS ansatz. As in the RGK model, the $\mathcal{PQG}$ and PBCS ansatz results are far from the exact canonical gap, while the $\mathcal{PQGT}$ conditions are able to compute it exactly. The Inset of Figure 2.2(b) shows the canonical gap for the reduced BCS model, which opens in the superconducting phase $g > g_c$.

While the previous results achieve a very good precision using the $\mathcal{PQGT}$ conditions, the ability of vRDM-DOCI to provide exact results breaks down when the single particle levels ε_i are not equidistant. This is shown in Figure 2.3, where each sample (dots) represents a Hamiltonian where the single particle levels are drawn from a Gaussian normal ensemble distribution, in comparison with the results for a Hamiltonian with equidistant levels (crosses).

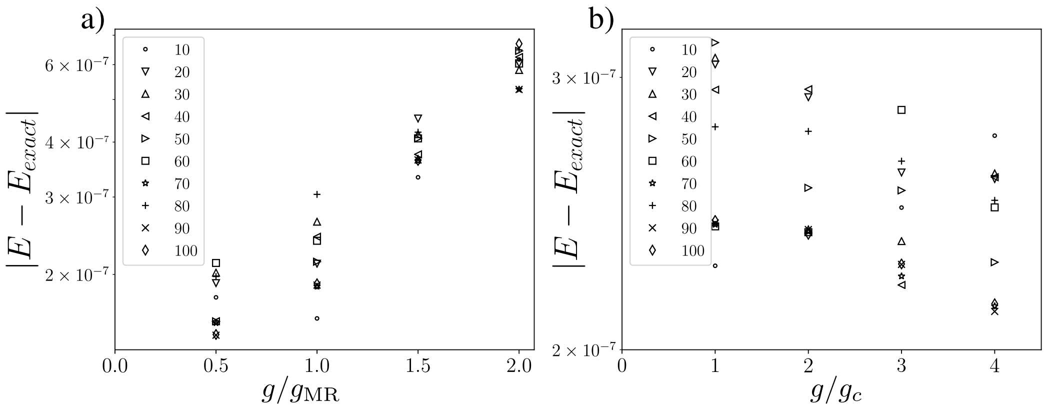

Figure 2.4: Absolute energy difference of the RGK model computed with the $\mathcal{PQGT}$ conditions for different system sizes $L = 10, 20, \ldots, 100$ at half filling.

The results of the $\mathcal{PQGT}$ conditions are exact in the weak coupling regime, $g < g_c$, for all Hamiltonians, while the error becomes larger in the strong attractive regime for random level Hamiltonians. Nevertheless, errors of order $\sim 10^{-4}$ are acceptable for many standards. This breakdown of the vRDM-DOCI method cannot be attributed to a loss of integrability, since the reduced BCS Hamiltonian is still integrable. It could instead be attributed to the complexity of wave functions for non equidistant single particle levels.

2.5.3 Size extensibility of the vRDM-DOCI method

An interesting question is whether vRDM-DOCI is size extensible, i.e. whether or not its accuracy breaks down for large system sizes. To this effect, we benchmark the ground state energy of the RGK and reduced BCS models computed with the $\mathcal{PQGT}$ conditions against the exact energy for different system sizes $L = 10, 20, \ldots, 100$ at half filling. To study systems with $L = 100$ levels using vRDM-DOCI we had to increase the summation error (2.38) to $\delta = 3 \cdot 10^{-7}$, which we set to tha value for all other sizes L. Figure 2.4 shows the energy comparison for different sizes for the RGK Hamiltonian (a) and reduced BCS model with equidistant single particle levels (b). The $\mathcal{PQGT}$ conditions are shown to return the exact energy within the method precision for all sizes, showing that the vRDM-DOCI method is extensible to arbitrary system sizes.

2.5.4 Conclusions

To summarize this section, we have found that imposing the $\mathcal{PQGT}$ conditions leads to an improvement of the vRDM-DOCI method's precision compared to the simpler $\mathcal{PQG}$ conditions. Moreover, we have found several examples for which this method is able to reach the exact ground state of pairing models. We were also able to conclude that this method does not suffer from system's size considerations and its precision holds for many different sizes. However, as we have also seen, the degree of exactness that the $\mathcal{PQGT}$ conditions are able to achieve is highly dependent on the complexity of the wave function.

2.6 The vRDM method using 3-POS conditions

The results from this section are reported in our article: *Variational reduced density matrix method in the doubly occupied configuration interaction space using three-particle N-representability conditions* [111].

In this section we will benchmark the inclusion of the 3-POS conditions of Section 2.4.3 in the computation of ground state properties of molecular systems and repulsive pairing models. Our results show an improvement between one and two orders of magnitude in the ground state energy of molecular systems and half an order of magnitude in the energy of the XXZ chain using the 3-POS conditions with respect to the 2- and (2,3)-POS conditions.

2.6.1 Molecular systems

In general, molecular systems are very different from condensed matter ones. Usually there is no translational symmetry, hoppings and interactions are inhomogeneous and there is often rotational or specular symmetry. As in the general case, the problem of finding the exact solution of the Hamiltonian eigenstates still remains. One method to find approximate solutions to the eigenstates that has enjoyed widespread success in molecular physics is the Configuration Interaction (CI) method [124, 125]. This method considers the basis of the Hilbert space to be made of Slater determinants, which are product states of single particle orbitals, equivalent to single particle wave functions. Because the size of the basis is exponentially large, CI truncates the space of states according to some criteria, e.g. the expectation energy of each basis state. It then proposes a variational wave function ansatz $|\psi(\vec{\alpha})\rangle$ on that truncated space, whose energy it seeks to minimize

$$\min_{\vec{\alpha}} \frac{\langle\psi(\vec{\alpha})|H|\psi(\vec{\alpha})\rangle}{\langle\psi(\vec{\alpha})|\psi(\vec{\alpha})\rangle} \geq E_0, \tag{2.78}$$

with E_0 the exact ground state energy. Because of the Ritz variational principle, this energy is an upper bound to the exact one. For small systems, where it is possible to keep the complete Hilbert space without truncation, this method is called Full CI (FCI) and is equivalent to exact diagonalization.

It becomes evident that the criteria used to truncate the Hilbert space is of huge importance, as it will determine how close the computed ground state can be to the exact one. One of the most used truncation methods builds the state space by taking a set of reference states, for example states computed with Hartree-Fock, and then adding single and double excitations onto those states [124, 125]. Recently [107, 109, 123], there has been some interest in truncating the Hilbert space according to the seniority number (2.40). It has been shown that, generally, the spaces with lowest seniority are able to capture almost all of the correlation energy of the ground state, with the greatest contribution coming from the DOCI zero space. Thus, a good approximation to the ground state can be expected by mapping the molecular Hamiltonian into a pairing Hamiltonian 1.2.1 and then truncating the basis of states into those with a low seniority number.

We have employed several orthonormal basis sets to map the molecular Hamiltonian to a pairing one: natural orbitals (NO), canonical molecular orbitals (CMO), orbitals that minimize the seniority number of the exact wave function ($\mathrm{M_{min}}$) [109] and orbitals that minimize the DOCI energy (OPTE) [126]. Figures 2.5(a-d) show the exact ground state energy after the mapping to a pairing Hamiltonian using CMO orbitals compared with the results using 2-, (2, 3)- and 3-POS conditions for a set of molecules: CO, N_2, CN^- and NO^+. For the NO^+ we also show the computations for a mapping to OPTE orbitals. The energy computed with the 3-POS conditions is, in general, between one or two orders of magnitude closer to the exact DOCI energy for all molecules than when it is only computed with the 2- and (2, 3)-POS conditions. In the case of the NO^+ molecule shown in Figure 2.5(d), while the vRDM-DOCI results for the mapping with OPTE orbitals are similar to the computations with CMO orbitals in the weak interaction regime, the former are two orders of magnitude closer to the exact DOCI

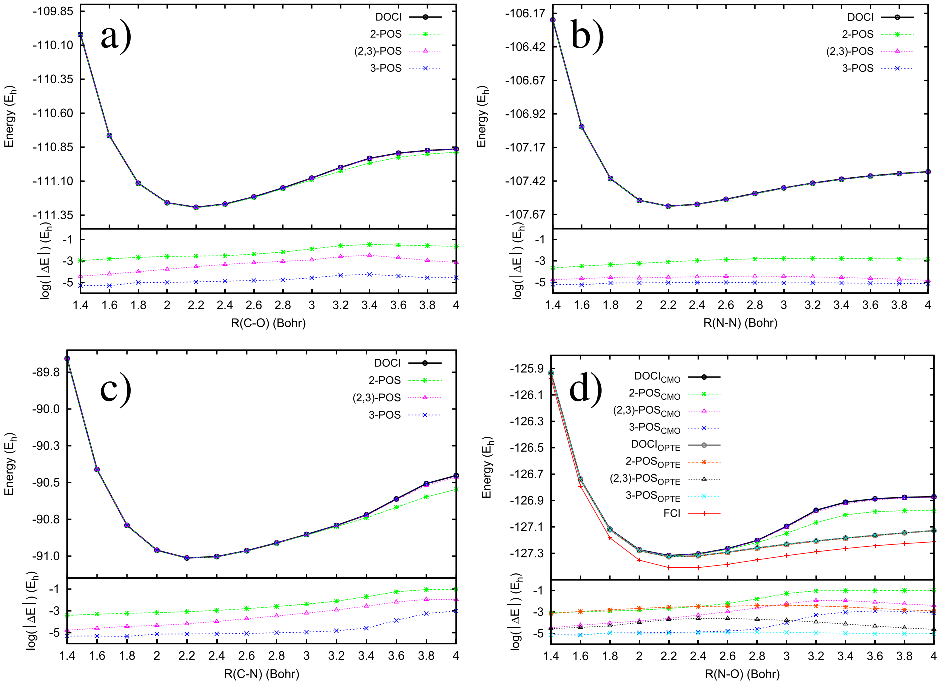

Figure 2.5: Ground state potential energy of the CO (a), N_2 (b), CN^- (c) and NO^+ (d) molecules computed with the Full CI, DOCI and vRDM-DOCI methods. For (a,c) the mapping to the pairing Hamiltonian is done using CMO orbitals and for (d) it is done with CMO and OPTE orbitals. The vRDM-DOCI energies have been computed with the 2-, (2, 3)- and 3-POS conditions. (Bottom panels) Absolute energy error of the vRDM-DOCI method compared to the DOCI energy for each choice of the orbitals.

energy after the potential well. A full comparison between NO, CMO, M_{min} and OPTE orbitals is shown in Table I of Reference [111], which indicates that, in general, the OPTE orbitals are the ones that better approximate the vRDM-DOCI energy to the exact one.

An interesting benchmark of the vRDM-DOCI method is to compare the resulting p-RDM matrices with respect to the exact ones. This is done by measuring the Frobenius norm of the difference of the exact DOCI and vRDM-DOCI results for the Π and D matrices (2.49) of the 2-RDM

$$\begin{aligned} ||\Pi_{\mathrm{DOCI}} - \Pi_{\mathrm{vRDM}}||/L &= \sqrt{\sum_{ij=1}^{L} \left(\Pi_{\mathrm{DOCI},ij} - \Pi_{\mathrm{vRDM},ij}\right)^2 / L} \\ ||D_{\mathrm{DOCI}} - D_{\mathrm{vRDM}}||/L &= \sqrt{\sum_{ij=1}^{L} \left(D_{\mathrm{DOCI},ij} - D_{\mathrm{vRDM},ij}\right)^2 / L}. \end{aligned} \tag{2.79}$$

The distances for the studied molecules are shown in Table III of Reference [111]. In every case the Frobenius distance with respect to the exact DOCI matrices using the 3-POS conditions is of order $10^{-5} - 10^{-6}$ for OPTE and $\mathrm{M}_{\mathrm{min}}$ orbital basis.

2.6.2 Repulsive pairing systems

In the previous section we observed that the (2, 3)-POS, or $\mathcal{PQGT}$, conditions are able to compute the exact ground state energy of the attractive RGK (1.29) and reduced BCS Hamiltonians (1.24) with equidistant single particle levels. However, we noticed that the vRDM-DOCI method cannot compute exact results for attractive constant pairing Hamiltonians with random single particle levels, which were attributed to an increase in the complexity of the wave function. Here we will study a pairing Hamiltonian with repulsive interactions that also displays non exact results using the (2, 3)-POS conditions.

The Hamiltonian is

$$H = \sum_{i=1}^{L} \varepsilon_i n_i + g \sum_{ij}^{L} \sqrt{\varepsilon_i \varepsilon_j}\, b_i^\dagger b_j, \tag{2.80}$$

with L the number of levels, $\varepsilon_i = i/L$ a set of equidistant single particle levels and g the repulsive pairing strength, $g > 0$. This Hamiltonian belongs to the hyperbolic integrability class (1.5).

Figure 2.6 shows the absolute energy error of the exact ground state energy of the repulsive pairing Hamiltonian with respect to the vRDM-DOCI energy. Computations are done for a system with $L = 40$ levels at half filling. In this case, the 3-POS conditions are shown to offer an improvement in the precision of the ground state energy of half an order of magnitude with respect

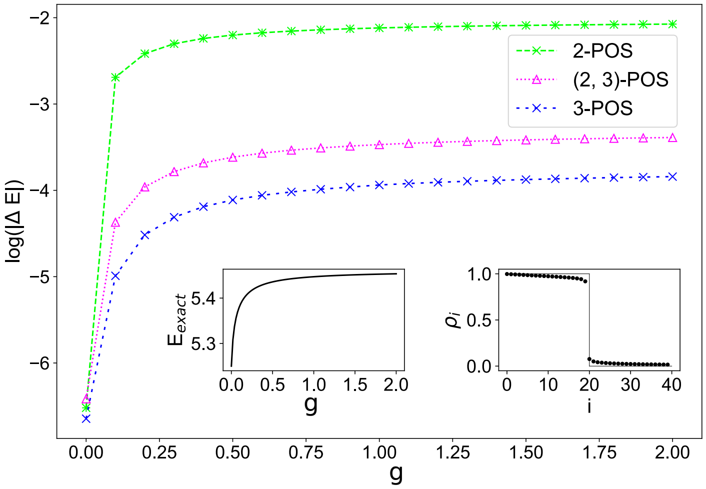

Figure 2.6: Absolute energy error of the ground state energy with respect to the interaction g of the repulsive pairing Hamiltonian computed with the 2-, (2, 3)- and 3-POS conditions. (Left inset) Exact ground state energy. (Right inset) Occupation numbers of the exact ground state at $g = 0$ (solid) and $g = 2$ (dots).

to the (2, 3)-POS conditions. The Insets of Figure 2.6 show the exact ground state energy of the Hamiltonian and the occupation numbers $\rho_i = \langle n_i \rangle$ in a metallic phase, $g = 0$, and a strongly correlated Fermi liquid, $g = 2$.

2.7 vRDM method in the DOCI space using 4-particle N-representability conditions

The results from this section are reported in our article: *Variational reduced density matrix method in the doubly-occupied configuration interaction space using four-particle N-representability conditions: Application to the XXZ model of quantum magnetism* [112].

In this section we benchmark the 4-POS conditions in the integrable 1D Heisenberg XXZ chain. We compare the ground state energy computed with vRDM-DOCI and the computed 2-RDM elements. Our results show an improvement of around one order of magnitude in the precision of the computed observables with respect to the 3-POS conditions. However, the great computational cost of these conditions limits us to studying small size models.

The Heisenberg XXZ Hamiltonian is one of the most studied systems in quantum magnetism [127, 128]. The Hamiltonian is

$$H = \sum_{i=1}^{L} \frac{1}{2} \left(S_i^{+} S_{i+1}^{-} + S_i^{-} S_{i+1}^{+} \right) + \Delta S_i^z S_{i+1}^z \tag{2.81}$$

with L the number of spins, $S_i^{\pm}$ and S_i^z the spin $SU(2)$ operators and Δ an anisotropy factor. In the hard-core boson representation (1.22) this Hamiltonian is written as

$$H = \Delta \left(\frac{L}{4} - M \right) + \sum_{i=1}^{L} \left[\frac{1}{2} \left(b_i^{\dagger} b_{i+1} + b_{i+1}^{\dagger} b_i \right) + \Delta n_i n_{i+1} \right], \tag{2.82}$$

with M the number of hard-core bosons (or fermionic pairs) in the system. This model has a rich phase diagram with a ferromagnetic phase for $\Delta < -1$, an antiferromagnetic phase for $\Delta > 1$ and a gapless critical antiferromagnet in between these phases, $-1 < \Delta < 1$. The XXZ model is an integrable model whose exact solutions can be computed with Bethe ansatz [127].

At $\Delta = -1$ the Hamiltonian can be written as a positive linear combination of projection operators made out of the killers of the ground state B_i

$$H_{-1} = -\frac{L}{4} + \frac{1}{2} \sum_{i=1}^{L} B_i^{\dagger} B_i, \quad B_i = a_{\bar{i}+1}^{\dagger} a_i - a_{\bar{i}}^{\dagger} a_{i+1}, \tag{2.83}$$

with $a_i^{\dagger}$, a_i the fermionic creation and annihilation operators and $(i, \bar{i})$ a set of pairwise degenerate levels. The fermionic operators are related to the hard-core bosons by the mapping (1.22). The ground state of this Hamiltonian is a PBCS state

$$|\psi_{-1}\rangle = \left[\sum_{i=1}^{L} (-1)^i b_i^{\dagger} \right]^M |0\rangle, \quad B_i |\psi_{-1}\rangle = 0, \ \forall i, \tag{2.84}$$

which is annihilated by the killers of the Hamiltonian. Therefore, the vRDM-DOCI method can compute the exact ground state energy at $\Delta = -1$.

Figure 2.7 shows the absolute energy error per particle pair of the XXZ model with respect to the anisotropy factor Δ for a system of $L = 12$ sites at

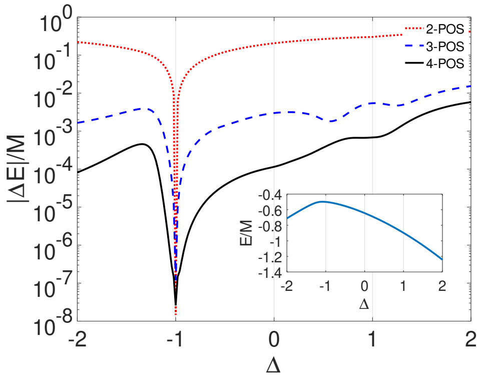

Figure 2.7: Absolute energy error per particle pair of the exact ground state energy of the XXZ Hamiltonian with respect the energy computed with the 2-, 3- and 4-POS conditions. (Inset) Exact energy with respect to Δ.

half filling. The energy is computed using the 2-, 3-, and 4-POS conditions and exact diagonalization. In this case, the 4-POS conditions represent an improvement with respect to the 3-POS ones in the precision of the computed energy of about one order of magnitude in the ferromagnetic $\Delta < -1$ and critical antiferromagnetic $-1 < \Delta < 1$ phases, while the improvement is of a factor ~ 5 in the antiferromagnetic phase $\Delta > 1$. The Inset shows the exact ground state energy of the Hamiltonian.

Figure 2.8 shows the Frobenius distance (2.79) between the 2-RDM computed with the vRDM-DOCI method and the 2-RDM computed with exact diagonalization. The matrices Π and D computed with 4-POS conditions show and improvement over the 3-POS conditions of between one and two orders of magnitude in most of the spectrum. However, for the D matrix, there is almost no improvement around $\Delta = 1/2$ and for $\Delta > 1$, which can be attributed to the complexity of the wave function in these regions.

To summarize, we have shown that the 4-POS conditions follow the same trend of improving the precision of the computed ground state energy and 2-RDM elements by an order of magnitude or two with respect to the previous 3-POS conditions. In general, this shows a behaviour in which imposing further p-POS conditions keeps improving the vRDM-DOCI results by one or two orders of magnitude at each step.

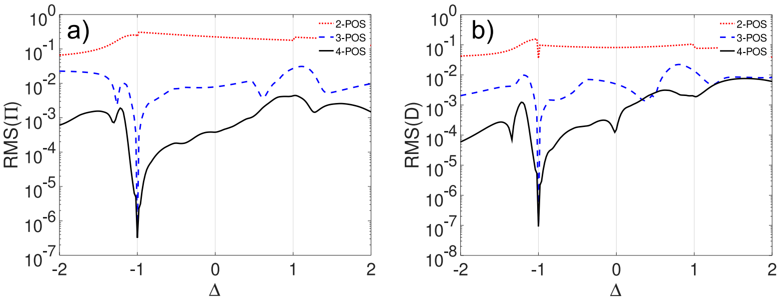

Figure 2.8: Frobenius distance between the exact Π (a) and D (b) 2-RDM matrices of the XXZ model and those computed with the 2-, 3- and 4-POS conditions.

2.8 The Inozemtsev model

In the previous sections we studied examples of integrable models like the RGK or the reduced BCS models. For these systems we found that the vRDM method can compute the exact ground state energy in some special cases and a very good approximation in the general case. Here we will study the Inozemtsev model [129], which is a parametrization between two integrable models, the Haldane-Shastry model [130, 131] and the isotropic XXX Heisenberg chain ($\Delta = 1$). Between these extrema the model is also integrable [132], although no solutions have been found yet.

The Inozemtsev Hamiltonian for a circular chain of L sites as the one illustrated in Figure 2.9(a) is

$$H = \sum_{i \neq j} \frac{1}{\operatorname{sn}\left(\frac{2(i-j)K(m)}{L}, m\right)^2} \vec{S}_i \cdot \vec{S}_j, \quad m \in [0,\, 1] \tag{2.85}$$

with $K(\cdot)$ the complete elliptic integral of the first kind and $\operatorname{sn}(\cdot,\cdot)$ the Jacobian elliptic sine function. The limit $m = 0$ corresponds to the Haldane-Shastry model and the denominator becomes proportional to the squared distance d_{ij} between sites i, j. On the other hand, the limit $m = 1$ corresponds to the Heisenberg XXX chain and the Hamiltonian has only nearest neighbour terms $\vec{S}_i \cdot \vec{S}_{i+1}$.

Figure 2.9(b) shows the absolute energy difference of the Inozemtsev ground state energy of a chain of $L = 10$ sites with zero net magnetization $S^z = 0$ with respect to the energy computed with the (2,3)-, 3- and 4-POS

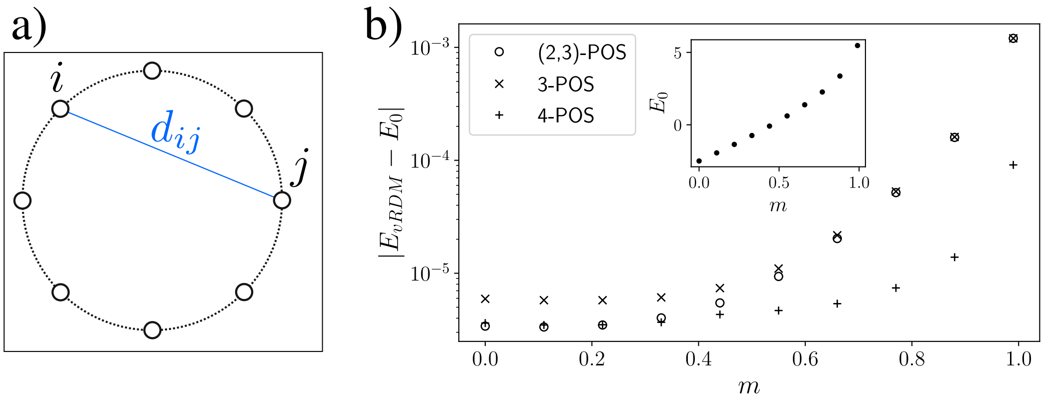

Figure 2.9: (a) Sketch of the circular chain of the Inozemtsev model. d_{ij} is the distance between two points of the chain. (b) Absolute energy difference of the ground state of the Inozemtsev model with respect to the energy computed with the (2,3)-, 3- and 4-POS conditions. (Inset) Exact ground state energy with respect to m.

conditions. The ground state of the Haldane-Shastry model is annihilated by a set of two-body killers, with which the Hamiltonian can be written as a sum of semidefinite positive operators [133]. Therefore, the vRDM method returns the exact energy in the limit $m = 0$ already with the (2, 3)-POS conditions. For $m > 0$, the computed energy is exact until $m \sim 0.5$. At $m = 1$ the vRDM-DOCI method results coincide with those computed for the Heisenberg XXZ chain with $\Delta = 1$ in Section 2.7. The Inset of Figure 2.9 shows the exact ground state energy of the model. Our results for the integrable Inozemtsev model support the hypothesis that the integrability of a system does not make it exactly solvable by the vRDM-DOCI method.

2.9 Computational cost of the vRDM-DOCI method

As we have seen in the previous sections, imposing successively the 2-, 3- and 4-POS conditions allow us to compute the ground states of relevant physical systems at a precision comparable to other standard numerical methods. However, we must take into account that the number of p-POS conditions imposed into the vRDM-DOCI algorithm can greatly increase its computa-

N-rep conditions	2-POS	3-POS	4-POS
Number of RDM elements	$\mathcal{O}\left(L^2\right)$	$\mathcal{O}\left(L^3\right)$	$\mathcal{O}\left(L^4\right)$
Computational scaling	$L^{2.01}$	$L^{5.00}$	$L^{7.43}$
Maximum reachable size	100	50	20

Table 2.1: Order of the number of elements in each of the p-RDM, fitted asymptotical time scaling of the vRDM-DOCI method with different p-POS conditions and maximum system size L that one can study with each p-POS condition.

tional cost. In this section we study how does the computational time of the vRDM-DOCI method depend on the number of p-POS conditions and what is the maximum size of the systems that it can compute. In general, we find that the algorithm is usually constrained by its time requirements and the maximum reachable system sizes are $L = 50$ when the 3-POS conditions are imposed and $L = 20$ for 4-POS conditions.

We have focused on the ground state properties of molecular systems, models of quantum magnetism and RG integrable pairing models. To solve the semidefinite programming problem we employed the SemiDefinite Programming Algorithm (SDPA) script [118, 119], which is a highly optimized C++ program that relies on the sparsity pattern of the semipositivity conditions and multithreading to lower the computational time required to solve the semidefinite problem. In general, the SDPA bottleneck lies on solving a linear system whose dimensions are the same as the number of variational parameters we are taking into account [119]. Therefore, the performance of our numerical computations is limited by the number of elements of the p-RDMs for which we are imposing semipositivity conditions.

To study the computational cost of the vRDM-DOCI method we compute the ground state energy of the XXZ Hamiltonian at half filling for different sizes $L = 12, 14, 16, 18$ and with respect to different p-POS conditions. For every set of p-POS conditions we measure the time that our computers require to finish one iteration of the SDPA algorithm and perform a linear fit with an exponential reference function $t(L) = \exp\left(\alpha + \beta L\right)$ to observe the scaling with the system size L.

Table 2.1 shows the number of elements in each of the p-RDM matrices, the fitted time scaling of the p-POS conditions and the maximum system size L that one can reach with each of the conditions. This computations were run single threaded on an Intel Xeon E5-2650v2 computer. We conclude that the scaling of the computational time is highly correlated with the number of elements of the p-RDM. Unfortunately, when using the 4-POS conditions, $L \sim 20$ sites is something that can be easily achieved by exact diagonalization, forcing us to find new strategies to reduce the computational time for these conditions.

2.10 Symmetries in the DOCI subspace

The computational cost of the vRDM-DOCI method is related to the number of p-RDM matrix elements of the conditions that are imposed, setting a fundamental limit in the sizes that can be studied. Fortunately, many condensed matter models have a two underlying symmetries that can help reduce the time scaling of vRDM-DOCI: translational invariance and reflection symmetry.

The most usual symmetry that appears in the 1D models that we have studied is translational symmetry. For the p-RDM this means that elements whose indices are shifted by a constant amount with respect to other index have an equal observable. As an example, the occupation numbers and correlation expectation values satisfy the following relations

$$\begin{aligned} \langle n_i \rangle &= \rho_i = \rho_1, \quad i = 1, \ldots, L \\ \langle b_i^\dagger b_j \rangle &= \Pi_{ij} = \Pi_{1,1+j-i}, \quad i, j = 1, \ldots, L. \end{aligned} \tag{2.86}$$

In general, for 1D systems of size L, translational invariance lets us to reduce the number of p-RDM elements by a factor of L.

Another symmetry of relevance is reflection symmetry, by which the Hamiltonian remains invariant if the site indices are reflected with respect to a fixed one. For the same observables as before, the symmetry relations between different elements of the p-RDM are

$$\begin{aligned} \langle n_i \rangle &= \rho_i = \rho_{a-i}, \quad i = 1, \ldots, L \\ \langle b_i^\dagger b_j \rangle &= \Pi_{ij} = \Pi_{a-i,a-j}, \quad i, j = 1, \ldots, L, \end{aligned} \tag{2.87}$$

with a a site index with respect to which all other indices are reflected.

The reflection symmetry together with translational symmetry have important consequences for the scaling of the vRDM-DOCI computations. For 1D systems with both symmetries the number of independent terms in the 2-, 3- and 4-RDMs is reduced by a factor of $2L$ and for 2D square lattices this reduction is of order $4L^2$. Furthermore, these symmetries imply that many DOCI semipositivity conditions are equivalent. As an example, this is the case of the 2-particle $\mathcal{G}$ conditions for 1D chains

$$G_{ab} = \begin{pmatrix} \rho_a - D_{ab} & -P_{ab} \\ -P_{ab} & \rho_b - D_{ab} \end{pmatrix} = G_{1,1+b-a} \succeq 0, \quad \forall\ a < b. \tag{2.88}$$

While not all semipositivity conditions have a similar reduction in number, we find that the overall number of conditions is reduced by an order of $\sim L$ for 1D systems and $\sim L^2$ for square 2D ones. These reductions, of both the number of terms and semipositivity conditions, allow us to study 1D systems with 2- and 3-POS conditions up to $L = 256$ sites (compared with a maximum of $L = 50$ for the 3-POS conditions without symmetries) and systems with 4-POS conditions up to $L = 30$ sites (compared to $L \sim 20$). For 2D square lattices we are able to compute $L = 16 \times 16$ lattices with 3-POS conditions and $L = 6 \times 6$ lattices with 4-POS conditions.

2.11 Exploiting translational and reflection invariance with the 4-POS conditions

The results from this section are reported in our article: *Variational determination of the two-particle reduced density matrix within the doubly occupied configuration interaction space: exploiting translational and reflection invariance* [113].

In this section we analyze how including the symmetries of the model in the p-POS conditions can decrease the computational cos of the vRDM-DOCI method. The method is applied to the 1D and 2D Heisenberg XXZ chain, which has translation and reflection invariance. Our results show that incorporating the symmetries into the N-representability conditions has the same precision in computing the ground state properties as without symmetries but with the additional advantage that we can study systems with medium and large sizes.

We start with a modification of the Heisenberg XXZ Hamiltonian in the hard-core boson representation valid for any number of dimensions

$$H = \Delta\, z \left(\frac{L}{4} - M\right) + \sum_{\langle ij \rangle}^{L} \frac{1}{2} \left(b_i^\dagger b_j + \text{h.c.}\right) + \Delta n_i n_j, \tag{2.89}$$

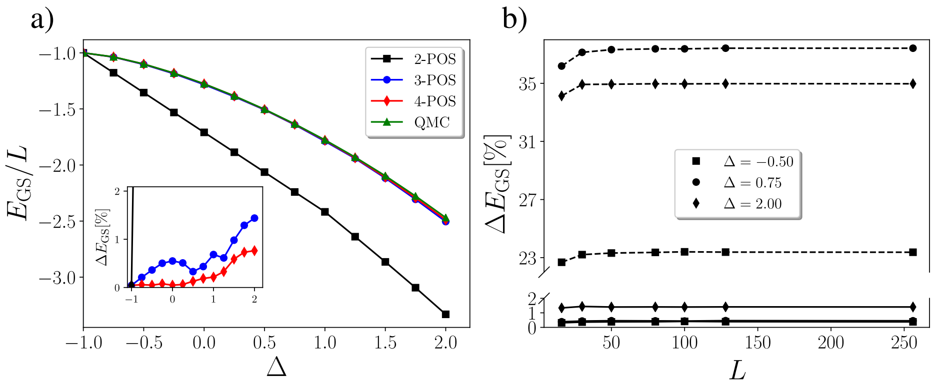

Figure 2.10: (a) Ground state energy per site of the 1D XXZ Hamiltonian with respect to Δ computed with the 2-, 3- and 4-POS conditions and QMC. (Inset of a) Relative energy error with respect to the QMC energy. (b) Relative energy error with respect to the QMC energy for different 1D lattice sizes L and for different Δ values for the 2-POS (dashed) and 3-POS (solid) conditions.

with $\langle ij \rangle$ a summation over first neighbour sites and z the number of first neighbours in the lattice. For the 1D case, there is a ferromagnetic phase at $\Delta < -1$, an antiferromagnetic phase at $\Delta > 1$ and a critical antiferromagnet with gapless excitations at $-1 < \Delta < 1$. In 2D there is a similar phase diagram with the $\Delta = -1, +1$ points separating the ferromagnetic, critical gapless ferromagnet and antiferromagnetic phases [134]. Importantly, the XXZ Hamiltonian preserves both translational and reflection symmetry for 1D and 2D lattices.

Figure 2.10(a) shows the ground state energy of the 1D XXZ Hamiltonian of a chain of $L = 30$ sites at half filling with respect to Δ computed with the 2-, 3- and 4-POS conditions using symmetry reductions. We also compute the ground state with the Quantum MonteCarlo (QMC) method, which we consider as a quasi exact energy. The relative energy of the vRDM-DOCI method with respect to the QMC energy is shown in the Inset of Figure 2.10(a), indicating that the energy computed with the 3- and 4-POS conditions has a relative accuracy below 1% in the critical antiferromagnetic phase $-1 < \Delta < 1$ and a relative accuracy of order of 1% in the antiferromagnetic phase $\Delta > 1$. In Figure 2.10(b) we show the energy computed with vRDM-DOCI with respect to different system sizes L and for different

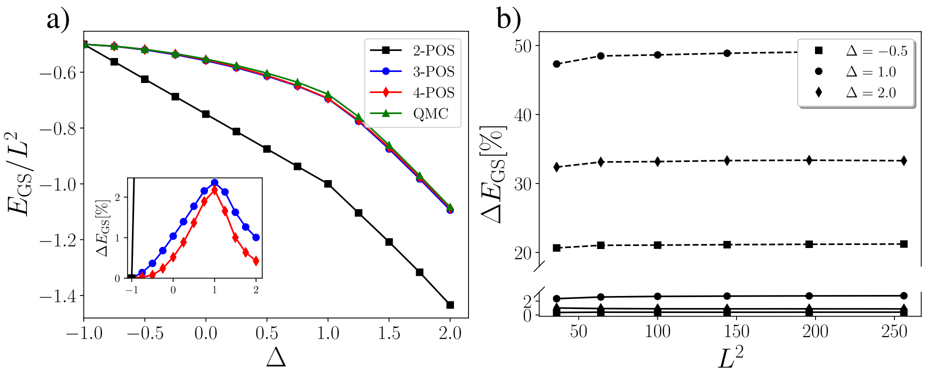

Figure 2.11: (a) Ground state energy per site of the square 2D XXZ Hamiltonian with respect to Δ. Results are shown for the 2-, 3- and 4-POS conditions and QMC. (Inset of a) Relative energy error with respect to the QMC energy. (b) Relative energy error with respect to the QMC energy for different 2D square lattice sizes and for different Δ values computed with the 2-POS (dashed) and 3-POS (solid) conditions.

Δ. This energy converges in the large size limit, further demonstrating the size extensibility of the vRDM-DOCI method with 3- and 4-POS conditions and symmetry reduction.

Figure 2.11(a) shows the ground state energy of the 2D square XXZ Hamiltonian with $L = 6 \times 6$ sites at half filling computed with the 2-, 3- and 4-POS conditions and QMC. Our results show a relative accuracy below 1% for the 3- and 4-POS conditions when the anisotropy term is negative and a sudden loss of precision around the critical point $\Delta = 1$. We show in Figure 2.11(a) the stability of the vRDM-DOCI energy results for large 2D square lattice sizes computed with the 2- and 3-POS conditions, which converge in the large size limit.

In order to assess the validity of the vRDM-DOCI method for studying ground state properties we also compute the spin correlation functions of the XXZ model. In terms of the hard-core boson representation they read

$$\begin{aligned} \langle S_i^x S_j^x \rangle = \langle S_i^y S_j^y \rangle &= \frac{1}{2}\langle b_i^\dagger b_j \rangle + \delta_{ij}\left(\frac{1}{2} - \langle n_i \rangle\right) \\ \langle S_i^z S_j^z \rangle &= \langle n_i n_j \rangle - \frac{1}{2}\langle n_i + n_j \rangle + \frac{1}{4}. \end{aligned} \tag{2.90}$$

For a 1D chain we show in Figure 2.12 the $\langle S_i^z S_j^z \rangle$ correlations that indicate

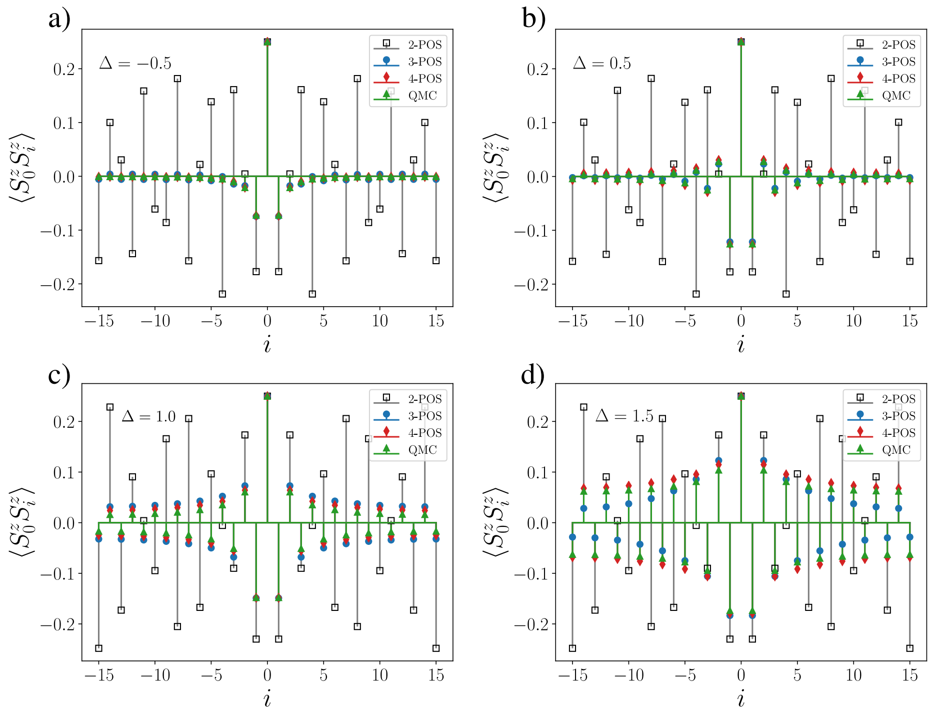

Figure 2.12: Spin $\langle S_0^z S_i^z \rangle$ correlations of the 1D XXZ Hamiltonian for different values of the anisotropy parameter Δ. Results are computed with the 2-, 3- and 4-POS conditions and QMC.

the ferromagnetic or antiferromagnetic character of the individual phases. These are computed with the 2-, 3- and 4-POS conditions and QMC at four different values of the anisotropy Δ. The chain has $L = 30$ sites and we consider a half filled ground state. Because the model has translational and reflection invariance, the $\langle S_0^z S_i^z \rangle$ observables represent all possible ZZ correlations. All p-POS conditions are able to infer the antiferromagnetic character $\langle S_i^z S_{i+1}^z \rangle < 0$ for their respective Δ parameters. However, only the 3- and 4-POS conditions are able to capture the exact quantitative form of the quasi exact ZZ correlations computed with the QMC method. For strong antiferromagnetic interactions, $\Delta = 1.5$, only the 4-POS conditions are able to capture the long range behaviour of the correlations.

Figure 2.13 shows the first and second neighbour correlations $\langle S_0^z S_{1,2}^z \rangle$, $\langle S_0^x S_{1,2}^x \rangle$ for different values of the anisotropy Δ of the 2D square XXZ Hamiltonian with sizes $L = 6 \times 6$ (a,c) and $L = 16 \times 16$ (b,d) at half filling. The

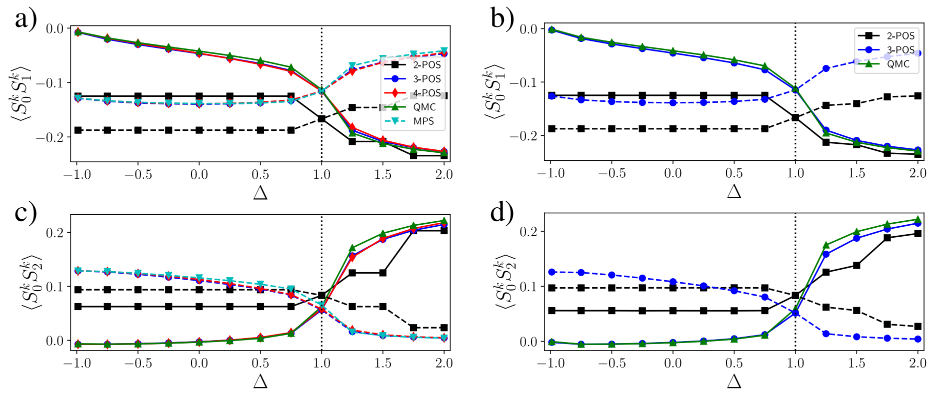

Figure 2.13: First and second neighbour correlations $\langle S_0^k S_1^k \rangle$ and $\langle S_0^k S_2^k \rangle$ of the 2D square XXZ Hamiltonian with $L = 6 \times 6$ (a,c) and 16×16 (b,d) sites with respect to Δ. The solid lines represent $k = z$ correlations and dashed lines the $k = x$ correlations.

correlations were computed using the 2-, 3- and 4-POS conditions, QMC and for the XX correlations also a Matrix Product State (MPS) ansatz. We consider these two methods to be quasi exact for 6×6 spin lattices and QMC a good solution for a 16×16 lattice. Our results show that the 3- and 4-POS conditions can reproduce the first and second neighbour correlations with a high degree of accuracy.

To summarize, we have been able to overcome the size limit of the vRDM-DOCI method for the 3- and 4-POS conditions with the help of translation and reflection symmetries. We were able to extend our computations with the 3-RDM method from systems of $L = 50$ sites to $L = 256$ (or $L = 16 \times 16$ for 2D lattices). Similarly, we increased the size limit for the 4-POS conditions from $L = 20$ to $L = 36$ or $L = 6 \times 6$ sites. Our results suggest that a more careful study of the underlying symmetries of the studied system can greatly increase the level of precision with which we can study their properties. As the one of the most promising candidates for future studies stands the rotational symmetry for 2D lattices with triangular, square or hexagonal configurations.

2.12 Conclusions

The exponential growth of the dimension of the Hilbert space with the length of a physical system imposes a fundamental limit into what extent a system can be studied with arbitrary precision. Contrary to many other numerical methods, the vRDM method avoids this problem altogether by focusing on the p-RDM rather than on the wave function of the system. The polynomial scaling of the number of elements of the p-RDM guarantees that there will be no exponential explosion. While this argument attracted a lot of attention into the vRDM method at the advent of quantum mechanics, it was slowly forgotten due to the computational hardship of imposing the N-representability conditions. However, since the works of Nakata *et al.* in the 2000s, vRDM has enjoyed a rebirth due to its reformulation as a semidefinite problem that can be solved with our current computational capacity. Apart from that, the reformulation of the N-representability conditions in the DOCI subspace has also represented a new era for vRDM in which much larger systems can be studied with an improved precision.

Travelling on this wave of success, we were first able to correctly benchmark the well known DOCI 2-POS and (2, 3)-POS conditions using integrable pairing Hamiltonians based on Richardson-Gaudin models, such as the Richardson-Gaudin-Kitaev or the reduced BCS Hamiltonian. In our work we were able to identify the great improvement in accuracy that the DOCI (2, 3)-POS conditions represented over the simpler 2-POS. The precision of the method was even found to be exact for several particular systems, which we hypothesize might be due to the form of the underlying wave function.

In subsequent works we were able to include the 3- and 4-POS conditions to the method. We showed the improved precision that the new conditions could achieve by analysing systems of great interest, such as molecular structure problems, pairing Hamiltonians and models of quantum magnetism. The achieved relative precision is between $1 - 0.1\%$ of the exact ground state energy for the Heisenberg chain and around $10^{-5}\%$ for molecular systems, which make the vRDM-DOCI method competitive with other state-of-the-art numerical methods. Furthermore, we also demonstrated that the elements of the 2-RDM computed with vRDM-DOCI, on which many relevant physical observables depend, can also reach similar levels of precision.

The vRDM-DOCI method, however, has a big obstacle when computing large systems with many N-representability conditions due to the big computation times the algorithm requires. As we have seen, adding successive layers of p-RDMs and N-representability conditions quickly increases the number of parameters the algorithm has to deal with. Thus, we are forbidden from studying systems with more that $L = 20$ sites with the DOCI 4-POS conditions. Fortunately, we are able to overcome this problem by implementing different symmetries into the N-representability conditions, which drastically reduces the number of independent p-RDM elements to be computed. Using these symmetry reductions, we were able to study the 1D and 2D Heisenberg XXZ chains with $L = 256$ sites for the 3-POS and with $L = 36$ for the 4-POS conditions.

The vRDM-DOCI method has been shown to be a competitive method that can reach high levels of precision for very large systems at a polynomial cost. However, the rapid evolution of the number of elements of the p-particle DOCI N-representability conditions hinders its ability to escalate the number of particles in the conditions. Our works open the door to improving the method, which might come from the inclusion of new symmetries into the conditions or the discovery of new ones. Among these, similar sets of conditions to the (2, 3)-POS conditions, such as the hypothetical (4, 5)-POS, could help the method reach new heights.

Chapter 3

Topological insulators

3.1 Introduction

The discovery of the integer [135, 136] and fractional [137, 138] quantum Hall effects attracted a big interest as they pointed to new quantum phases of matter. These phases, among other properties, could not be understood within the traditional framework of Landau's phase transitions, displayed novel long range correlation patterns in the structure of their ground states [139] and proved to be resilient against smooth perturbations. Such properties, together with the dependence of the ground state degeneracies on the topology of the embedding space, led to the notion of topological order [140, 141] and to the introduction of a new set of quantum numbers, the topological invariants, to classify these novel phases [139]. The topological nature of these invariants is manifested as they can only take discrete values, much similar to, e.g. the *genus* number of a surface counting the number of holes, which is restricted to the set of natural numbers. Aside from its classification, it was soon realized that topological systems also give rise to interesting edge effects [142, 143], such as gapless edge excitations or protected edge states.

One relevant class of these new quantum phases of matter are topological insulators (TI) [144–146], which are gapped phases of non interacting fermionic models with topologically protected boundary states [147–149]. There is a rich variety of TIs, all of them classified by their symmetries [150–153] and by a topological invariant. Interestingly, this invariant is associated to the *bulk-boundary* correspondence, which states that the net number of localized boundary modes of a TI is directly related to the topology of its bulk. In general, this bulk is band insulating, although localized currents can be induced with a non zero local potential gradient, as we will see in this chapter. On the other hand, the topological nature of TIs implies that one cannot smoothly connect one TI phase with another without closing the gap in the spectrum first, in what is known as a topological quantum phase transition.

Historically, the integer quantum Hall effect was the first class of TI that was discovered. In 1980 von Klitzing reported that immersing a 2D quantum gas of fermions in a large magnetic field B resulted in quantized values of the transverse Hall conductance σ_{xy} [135]. It was soon suggested that this transverse conductance was proportional to a topological invariant, the Chern number ν [154, 155]. For 2D systems, this number is defined as the winding of the Berry phase [156] around the Brillouin Zone (BZ) and is equal to the Thouless-Kohmoto-Nightingale-den Nijs integer [154]. Surprisingly, although the Chern number is defined for infinite systems, non zero Chern numbers are also related to the appearance of boundary modes in finite systems with open boundaries [147, 148, 157]. Precisely, these boundary modes are the ones responsible for the quantized transverse conductance $\sigma_{xy} \propto \nu$ of the integer quantum Hall effect. Moreover, these modes are exponentially localized at the boundaries of the material.

Later, the discovery of the Quantum Spin Hall insulator [158, 159] and several real world candidates for TIs [160–164] drew a lot of interest into this field, which resulted in the classification of TIs according to their symmetry classes [150–153]. Among well known classes of TIs and their respective symmetries are: Chern insulators (CI), to which the integer quantum Hall state belongs and which break time reversal and charge conjugation symmetry (crucial, as the transverse conductance σ_{xy} is antisymmetric with respect to time reversal); Quantum Spin Hall insulators [158, 159], which must explicitly maintain time reversal invariance; or $p_x + ip_y$ superconductors [62], which are charge conjugation invariant.

Inspired by the novel properties of TIs, there has been a growing interest in simulating them in physical platforms, where ultracold atoms trapped in optical lattices [165–167] have taken the lead due to the high degree of experimental purity that they can offer. In such experiments, a sample of ultracold neutral atoms is loaded inside a laser field that traps the atom cloud inside it and, at the same time, creates an effective Hamiltonian of our choosing for the atoms that can simulate a rich variety of physically relevant models. Using the electronic transitions of the atoms or Floquet engineering, it is possible to simulate artificial gauge fields for the neutral atom cloud [168–170], reaching regimes that are comparable to von Klitzing's original experiments. It is now feasible to simulate topological systems in ultracold atoms, such as the Hofstadter Hamiltonian [171], the SSH chain [172], the Haldane model [170] or the Creutz ladder model [173].

In Section 3.2 we introduce the Haldane model [174], one of the first discovered examples of a CI, and study its ground state and topological classification. Section 3.3, based on our article *Topological phases in the Haldane model with spin-spin on-site interactions* [175], examines what happens to the topological quantum phases of two spinful copies of the Haldane model in the presence of spin-spin on-site interactions [175], the so called Haldane-Hubbard model, where our results indicate a survival of the topologically non trivial phase until relatively large values of the interactions. In Section 3.4 we tackle the emergence of localized states and currents at the edges of TI with open boundary conditions, while Section 3.5 deals with inhomogeneous potentials in TIs and the emergence of localized states and currents in the bulk of the system. This is studied using a simple perturbation theory analysis of the mode $p = \pi$ of the Haldane model on a cylinder and with exact diagonalization of all Hamiltonian modes on the cylinder. The results of this Section are reported on our article *Topological bulk states and their currents* [176]. Section 3.6 covers the implementation of TI models in ultracold atoms setups and proposes two experimental implementations that can be done with state-of-the-art techniques. The first one of these is the implementation and measurement of the Chern number in the Haldane-Hubbard model and the second one is the measurement with time of flight images of the localized bulk and edge currents in the Haldane model subject to an harmonic potential trap. For the latter we show numerical simulations supporting the observation of currents in our proposal, which are reported in our article *Seeing topological edge and bulk currents in time-of-flight images* [177]. Finally, Section 3.7 is reserved for conclusions.

3.2 The Haldane model

The Haldane model [174] is one of the first discovered examples of a TI. In his work, Haldane presented a realization of the integer quantum Hall effect that has a non zero Hall conductance σ_{xy} by breaking time reversal symmetry but, contrary to expected, without any net magnetic field. In the literature, this way of realizing the integer quantum Hall effect without magnetic field is usually called anomalous quantum Hall effect. This model has a topologically trivial phase with $\nu = 0$, which we will refer to as the trivial or trivial insulator phase, and two topologically non trivial phases with $\nu = \pm 1$, which we call the topological or the CI phases. In general, a CI phase is one with $\nu \neq 0$. These phases have a quantized non zero Hall conductance related to the value of the Chern number $\sigma_{xy} = \nu e^2/h$ and, if the model is placed in a finite system with open boundaries, it displays gapless boundary modes localized along them.

The Haldane model is related to the much simpler graphene Hamiltonian, which is embedded in an hexagonal lattice composed of two triangular sublattices A and B. This lattice is shown as a sketch in Figure 3.1. The displacement vectors between unit cells are

$$\mathbf{a}_1 = \frac{a}{2}\left(3, \sqrt{3}\right), \quad \mathbf{a}_2 = \frac{a}{2}\left(3, -\sqrt{3}\right), \tag{3.1}$$

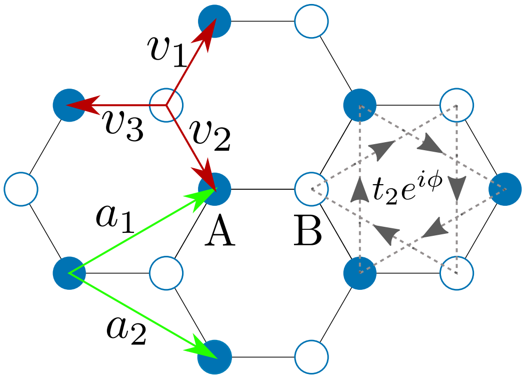

Figure 3.1: Sketch of the hexagonal lattice of the Haldane model. Blue and white points correspond to the A and B sublattices, respectively. Green arrows illustrate the translation vectors between unit cells and red arrows the translations between sublattices. The dashed arrows correspond to the direction of the positive phase $t_2e^{i\phi}$ hoppings.

with a the lattice separation between nearest neighbour sites. The translation vectors between the two sublattices are

$$\mathbf{v}_1 = \frac{1}{2}\left(1, \sqrt{3}\right), \quad \mathbf{v}_2 = \frac{1}{2}\left(1, -\sqrt{3}\right), \quad \mathbf{v}_3 = \frac{1}{2}\left(-1, 0\right). \tag{3.2}$$

The BZ corresponding to this lattice is formed by a parallelogram defined by the reciprocal lattice vectors

$$\mathbf{b}_1 = \frac{2\pi}{3a}\left(1, \sqrt{3}\right), \quad \mathbf{b}_2 = \frac{2\pi}{3a}\left(1, -\sqrt{3}\right), \tag{3.3}$$

which satisfy $\mathbf{a}_i \cdot \mathbf{b}_j = 2\pi\delta_{ij}$. In the following we set $a = 1$ without loss of generality.

The Haldane Hamiltonian extends this model by adding a time-reversal breaking next-nearest neighbour hopping t_2 and an inversion symmetry breaking on-site potential ϵ

$$\begin{aligned} H = &- t_1 \sum_{\langle ij \rangle} \left(a_i^\dagger b_j + \text{h.c.}\right) - t_2 \sum_{\langle\langle ij \rangle\rangle} \left(e^{i\nu_{ij}\phi} a_i^\dagger a_j + e^{-i\nu_{ij}\phi} b_i^\dagger b_j\right) \\ &- \epsilon \sum_i \left(a_i^\dagger a_i - b_i^\dagger b_i\right) \end{aligned} \tag{3.4}$$

Here, $a_i^\dagger$, $b_i^\dagger$ are the fermion creation operators in the A and B triangular sublattices, $\langle ij \rangle$, $\langle\langle ij \rangle\rangle$ are pairs of nearest and next-nearest neighbour sites and t_1 is the nearest neighbour hopping. Time reversal is broken by the complex phase ϕ whose sign $\nu_{ij} = \pm 1$ can be interpreted as the direction of the hopping [See Figure 3.1] and inversion symmetry is broken by the sublattice imbalance term ϵ. In momentum space, the Haldane Hamiltonian reads

$$\begin{aligned} H = & -t_1 \sum_{\mathbf{k}\mathbf{v}_i} \left(e^{i\mathbf{k}\mathbf{v}_i} a^\dagger_{\mathbf{k}} b_{\mathbf{k}} + \text{h.c.} \right) - \epsilon \sum_{\mathbf{k}} \left(a^\dagger_{\mathbf{k}} a_{\mathbf{k}} - b^\dagger_{\mathbf{k}} b_{\mathbf{k}} \right) \\ & - t_2 \sum_{\mathbf{k}\mathbf{v}_i^2} \left[\cos\left(\phi + \mathbf{k}\mathbf{v}_i^2\right) a^\dagger_{\mathbf{k}} a_{\mathbf{k}} + \cos\left(\phi - \mathbf{k}\mathbf{v}_i^2\right) b^\dagger_{\mathbf{k}} b_{\mathbf{k}} \right], \end{aligned} \tag{3.5}$$

with $\mathbf{v}_i^2 = -\mathbf{a}_1, \mathbf{a}_2, \mathbf{a}_1 - \mathbf{a}_2$ translations inside sublattices. Introducing the pseudospin operators $\sigma^x_{\mathbf{k}} = a^\dagger_{\mathbf{k}} b_{\mathbf{k}} + b^\dagger_{\mathbf{k}} a_{\mathbf{k}}$, $\sigma^y_{\mathbf{k}} = i b^\dagger_{\mathbf{k}} a_{\mathbf{k}} - i a^\dagger_{\mathbf{k}} b_{\mathbf{k}}$, $\sigma^z_{\mathbf{k}} = a^\dagger_{\mathbf{k}} a_{\mathbf{k}} - b^\dagger_{\mathbf{k}} b_{\mathbf{k}}$ and $\mathbb{I}_{\mathbf{k}} = a^\dagger_{\mathbf{k}} a_{\mathbf{k}} + b^\dagger_{\mathbf{k}} b_{\mathbf{k}}$ the Hamiltonian takes a much simpler form

$$H = -2t_2 \cos\phi \sum_{\mathbf{k}\mathbf{v}_i^2} \cos\left(\mathbf{k}\mathbf{v}_i^2\right) \mathbb{I}_{\mathbf{k}} - \sum_{\mathbf{k}\in BZ} \mathbf{B}(\mathbf{k}) \cdot \sigma_{\mathbf{k}}, \tag{3.6}$$

with $\mathbf{B}(\mathbf{k})$ an effective magnetic field in momentum space

$$\mathbf{B}(\mathbf{k}) = \left(t_1 \sum_{\mathbf{v}_i} \cos\left(\mathbf{k}\mathbf{v}_i\right), t_1 \sum_{\mathbf{v}_i} \sin\left(\mathbf{k}\mathbf{v}_i\right), \epsilon + 2t_2 \sin\phi \sum_{\mathbf{v}_i^2} \sin\left(\mathbf{k}\mathbf{v}_i^2\right) \right). \tag{3.7}$$

The ground state of this Hamiltonian at half filling is a product state of single particle operators over the BZ

$$|\Psi_0\rangle = \prod_{\mathbf{k}\in BZ} c^\dagger_{\mathbf{k}} |0\rangle, \quad c^\dagger_{\mathbf{k}} = \alpha_{\mathbf{k}} a^\dagger_{\mathbf{k}} + \beta_{\mathbf{k}} b^\dagger_{\mathbf{k}}, \tag{3.8}$$

which is completely described by the pseudospin field

$$\mathbf{S}(\mathbf{k}) := \frac{1}{2} \langle \Psi_0 | \sigma_{\mathbf{k}} | \Psi_0 \rangle \equiv \frac{\mathbf{B}(\mathbf{k})}{|\mathbf{B}(\mathbf{k})|}. \tag{3.9}$$

One crucial aspect of the Haldane model is the breaking of time reversal and inversion symmetry. Time reversal symmetry $\mathcal{T}$ reverses the arrow of time $t \to -t$ and its action on the Hamiltonian is

$$\mathcal{T} H \mathcal{T}^{-1} = -2t_2 \sum_{\mathbf{k}\mathbf{v}_i^2} \cos\phi \cos\left(\mathbf{k}\mathbf{v}_i^2\right) \mathbb{I}_{-\mathbf{k}} - \sum_{\mathbf{k}} \mathbf{B}^*(\mathbf{k}) \cdot \left(\sigma_{-\mathbf{k}}\right)^* \tag{3.10}$$

Thus, the Haldane Hamiltonian is time reversal invariant whenever

$$\mathbf{B}(-\mathbf{k}) = \Big(B_x^*(-\mathbf{k}),\, -B_y^*(-\mathbf{k}),\, B_z^*(-\mathbf{k})\Big). \tag{3.11}$$

On the other hand, inversion symmetry reflects site positions with respect to a central fixed point $x_0 + x \to x_0 - x$, where x_0 can be e.g. the central site of an hexagon. The action of this symmetry is thus to interchange the sublattice positions $a \leftrightarrow b$ and its action upon the effective magnetic field is

$$\mathbf{B}(\mathbf{k}) \to \Big(B^x(-\mathbf{k}),\, -B^y(-\mathbf{k}),\, -B^z(-\mathbf{k})\Big). \tag{3.12}$$

While B^x and B^y are invariant under both symmetries, the z component

$$B^z(k) = \epsilon + 2t_2 \sin\phi \sum_{\mathbf{v}_i^2} \sin\left(\mathbf{k}\mathbf{v}_i^2\right) \tag{3.13}$$

is not and time reversal symmetry is broken whenever the complex phase $\sin\phi \neq 0$ and inversion symmetry is broken by the sublattice imbalance term $\epsilon \neq 0$.

An important property of the graphene Hamiltonian ($t_2 = \epsilon = 0$) is that its spectrum becomes gapless at two points in the BZ, the Dirac points

$$\mathbf{K}_D^{\pm} = \frac{2\pi}{3}\left(1,\, \pm\frac{1}{\sqrt{3}}\right). \tag{3.14}$$

These two points are related by time reversal symmetry, $\mathcal{T}\,\mathbf{B}\left(\mathbf{K}_D^{+}\right)\mathcal{T}^{-1} = \mathbf{B}\left(\mathbf{K}_D^{-}\right)$, and their positions are fixed when the Hamiltonian has rotational symmetry C_3, which is not broken in the Haldane model [178, 179]. Because the spectrum becomes gapless at the Dirac points, Haldane showed [174] that his model for the integer quantum Hall effect can be described as a relativistic model in the vicinity of these points. From there, he was able to show that the Hall conductance $\sigma_{xy} = \nu e^2/h$ can be derived from the sign of the effective magnetic field z component at the Dirac points

$$\nu = \frac{1}{2}\left[\operatorname{sgn}\left(B^z(\mathbf{K}_D^{+})\right) - \operatorname{sgn}\left(B^z(\mathbf{K}_D^{-})\right)\right]. \tag{3.15}$$

This number is clearly a topological invariant as it can only take integer values $\nu = \{0, \pm 1\}$ and, to change the phase of the ground state, one must close the gap in the spectrum first, which is equal to setting one of the $B^z\left(\mathbf{K}_D^{\pm}\right)$

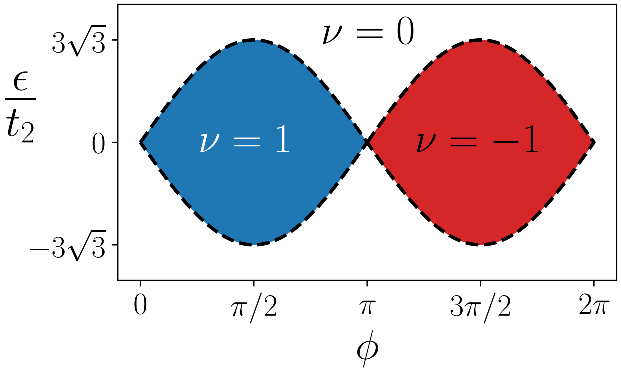

Figure 3.2: Topological phases of the Haldane model with respect to the complex phase ϕ and the rescaled sublattice imbalance ϵ/t_2. Each phase is defined by the value of the Chern number ν. The dashed lines show the points at which the spectrum becomes gapless.

to zero. The Chern number is also proportional to the total Berry flux [156] through the BZ and to the winding number of the pseudospin field [180]

$$\nu = \frac{1}{4\pi} \int_{BZ} \hat{\mathbf{S}}(\mathbf{k}) \cdot \left[\partial_{k_x} \hat{\mathbf{S}}(\mathbf{k}) \times \partial_{k_y} \hat{\mathbf{S}}(\mathbf{k}) \right] d^2\mathbf{k}, \tag{3.16}$$

with $\hat{\mathbf{S}} = \mathbf{S}/|\mathbf{S}|$ the normalized orientation of the pseudospin. The winding number maps the points in the BZ to a 3D unit sphere $\mathbf{k} \to \hat{\mathbf{S}}(\mathbf{k})$ and measures the total solid angle subtended by the normalized pseudospin, with $d\Omega \propto \hat{\mathbf{S}}(\mathbf{k}) \cdot \left[\partial_{k_x} \hat{\mathbf{S}}(\mathbf{k}) \times \partial_{k_y} \hat{\mathbf{S}}(\mathbf{k}) \right] d^2\mathbf{k}$ the differential solid angle of the pseudospin at $\mathbf{k}$.

The three possible values of the Chern number define the topological phase diagram of the Haldane model, shown in Figure 3.2. There are two CI phases with $\nu = \pm 1$ and a trivial insulating phase with $\nu = 0$. As we have seen, the boundary between phases lays at the points where one of the gaps closes

$$B_z(\mathbf{k}_D^{\pm}) = \epsilon \pm 3\sqrt{3} t_2 \sin\phi \equiv 0. \tag{3.17}$$

3.3 Topological phases in the Haldane model with interactions

The results from this section are reported in our article: *Topological phases in the Haldane model with spin-spin on-site interactions* [175].

A topological insulator is a quantum phase of matter that can be understood in the single particle picture. An interesting question is whether the notion of TI phases is still valid in the presence of interactions, which break the single particle picture, or whether the interactions can give rise to other non trivial phases. Many studies have addressed this question for general interacting TI models [181], including the Haldane model with nearest neighbour interactions [182], the Haldane-Hubbard model [183–192], the Quantum Spin Hall model [193, 194] or general TIs with fractional filling [195]. In the particular case of the Haldane-Hubbard model, while there is an agreement in the existence of a CI phase, $\nu \neq 0$, in the weak interacting regime and an antiferromagnetic trivial Mott insulator in the strong repulsive limit, there is not yet a clear consensus of whether there is an intermediate phase between these two limits with either trivial topology [192], with a non trivial topology and the same Chern number as the non interacting CI phase [184, 186, 191] or with a different Chern number [185, 188–190].

In this section we study the topological quantum phase diagram of the Haldane-Hubbard model using a mean field ansatz in momentum space and matrix product states (MPS) [92, 196]. This model consists of two spinful copies of the Haldane model with spin-spin on-site interactions. These two copies are needed as only one of them would not allow the introduction of on-site correlations in the model. Our study suggests that the CI phases of the Haldane model survive in the presence of interactions and extend until the value of the Hubbard interactions is similar to the fermions' kinetic energy. In this range of interactions our mean field ansatz is very well suited to capture the long range correlations of the model. For strong repulsive interactions the system becomes a trivial Mott insulator, $\nu = 0$, and we find traces of an intermediate phase with magnetic order and the same Chern number as in the non interacting regime.

We start with a variation of the Haldane Hamiltonian presented in Reference [197]. For a single spin population s this Hamiltonian reads

$$\begin{aligned} H_{0s} = & -t \sum_{\langle ij \rangle} \left(e^{i\phi_{ij}} a^\dagger_{is} b_{js} + \text{h.c.} \right) - \sum_{\langle\langle ij \rangle\rangle} \left(t_a a^\dagger_{is} a_{js} + t_b b^\dagger_{is} b_{js} \right) \\ & - \epsilon \sum_i \left(a^\dagger_{is} a_{is} - b^\dagger_{is} b_{is} \right) \end{aligned} \tag{3.18}$$

with t the first neighbour hopping between sublattices, $\phi_{ij} = \mathbf{p}(\mathbf{x}_i - \mathbf{x}_j)$ a complex phase between sublattices that depends on an external phase vector $\mathbf{p}$, $t_{a,b}$ the second neighbour hoppings inside the A and B sublattices and ϵ the sublattice imbalance term. Contrary to the original Haldane model, this variation breaks time reversal symmetry by introducing a complex phase in the next-nearest neighbour hoppings instead of in the nearest ones. These complex hoppings have the advantage that they can be induced in an ultracold atom experiment by means of Raman lasers [168, 197], which is an alternative way of introducing artificial gauge fields in optical lattice rather than periodically shaking the lattice. As in the original version of the model, some non-zero configurations of the vector $\mathbf{p}$ preserve time reversal symmetry and the model becomes topologically trivial [198]. Interestingly, in this variation of the Haldane Hamiltonian the second neighbour hoppings $t_{a,b}$ can be different, which has been shown to lead to novel topological semi-metallic phases not present in the original Haldane model when $|t_a| \neq |t_b|$ [198]. However, for $|t_a| = |t_b|$ both models are topologically equivalent and one can smoothly deform the Haldane Hamiltonian into this variation without breaking the topological phase. This is the parametrization we are going to use and, for the rest of this work, we set $t = 1$, $t_a = -t_b = 0.1$, $\epsilon = 0$ and the phase vector points along the vertical direction $\mathbf{p} = (0, \frac{\sqrt{3}}{2}\phi)$, with ϕ a tunable parameter.

In momentum space the Haldane Hamiltonian for one spin population s can be written as

$$H_{0s} = -\sum_{\mathbf{k} \in BZ} \mathbf{B}(\mathbf{k}) \cdot \sigma_{\mathbf{k}s}, \tag{3.19}$$

with $\sigma_{\mathbf{k}s}$ the set of Pauli matrices for each spin similar to those defined for the original Haldane model (3.6) and $\mathbf{B}(\mathbf{k})$ an effective magnetic field in momentum space

$$\mathbf{B}(\mathbf{k}) = \left(t \ \text{Re}\left\{ f(\mathbf{k}) \right\}, t \ \text{Im}\left\{ f(\mathbf{k}) \right\}, \epsilon + (t_a - t_b) g(\mathbf{k}) \right) \tag{3.20}$$

and

$$\begin{aligned} f(\mathbf{k}) &= \sum_{\mathbf{v}_i} e^{i(\mathbf{k}-\mathbf{p})\mathbf{v}_i} \\ g(\mathbf{k}) &= \sum_{\mathbf{v}_i^2} \cos\left(\mathbf{k}\mathbf{v}_i^2\right). \end{aligned} \tag{3.21}$$

Interestingly, the complex hopping phase ϕ_{ij} breaks the rotational C_3 symmetry of the model, which displaces the Dirac points along $\mathbf{p}$

$$\mathbf{K}_D^{\pm} = \left(p_x + \frac{2\pi}{3}, p_y \pm \frac{2\pi}{3\sqrt{3}}\right). \tag{3.22}$$

However, this symmetry breaking is not able to merge the Dirac cones and annihilate the CI phases [178, 179].

Without any chemical potential, the ground state of this Hamiltonian for two copies of spin-1/2 at half filling is a product state

$$|\Psi_0\rangle = \prod_{\mathbf{k}\in BZ} c^\dagger_{\mathbf{k}\uparrow} c^\dagger_{\mathbf{k}\downarrow}|0\rangle, \quad c^\dagger_{\mathbf{k}s} = \alpha_{\mathbf{k}} a^\dagger_{\mathbf{k}s} + \beta_{\mathbf{k}} b^\dagger_{\mathbf{k}s}, \tag{3.23}$$

determined by the pseudospin fields $\mathbf{S}_s(\mathbf{k})$

$$\mathbf{S}_s(\mathbf{k}) := \frac{1}{2}\langle 0|c_{\mathbf{k}s}\sigma_{\mathbf{k}s}c^\dagger_{\mathbf{k}s}|0\rangle = \frac{\mathbf{B}(\mathbf{k})}{|\mathbf{B}(\mathbf{k})|}. \tag{3.24}$$

For Hamiltonians with two or more fermionic species, such as the two spin-1/2 copies in this case, the Chern number can be decomposed as the sum of the individual Chern numbers of each type of particles [180]. The topological phases of the modified Haldane model are shown in Figure 3.3. Note that $\nu = \pm 2$ due to the two spinful copies of the model, for which each contributes with $\nu = \pm 1$.

An important question is how does adding interactions affect the topological characteristics of the model. To answer that question we study the Haldane-Hubbard model with spin-spin on-site interactions

$$H = H_{0\uparrow} + H_{0\downarrow} + U\sum_i \left(a^\dagger_{i\uparrow}a^\dagger_{i\downarrow}a_{i\downarrow}a_{i\uparrow} + b^\dagger_{i\uparrow}b^\dagger_{i\downarrow}b_{i\downarrow}b_{i\uparrow}\right). \tag{3.25}$$

In the following subsections we analyze the interacting model using both a mean field ansatz and a MPS state to characterize the quantum phases of the model.

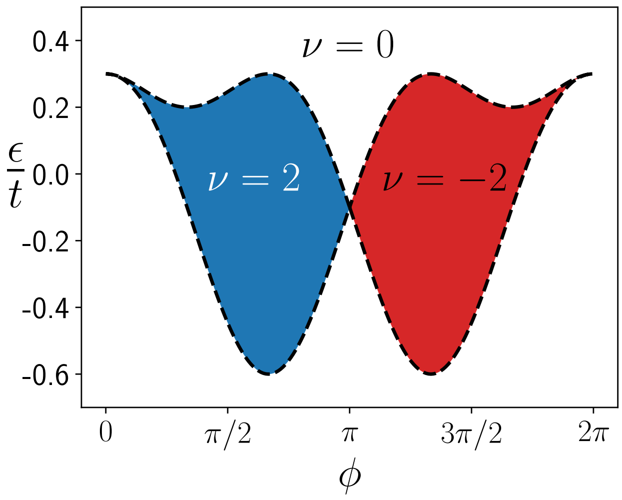

Figure 3.3: Topological phases of the modified Haldane model with respect to the complex phase ϕ, the site imbalance ϵ and first neighbour hoppings t. Each phase is labelled by the value of the Chern number ν. The dashed lines show the points at which the spectrum becomes gapless.

3.3.1 Mean field

The ground state of the Haldane model without chemical potential at half filling is completely defined by the pseudospin field $\mathbf{S}_s(\mathbf{k})$ for each spin family. Therefore, it makes sense to propose a mean field ansatz based on a variational pseudospin field

$$|\Psi_0; \mathbf{S}_\uparrow, \mathbf{S}_\downarrow\rangle = \prod_{\mathbf{k}\in BZ} c^\dagger_{\mathbf{k}\uparrow}\,[\mathbf{S}_\uparrow]\, c^\dagger_{\mathbf{k}\downarrow}\,[\mathbf{S}_\uparrow]\,|0\rangle, \tag{3.26}$$

with $c^\dagger_{\mathbf{k}s}[\mathbf{S}_s] = \alpha_{\mathbf{k}s}[\mathbf{S}_s]\, a^\dagger_{\mathbf{k}s} + \beta_{\mathbf{k}s}[\mathbf{S}_s]\, b^\dagger_{\mathbf{k}s}$ chosen such that

$$\frac{1}{2}\langle 0|(a_{\mathbf{k}s}\; b_{\mathbf{k}s})\, \sigma_{\mathbf{k}s} \begin{pmatrix} a^\dagger_{\mathbf{k}s} \\ b^\dagger_{\mathbf{k}s} \end{pmatrix} |0\rangle = \mathbf{S}_s(\mathbf{k}) \tag{3.27}$$

Thus, all information about the mean field state is contained in the two pseudospin fields. The energy functional of this ansatz state is

$$\begin{aligned} E[\mathbf{S}_\uparrow, \mathbf{S}_\downarrow] &= -\,2\sum_{\mathbf{k}s} \mathbf{B}(\mathbf{k})\cdot\mathbf{S}_s(\mathbf{k}) + 2\frac{U}{N}\sum_{\mathbf{k}\mathbf{k}'} S^z_\uparrow(\mathbf{k}) S^z_\downarrow(\mathbf{k}') + N\frac{U}{2} \\ &= -\,2\sum_{\mathbf{k}s} \mathbf{B}(\mathbf{k})\cdot\mathbf{S}_s(\mathbf{k}) + 2\,UN\langle S^z_\downarrow\rangle\langle S^z_\uparrow\rangle + N\frac{U}{2}, \end{aligned} \tag{3.28}$$

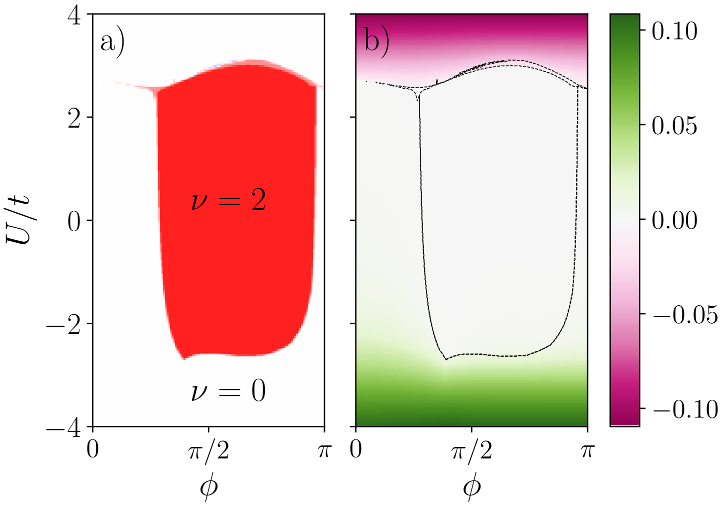

Figure 3.4: Quantum phase diagram of the Haldane-Hubbard model with respect to the complex phase ϕ and interaction U/t. The phases are characterized by the winding number (a) and double occupancy (b). The dashed lines in (b) mark the lines where the winding number changes.

with N the number of unit cells in the lattice and $\langle S_s^z \rangle = \frac{1}{N}\sum_{\mathbf{k}} S_s^z(\mathbf{k})$. In the absence of interactions $U = 0$, this functional returns the energy of two spinful copies of the Haldane model, for which the mean field ansatz is exact.

From the form of the energy functional we can determine that for weak interactions $|U| \ll |\mathbf{B}|$ the pseudospin field will be almost proportional to $\mathbf{B}(\mathbf{k})$ and thus the CI phase remains unaffected. As the interaction increases into the strong repulsive limit $U \gg |\mathbf{B}|$ the pseudospins will point in the z direction but with an antiferromagnetic ordering $\langle S_\uparrow^z \rangle = -\langle S_\downarrow^z \rangle$. This expectation value is related to the population imbalance between the A and B sublattices

$$\langle S_s^z \rangle = \frac{1}{2N}\sum_{\mathbf{k}} \langle a_{\mathbf{k}s}^\dagger a_{\mathbf{k}s} \rangle - \langle b_{\mathbf{k}s}^\dagger b_{\mathbf{k}s} \rangle = \frac{1}{2N}\sum_{i} \langle a_{is}^\dagger a_{is} \rangle - \langle b_{is}^\dagger b_{is} \rangle \tag{3.29}$$

so that in the strong repulsive limit all particles with spin up are located on one sublattice and all particles with spin down in the other sublattice. In the strong attractive regime $U \ll -|\mathbf{B}|$ the pseudospin has a ferromagnetic order $\langle S_\uparrow^z \rangle = \langle S_\downarrow^z \rangle$ and all particles sit on the same sublattice.

We show in Figure 3.4(a) the mean field topological phase diagram of the

Haldane-Hubbard model for a lattice of 20×20 unit cells. At each point the computation of the Chern number is done by discretizing the integral of the winding number (3.16) as a sum of momentum points inside the BZ. In the following we will use sometimes the notation winding number for the Chern number. The CI phase of the Haldane model, $\nu = 2$, survives in the presence of interactions and extends until the interaction is around three times the kinetic energy of the system $|U| \sim 3t$. At that transition there is also a region with winding number $\nu = 1$, which could indicate the existence of a different topological phase.

Aside from the winding number we can also characterize the quantum phases using the double occupancy, which for a half filled state is

$$D = \frac{\sum_i \langle n_{i\uparrow} n_{i\downarrow} \rangle}{\sum_{is} \langle n_{is} \rangle} - \frac{1}{4} = \langle S^z_\uparrow \rangle \langle S^z_\downarrow \rangle. \tag{3.30}$$

The double occupancy is related to the mean field energy functional (3.28) and is zero when, in average, the two particles per unit cell (one per spin) are evenly distributed over both sites. The double occupancy is shown in Figure 3.4(b). It is zero in the CI phase and non zero in the strong repulsive and attractive limits, showing an antiferromagnetic or ferromagnetic order, respectively. However, in the small region between the CI and antiferromagnetic phases, the double occupancy is non zero and the winding number is $\nu = 1$, suggesting the existence of an intermediate topological phase with magnetic ordering. On the other hand, in the topologically trivial region $\nu = 0$ at weak coupling there is a smooth crossover from negative to positive values of the double occupancy.

3.3.2 MPS ansatz

In addition to the mean field ansatz to study the Haldane-Hubbard model, we have employed a MPS ansatz [92, 196]. This method relies on the low scaling of the entanglement entropy of the ground states of 1D and 2D models and has been successfully applied to the study of many relevant condensed matter models. An advantage of this model is that it is better suited than the mean field ansatz to capture the correlations of the strong interaction regimes $|U| \gg |\mathbf{B}|$.

The MPS ansatz is a description of a general quantum many body state as a product of tensors associated to each degree of freedom of the system,

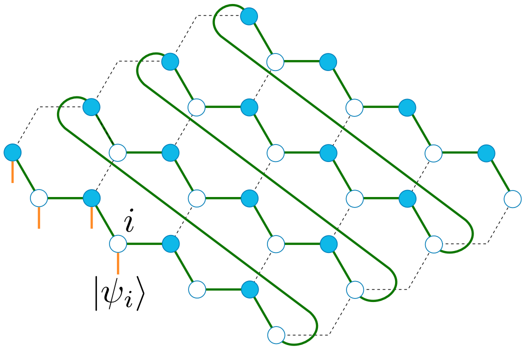

Figure 3.5: Hexagonal lattice and 1D path followed by the 'snake' MPS ansatz (green line).

in our case to each lattice site and spin

$$|\Psi\rangle = \sum_{i_1,i_2,\ldots,j_1,j_2,\ldots} A^{i_1}A^{i_2}\cdots A^{j_1}A^{j_2}\cdots|i_1\uparrow, i_2\uparrow,\cdots, j_1\downarrow, j_2\downarrow,\cdots\rangle, \quad (3.31)$$

with e.g. A^{i_2} a three dimensional tensor associated to site 2 and spin ↑. The dimension of A^{i_j} corresponding to the index i_j is called the physical dimension and runs over all degrees of freedom present at site j, while the other two dimensions depend on the amount of entanglement present in the MPS. In principle, when the latter dimensions are unbounded the MPS reproduces the exact ground state, although, in practice, this is infeasible and one usually allows a maximal dimension, called the bond dimension χ.

For the 2D lattice of the Haldane model we designed a 'snake' MPS ansatz [92] that covers every site of the two hexagonal lattices, one per spin, in a 1D path, as shown in Figure 3.5. Each lattice has $N \times N$ unit cells and the total number of sites in the MPS is $2 \times 2 \times N \times N$. For our computations we have chosen $N = 4$ and a maximal bond dimension of $\chi = 180$. Smaller lattices than 4×4 are not able to infer correctly the winding number, even in the exact non interacting regime, while bigger lattices demand more computational power than our available resources.

We show in Figure 3.6 the main results of the MPS computations. Because of the big computational cost of the MPS simulations we only study a series of points along two representative lines in parameter space, as illustrated in Figure 3.6(a). The winding number at these points is shown in Figures 3.6(b,d), where they are computed by Fourier transforming the

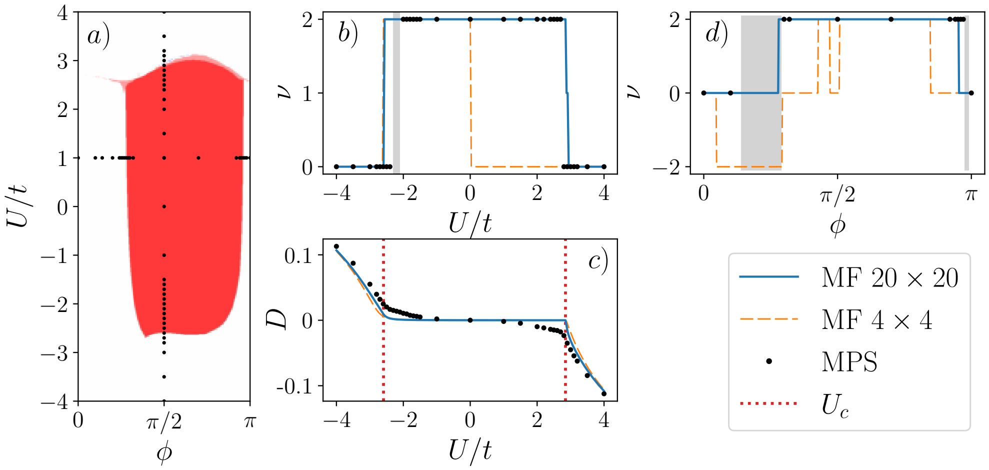

Figure 3.6: Numerical results of the MPS (dots) and mean field computations (lines). (a) On top of the mean field phase diagram, points in parameter space analysed with MPS. (b) Winding number for $\phi = \pi/2$. The grey shaded areas illustrate where the winding number of MPS did not converge. (c) Double occupancy for $\phi = \pi/2$. The critical interaction U_c (red dotted lines) marks where the mean field winding number changes. (d) Winding number in the line $U/t = 1$.

lattice correlations $\langle c_i^\dagger c_j \rangle$ into bigger lattices in momentum space with 8×8, 12×12 or 16×16 unit cells and then calculating the discretized winding number (3.16). We only keep the winding numbers that converge for the three lattice sizes in momentum space. We find, in general, a good agreement between the mean field computations for a lattice with 20×20 unit cells and the MPS ansatz. Near the phase transitions, however, the winding number has difficulties to converge, probably due to the closing of the gap. This lack of convergence is also true even for the mean state ansatz with 4×4 lattices (orange dashed lines). These regions are illustrated by a grey shaded area. Figure 3.6(c) shows the double occupancy of the MPS ground state in the line $\phi = \pi/2$. The results of the MPS computations qualitatively agree with the mean field ansatz, in special in the CI phase, where $D \sim 0$.

To analyze the magnetic ordering of the topologically trivial phases we

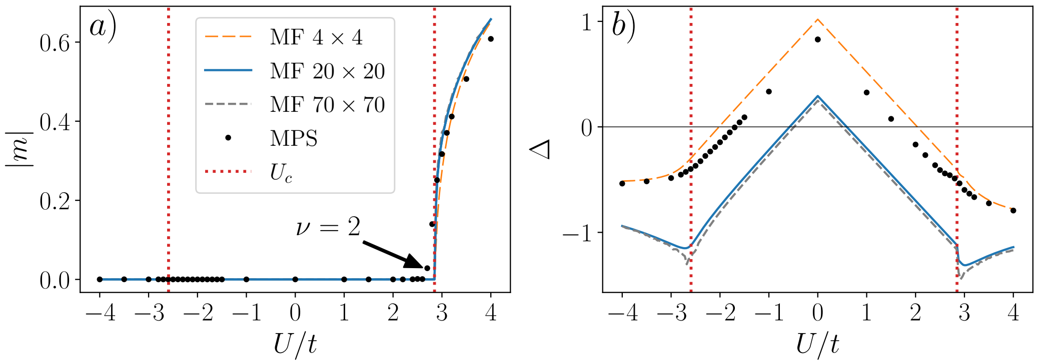

Figure 3.7: Staggered magnetization (a) and quasiparticle gap (b) with respect to the interaction U/t in the line $\phi = \pi/2$ of the MPS (dots) and mean field (lines) computations.

study the staggered magnetization

$$m = \frac{1}{N} \sum_i (-1)^i \left(n_{i\uparrow} - n_{i\downarrow}\right) = 2\left(\langle S^z_\uparrow \rangle - \langle S^z_\downarrow \rangle\right), \tag{3.32}$$

which we show in Figure 3.7(a). The magnetization is zero in the CI phase, where both pseudospin fields are aligned, and in the attractive interaction region. On the other hand, in the strong repulsive regime there is an antiferromagnetic ordering $m \neq 0$, as was shown also by the double occupancy D. The numerical MPS and mean field results are in good agreement with each other, although MPS presents a non zero staggered magnetization just before the critical interaction U_c. This can be attributed either to a finite size effect or to the emergence of an intermediate CI phase with magnetic order, as has been reported in References [184, 186, 191]. If this were a true phase of the model, it could happen that it exists when there is a non zero sublattice imbalance $\epsilon \neq 0$ and we are observing its boundary as a single point in parameter space with $\epsilon = 0$, although the evidences for this are small. Beyond that point, at U_c the results show a second order topological phase transition.

Figure 3.7(b) shows the quasiparticle gap, which measures the minimum change in energy when one adds or removes a particle to the ground state

$$\Delta = \min\left\{E\left(N_{p+1}\right) - E\left(N_p\right),\, E\left(N_{p-1}\right) - E\left(N_p\right)\right\}. \tag{3.33}$$

At half filling Δ must become zero in the strong repulsive limit, where the state becomes a trivial Mott insulator and all particles are localized in different sublattices. For the interaction regimes shown in the figure it is seen that both the MPS and mean field results qualitatively agree in the sign of Δ for a 4×4 lattice. However, the mean field computations for this gap are strongly size dependent, which we show in the figure by plotting the mean field quasiparticle gap for a lattice of 70×70 unit cells. We note that Δ is defined using systems with a different particle number and, thus, it does not correspond to the gap closing of the topological phase transition, which happens in the subspace with the same particle number.

The analysis of the convergence of the MPS results is shown in Figure 3.8(a). We performed a series of computations for different maximum bond dimensions up to $\chi = 180$ in the CI (red triangles) and trivial (blue circles) phases and fit the ground state energies to $E(\chi) = ae^{-b\chi} + c$. The interpolation suggests that calculations with $\chi = 180$ are very near to full convergence. However, while the interpolation can measure the required bond dimension for the MPS ground state to converge, it does not capture the quality of our estimation of the ground state. This is measured by the eigenstate fidelity

$$\varepsilon_F = 1 - \sqrt{\frac{\langle H^2 \rangle}{\langle H \rangle^2}}, \tag{3.34}$$

which is is zero for exact Hamiltonian eigenstates. The fidelity is shown in Figure 3.8(b) and it indicates that the best approximation to an eigenstate is reached at the non interacting point $U = 0$, while it peaks at the topological phase transitions, indicating the appearance of stronger correlations that require a larger bond dimension χ to be better captured.

Finally, we have also benchmarked the performance of the MPS ground state energy extrapolation $E_\infty := \lim_{\chi \to \infty} E(\chi)$ against the mean field energy for very large lattices of size 70×70 unit cells, which we consider to be close to the thermodynamic limit. This is computed through the relative energy difference

$$\Delta E = \frac{E_{\mathrm{MF}} - E_\infty}{|E_{\mathrm{MF}}|}, \tag{3.35}$$

which is negative whenever the mean field energy is a better description of the ground state energy than the extrapolated from the MPS simulations. This difference is shown in Figure 3.8(c) and indicates that the mean field ansatz yields a lower energy than MPS in the weak interacting region, which

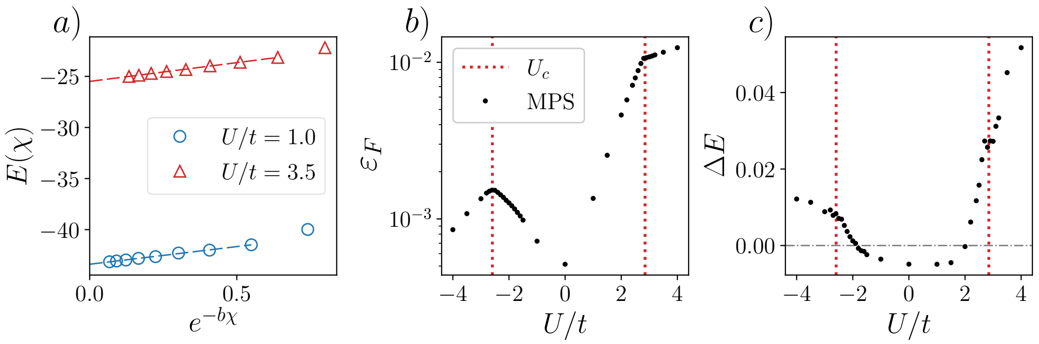

Figure 3.8: (a) Energy convergence of the MPS ground states with different maximum bond dimensions χ in a CI phase $U/t = 1$ (red triangles) and a trivial phase $U/t = 3.5$ (blue dots). The dashed lines illustrate the convergence fit of the energy. (b) Eigenstate fidelity of the MPS ground states at different values of the interaction U/t in the line $\phi = \pi/2$. U_c marks the critical energy of the topological phase transitions. (c) Relative energy difference ΔE between the mean field and extrapolated MPS ground state energies. The dash dotted line at $\Delta E = 0$ is a guide for the eye.

establishes that the mean field ansatz can capture the long range correlations of the CI phase. However, when correlations become large near the phase transitions, the MPS simulations become a better description of the ground state.

3.3.3 Discussion

We have studied the topological phase diagram of the Haldane-Hubbard model using a mean field ansatz in momentum space and MPS simulations. Our main results show that the CI phase of the Haldane model survives in the presence of interactions and extends well inside the attractive and repulsive interactions regime until the interaction strength is about three times the kinetic energy $|U| \sim 3|\mathbf{B}|$. These results are supported by the mean field and MPS simulations, which show a good qualitative agreement. In addition to computing the winding numbers, we are also able to study the magnetic ordering of the topological phase diagram using the double occupancy and staggered magnetization, which show the existence of a topological second order phase transition near the critical interaction where the winding number changes. With respect to the existence of an intermediate phase between the

CI and trivial Mott insulator phases, reported by several works, we observe both in the mean field and MPS results traces of this intermediate phase with magnetic ordering and a winding number equal to that of the CI phase. However, the signatures of this intermediate phase are not very strong and could have been originated by finite size effects. Finally, we want to remark the accuracy of the mean field ansatz in momentum space in capturing the long range correlations present in the CI phase.

3.4 Edge currents in topological insulators

The bulk-boundary correspondence is one of the most fascinating properties of topological insulators. For systems with open boundaries it states that, whenever the bulk of the system has a non trivial topological order, e.g. $\nu \neq 0$, it will always have a non zero net number of localized gapless modes along its boundaries. These boundary modes have a topological origin [147–149] and are responsible for the quantized Hall conductivity of Chern insulators $\sigma_{xy} \propto \nu$. The particle currents generated by these modes are topologically protected and have a definite direction of movement along the boundaries, making them resilient against inhomogeneities and backscattering. These characteristics of TI suggest their potential for new technological applications, such as frictionless transport of currents, amplifiers, detectors and transistors [199–203].

We can model the edge states of a Chern insulator embedded in a 2D semi infinite lattice with one edge as the continuum massless fermionic model

$$H = \nu \int_{-\infty}^{\infty} \varepsilon(p)\, a_p^\dagger a_p \, dp, \tag{3.36}$$

with ν the Chern number, $a_p^\dagger$ the creation operator of a fermionic mode localized at the boundary of the system and $\varepsilon(p)$ the energy of these modes, which obeys a linear dispersion relation $\varepsilon(p) = p$. The occupation of the edge modes in equilibrium at a temperature T and chemical potential μ is

$$n(p) = \frac{1}{1 + e^{[\varepsilon(p) - \mu]/T}}. \tag{3.37}$$

The total particle density current travelling along the edge of the system in units of $e^2/\hbar$ is equal to the number of occupied modes with different directions

$$I = \frac{\nu}{2\pi} \int_{-\infty}^{\infty} \mathrm{sgn}\,(\varepsilon)\, n(\varepsilon - \mu) d\varepsilon. \tag{3.38}$$

Note how the particles with negative momentum $p = \varepsilon < 0$ decrease the current and particles with positive momentum increase it. The current equation can also be written as

$$I = \frac{\nu}{2\pi} \int_{0}^{\infty} \left[1 - n(\varepsilon + \mu) + n(\varepsilon - \mu)\right] d\varepsilon, \tag{3.39}$$

where the first two terms are a positive current contribution created by adding *holes* $a^\dagger_{-p} \to b_{-p}$ to the negative part of the spectrum $\varepsilon < 0$. Removing the constant term, related to the total current at zero chemical potential, the edge particle density current is defined as

$$I_{\text{edge}} = \frac{\nu}{2\pi} \int_{0}^{\infty} \left[n(\varepsilon - \mu)) - n(\varepsilon + \mu)\right] d\varepsilon. \tag{3.40}$$

For a constant uniform potential along the edge $V(\mathbf{r}) = \mu$ and zero temperature this current is

$$I_{\text{edge}} = -\frac{\nu}{2\pi}\mu. \tag{3.41}$$

3.4.1 Edge modes in the Haldane model

Consider now a general non interacting fermionic Hamiltonian embedded in a discrete 2D lattice

$$H = \sum_{ij} A_{ij} c_i^\dagger c_j, \tag{3.42}$$

with $c_i^\dagger$ the fermion creation operator at a generic site of the lattice and A the Hamiltonian's matrix elements. The system is put on a cylinder with $L_x \times L_y$ unit cells and we consider the Hamiltonian to be translationally invariant along the x axis. This Hamiltonian can thus be Fourier diagonalized with the following modes

$$c_{jp}^\dagger = \frac{1}{\sqrt{L_x}} \sum_{i=1}^{L_x} e^{-ipx_i} c_{jx}^\dagger, \quad j = 1, \ldots, L_y \tag{3.43}$$

where j runs along the y direction and x_i denotes the lattice site positions along x. The Fourier Hamiltonian is now a sum of block diagonal Hamiltonians over different momenta

$$H = \sum_p H(p) = \sum_p \sum_{ij} A_{ij}(p) c^\dagger_{ip} c_{jp} \tag{3.44}$$

and the diagonalization of $A(p)$ at each momentum p

$$d^\dagger_{mp} = \sum_j U_{jm}(p) c^\dagger_{jp}, \quad A_{ij}(p) = \sum_m U_{im}(p) \varepsilon_m(p) \left(U^\dagger(p)\right)_{mj} \tag{3.45}$$

provides the eigenstates $d^\dagger_{mp}$ and eigenvalues $\varepsilon_m(p)$ of the Hamiltonian on the cylinder $H(p)$.

If the system is in thermal equilibrium, the mode correlations on the cylinder are written as

$$\langle c^\dagger_{xy} c_{rs} \rangle = \frac{1}{L_x} \sum_{mp} e^{-ip(x-r)} U^*_{ym}(p)\, U_{sm}(p)\, n(\varepsilon_m(p);\, T,\, \mu) \tag{3.46}$$

with the density following Fermi-Dirac statistics

$$n(E;\, T,\, \mu) = \frac{1}{1 + e^{(E-\mu)/T}}. \tag{3.47}$$

We now apply the above diagonalization method to study the Haldane Hamiltonian (3.4) on a cylinder

$$\begin{aligned} H = &- t_1 \sum_{\langle ij \rangle} \left(a^\dagger_i b_j + \text{h.c.} \right) - t_2 \sum_{\langle\langle ij \rangle\rangle} \left(e^{i\nu_{ij}\phi} a^\dagger_i a_j + e^{i\nu_{ij}\phi} b^\dagger_i b_j \right) \\ &- \epsilon \sum_i \left(a^\dagger_i a_i - b^\dagger_i b_i \right) + \sum_i \left(V_a(y_i) a^\dagger_i a_i + V_b(y_i) b^\dagger_i b_i \right). \end{aligned} \tag{3.48}$$

with $V_{a,b}(y)$ a non uniform local potential that preserves the translational invariance. The Fourier Hamiltonian at momentum p (3.44) reads

$$H(p) = \psi^\dagger_{jp} K_1(p) \psi_{jp} + \psi^\dagger_{jp} K_2(p) \psi_{j+1,p} + \text{h.c.}, \tag{3.49}$$

with

$$K_1(p) = \frac{1}{2} \begin{pmatrix} 4t_2 \cos(\phi + p) + V_a(j) & t_1 \left(e^{ip} + 1\right) \\ t_1 \left(e^{-ip} + 1\right) & 4t_2 \cos(\phi - p) + V_b(j) \end{pmatrix} \tag{3.50}$$

$$K_2(p) = \begin{pmatrix} t_2 \left(e^{i\phi} + e^{-i(\phi-p)}\right) & 0 \\ t_1 & t_2 \left(e^{-i\phi} + e^{i(\phi+p)}\right) \end{pmatrix} \tag{3.51}$$

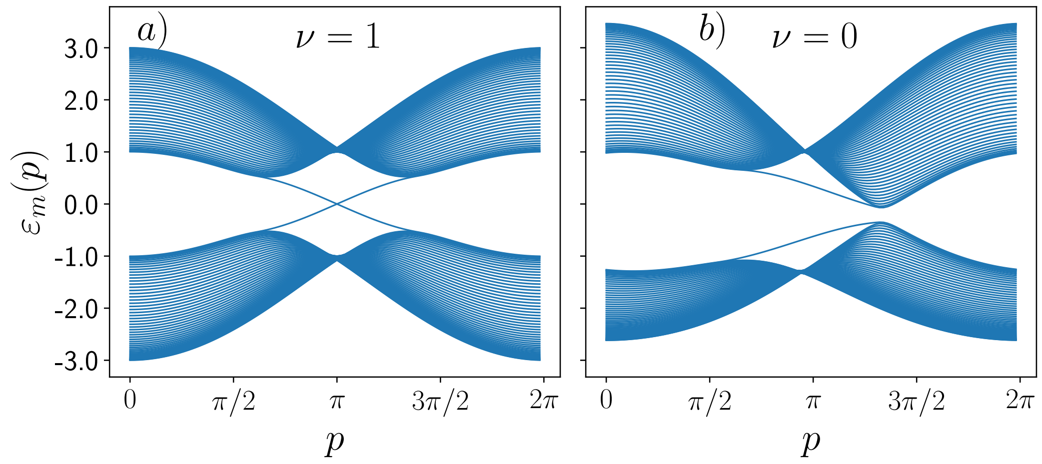

Figure 3.9: Spectrum of the Haldane model on a cylinder in a CI phase (a) and in a trivial phase (b).

and $\psi^\dagger_{jp} = \begin{pmatrix} a^\dagger_{jp} & b^\dagger_{jp} \end{pmatrix}$ a spinor over both sites of the unit cell.

Figure 3.9 shows the spectrum of the Haldane Hamiltonian on a cylinder of $L_x \times L_y = 100 \times 50$ unit cells in a CI phase (a) with $\phi = \pi/2$, $\varepsilon = 0$ and in a trivial phase (b) with $\phi = \pi/4$, $\varepsilon = 0.5$. The other Hamiltonian parameters are $t_1 = 1$, $t_2 = 0.1$, $\epsilon = 0$, which are fixed for the rest of this work. In the CI phase the spectrum has two bands that cross from the valence to the conductance bands with an approximately linear dispersion relation $\varepsilon_m(p) \sim p$ around $p = \pi$. These modes are located one at each boundary and, as we will see later, they both conduct a current along their corresponding edges with opposite group velocity. On the contrary, in the trivial insulator phase these modes are absent and there is an energy gap separating the two bands.

3.4.2 Particle density currents

The two-point particle density current J_{ij} flowing from site j to i is derived through the Heisenberg equation for the number of particles in one lattice site

$$\frac{dn_i}{dt} = -i\,[H,\, n_i] = \sum_j J_{ij}. \tag{3.52}$$

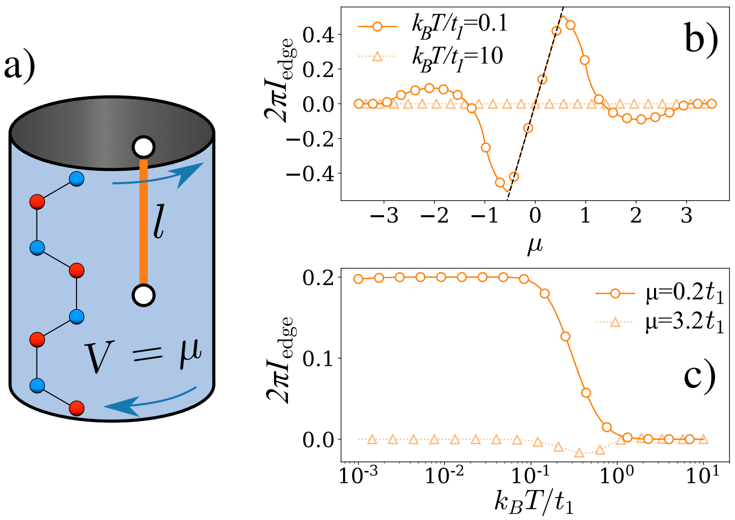

Figure 3.10: (a) Sketch of the Haldane Hamiltonian on a cylinder and the boundary l used to define the edge currents. (b) Variation of the edge current with respect to the constant chemical potential for different temperatures, one smaller than the energy gap $k_b T = 0.1 t_1$ and one larger $k_b T = 10 t_1$. (c) Edge currents with respect to the temperature at two different chemical potentials, one inside the energy gap $\mu = 0.2 t_1$ and one well inside the conductance band $\mu = 3.2 t_1$.

with $\sum_j J_{ij}$ the total incoming particle density flux into the lattice site i. For a general one body Hamiltonian (3.42), this current is

$$\sum_j J_{ij} = -i \sum_{mn} A_{mn} \left[c_i^\dagger c_i, c_m^\dagger c_n \right] = -i \sum_{mn} A_{mn} \left(\delta_{im} c_i^\dagger c_m - \delta_{in} c_m^\dagger c_i \right), \tag{3.53}$$

from which the form of the two-point density current operator is

$$J_{ij} = -i \left(A_{ij} c_i^\dagger c_j - A_{ji} c_j^\dagger c_i \right). \tag{3.54}$$

and the average current between two points is

$$\langle J_{ij} \rangle = 2 \, \mathrm{Im} \left\{ A_{ij} \langle c_i^\dagger c_j \rangle \right\}. \tag{3.55}$$

To observe the edge currents produced by the edge modes of the Haldane model it is useful to define a boundary l crossing one edge of the cylinder, as illustrated by the orange line in Figure 3.10(a). One then defines the average particle density current at the edge as the sum of all two-point currents J_{ij} that cross the boundary along the same direction (from 'left' of l to 'right' in this case)

$$2\pi I_{\text{edge}} = \sum_{ij\text{: cross } l} J_{ij}. \tag{3.56}$$

For the ground state of the Haldane Hamiltonian in a CI phase on a cylinder (3.49) with a constant chemical potential $V_{a,b} = \mu$, Figure 3.10(b) shows the evolution of the edge particle current I_{edge} with respect to the chemical potential μ. These results are computed for a cylinder with 300×30 unit cells at temperatures $k_B T/t_1 = 0.1,\ 10$. As was shown by the continuum edge model (3.36), the edge currents at low temperatures are proportional to the chemical potential μ at the edge whenever it lays inside the energy gap. This behaviour is illustrated by the dashed line around $\mu = 0$. However, larger chemical potentials or temperatures open holes and create particles in the valence and conductance bands, causing the edge currents to vanish. The effect of high temperatures is shown in Figure 3.10(c) for two constant chemical potentials $\mu = 0.2t_1,\ 3.2t_1$. In there, when the chemical potential is inside the energy gap, $\mu = 0.2t_1$, the edge currents persist until the temperature is of the order of the gap $k_B T/t_1 \sim 1$. On the other hand, for the chemical potential outside the energy gap, $\mu = 3.2t_1$, the edge current is always zero.

3.5 Bulk currents in Chern insulators

The results from this section are reported in our article: *Topological bulk states and their currents* [176].

The definition of topological insulators frequently includes that they are band insulating materials in their bulk, while, at the same time, conduct currents along its boundaries. These edge currents, as we have seen in the previous section, are gapless, localized and protected against small inhomogeneities. However, our analysis only took into account Hamiltonians with a constant chemical potential. We will see in this section that having inhomogeneous potentials in Chern insulators can lead to topologically protected localized states and currents *in the bulk* of the topological insulator.

3.5.1 Emergence of localized bulk states and currents in the SSH chain

As we have seen, the Haldane Hamiltonian embedded on a cylinder can be Fourier transformed into a sum of Hamiltonians for each momentum p (3.49). A simple example of a system that has localized bulk states and gives rise to localized bulk currents is found in the mode $p = \pi$

$$\begin{aligned} H(\pi) = t_1 \sum_{j=1}^{L_y} \left(b_j^\dagger a_{j+1} + \text{h.c.} \right) + 2\, t_2 \sum_j \left(i\, a_j^\dagger a_{j+1} - i\, b_j^\dagger b_{j+1} + \text{h.c.} \right) \\ + \sum_j \left[V_a(j)\, a_j^\dagger a_j + V_b(j)\, b_j^\dagger b_j \right], \end{aligned} \tag{3.57}$$

where j runs along the y axis of a large 1D unit cell. This Fourier mode is described by a dimerized version of the Su-Schrieffer-Heeger (SSH) 1D chain with additional complex second neighbour hoppings t_2 and an inhomogeneous local potential $V_{a,b}(j)$. This potential is taken to be a step at the middle of the cylinder

$$V_a(j) = V_b(j) = \begin{cases} -w, & j \leq L_y/2 \\ +w, & j > L_y/2 \end{cases}. \tag{3.58}$$

Localized bulk modes for $p = \pi$

We begin by studying the simpler case of the SSH chain without second neighbour couplings $t_2 = 0$. In this limit the lattice splits into independent pairs of sites (b_{i-1}, a_{j+1}), called dimers, coupled by the first neighbour hopping t_1, as illustrated by the dashed circle in Figure 3.11(a). However, the two boundary sites of the chain are left decoupled from the rest of the system. This produces two localized edge modes that have zero energy in the absence of any potential. The populations at the boundary sites at half filling are related by $n_1 + n_{L_y} = 1$.

The dimer modes in the bulk of the chain are degenerate and the population density is evenly distributed between the two dimer sites, as seen in Figure 3.11(b) for a lattice with $L_y = 6$ unit cells at half filling and for different potential steps $w = 0.2$, 0.4, 0.8 with zero temperature. This degeneracy can lead to the bulk modes being delocalized over one of the potential steps $1 < j < L_y/2$ or $L_y/2 < j < L_y$. However, the dimer located at the

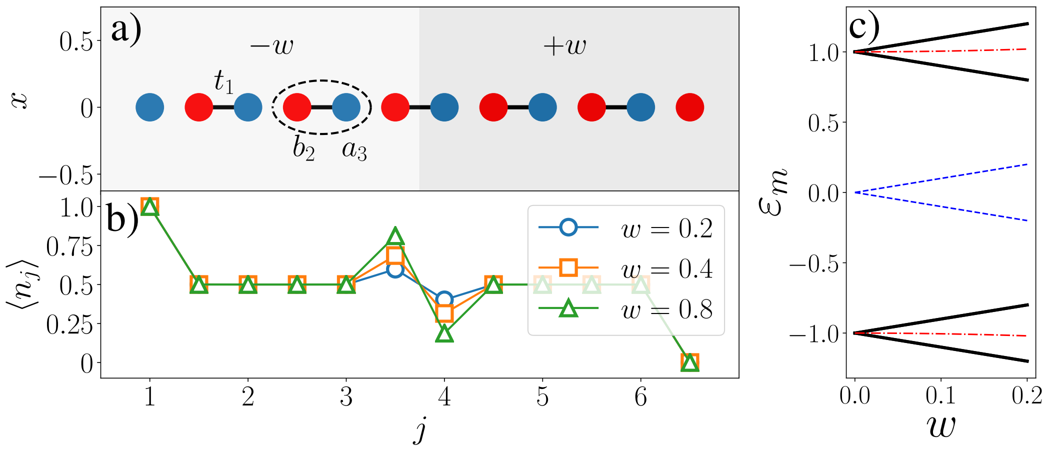

Figure 3.11: (a) Sketch of the fully dimerized SSH chain inside a step potential. (b) Population density at each site of the chain for different potential steps w. (c) Dimer energies with respect to w. The thick solid lines represent the degenerate energies of the bulk modes, the blue dashed the edge modes and the red dash-dotted are the step modes.

potential step $y = L_y/2$, which we refer to as the *step mode*, has a different local potential energy at each site, making it to have a different energy than the rest of the bulk modes. This prevents it from delocalizing over the chain and localizes this mode at the step of the potential. This decoupling of the step mode energies with $w \neq 0$ is shown in Figure 3.11(c) for the 1D SSH chain with $L_y = 6$ unit cells and $t_1 = 1, t_2 = 0$. The bulk dimer energies (thick solid lines) split into four degenerate groups as w increases, while the the step dimer energies (red dash-dotted lines) are different than that of the bulk modes for $w > 0$.

Bulk currents on the cylinder from the $p = \pi$ mode

The introduction of small complex second neighbour hoppings $t_2 \ll t_1$ in the SSH chain causes the emergence of localized bulk currents on the cylinder stemming from the localized step modes. We can prove it with first order perturbation theory in the next-nearest neighbour hoppings $t_2 \ll t_1$ and in the step of the potential $w \ll t_1$. The full mathematical derivation is done in Appendix. A.3. We find that each dimer mode gives rise to two counter propagating currents localized at each dimer site. The magnitude of these currents for each dimer depends on the balances of population and energies of this dimer and its nearest neighbouring dimers. In the bulk of the system, where all dimers have equal characteristics, these currents have equal magnitude and the current of one dimer is canceled by the current of its neighbouring one. However, the potential gradient induces a change in the population balance of the step dimer and its energy. Therefore, the magnitude of the currents of the step dimer is different from the currents of its neighbouring bulk dimer modes, generating a localized net current around the step. A similar behaviour is observed at the boundary modes.

As detailed in Appendix A.3, to first order in t_2/t_1 and w/t_1, the net currents localized in the bulk and on the edge of the cylinder for the mode $p = \pi$ are

$$\begin{aligned} I_{\text{edge}} &= 2\, t_2 \\ I_{\text{bulk}} &= -\, 4\frac{w\, t_2}{t_1}. \end{aligned} \tag{3.59}$$

While these currents are derived for the 1D SSH chain, it can be shown that they also give rise to currents between adjacent 1D unit cells on the cylinder. Figure 3.12(a) shows a sketch of this 1D lattice on the cylinder, together with the direction of the purely imaginary second neighbour hoppings $i\, t_2$ (black arrows) and the first neighbour hoppings t_1 (solid lines). The bulk and edge currents originated from the $p = \pi$ mode are shown in Figure 3.12(b) for a cylinder with $L_x \times L_y = 100 \times 6$ unit cells inside a step potential of height $w = 0.1$ at zero temperature. There are two bulk currents, one on each side of the potential step. Together, they form a net bulk current localized around the potential step, flowing along the opposite direction as the edge currents. Note that the homogeneous potential case with only localized edge currents is recovered for $w = 0$, which is often the analysed situation in topological insulator theory.

Dispersion relation

The analysis of the SSH chain with complex second neighbour hoppings (3.57) partially explains the emergence of localized bulk states in the system and the localized currents in the bulk that they produce. However, as seen in the continuum edge model (3.36), a non zero dispersion relation $dE(p)/dp$ is needed in order for the 2D model to have a net edge current. We study the dispersion relation of the Haldane model by analysing modes near $p = \pi$ with

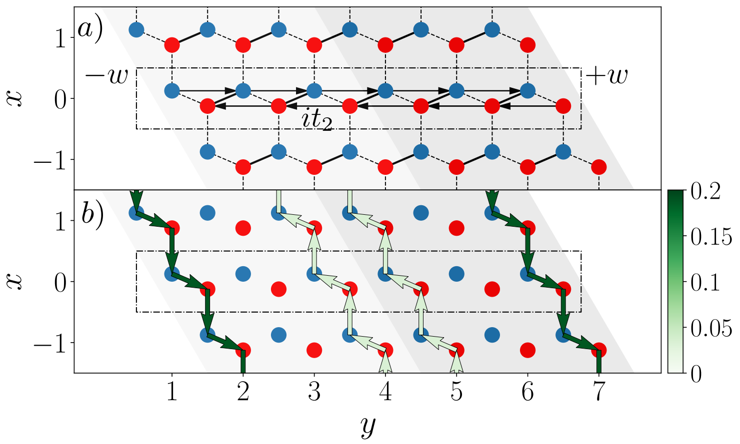

Figure 3.12: (a) Sketch of the 1D SSH chain on the cylinder (inside the dashed rectangle). Arrows indicate the direction where the complex second neighbour hoppings are $+it_2$ and solid lines indicate the first neighbour hoppings t_1. (b) Localized bulk and edge currents on the cylinder.

perturbation theory [See Appendix. A.3]. Introducing a small momentum offset $p = \pi + \delta p$ that adds a perturbation potential V_p to the complex SSH chain, the dispersion relation of a particular mode $|\psi_j\rangle$ is

$$\frac{dE_j}{dp}(p=\pi) = \frac{\langle \psi_j | V_p | \psi_i \rangle}{\delta p} + \mathcal{O}\left(\delta p^2\right). \tag{3.60}$$

For small couplings and potential steps $w, t_2 \ll t_1$, the dispersion relations around $p = \pi$ of the Haldane bulk and edge modes are

$$\begin{aligned} \frac{dE_{\text{edge}}}{dp}(\pi) &= \pm\, 6t_2 \\ \frac{dE_{\text{step}}}{dp}(\pi) &= \pm\, 6\frac{w\, t_2}{t_1}, \end{aligned} \tag{3.61}$$

where the sign of the edge mode depends on which boundary it is located and the sign of the bulk mode depends on whether the mode is in the valence or conductance band. The dispersion relation of the step modes again indicates that a completely homogeneous potential $w = 0$ annihilates any localized bulk current.

Thus, as we have seen, the perturbation theory analysis of the Haldane Hamiltonian modes with $p = \pi$ can explain the emergence of localized states in the bulk where the potential changes, the emergence of localized currents in the bulk and the non zero dispersion relation of the bulk modes, which indicates that these have a similar band pattern as the edge modes that give rise to edge currents.

3.5.2 Localized bulk currents in the Haldane model from all modes

Guided by the above results it is then interesting to ask whether localized bulk states and localized bulk currents can emerge in the full Haldane model on a cylinder. In this section we analyze this model inside different inhomogeneous potentials and study the associated states and currents. Our results strongly support that the changes in the local potential give rise to localized states in the bulk of the cylinder and that these states, in turn, give rise to localized bulk currents. Moreover, these currents are topologically protected against temperature and local disorder in the same form as edge currents.

We begin our study by analysing different inhomogeneous potentials on the cylinder. The bandwidth of such potentials is always smaller than the energy gap, so that they are not able to induce any topological phase transition. Additionally, we set the potential at the boundaries of the cylinder to zero $V(1) = V(L_y) = 0$, which, according to Equation (3.41), removes the edge currents and the focus remains only on bulk currents.

The first example is a double step potential of the form

$$V(y) = \begin{cases} +w, & L_y/4 < y < 3L_y/4 \\ 0, & \text{otherwise.} \end{cases} \tag{3.62}$$

The shape of this potential is similar to the one previously studied in the SSH chain, but it has two steps instead of one. It is sketched as white dots in Figure 3.13(a). We compute every particle density current $I(y)$ going from 'left' to 'right' at different heights y for a cylinder with $L_x \times L_y = 1000 \times 30$ unit cells with x the periodic axis and at thermal equilibrium with $T = 0$ and no chemical potential. These currents are shown as blue bars in Figure 3.13(a) and are zero for all y except at the points were the potential changes, where they are highly localized. Moreover, the total current in the top of the cylinder (orange diamond) is of the same magnitude as the current in the bottom of the cylinder (green circle) but has opposite direction, so the net current on the cylinder is zero.

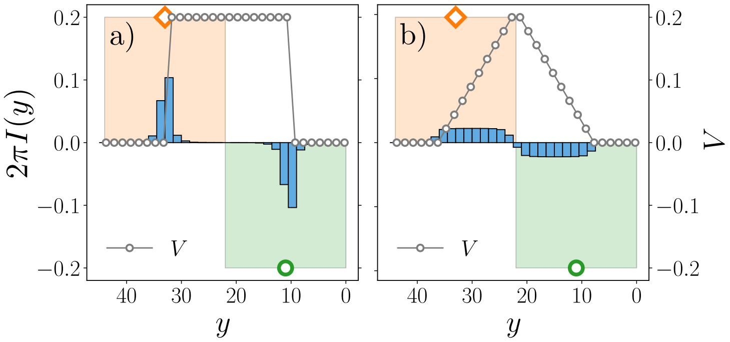

Figure 3.13: Profiles of local two-point currents $2\pi I(y)$ (blue bars) with respect to their height on the cylinder y. The systems are inside a two step potential (a) and a triangular potential (b) (white dots). The orange diamonds represent the net current on the top of the cylinder $y > L_y/2$ and the green dots the net current on the bottom $y < L_y/2$.

Motivated by the above results we postulate a different potential in the form of a triangle, sketched in Figure 3.13(b). The gradient of this potential is continuous inside the triangle and zero near the boundaries of the cylinder. The current profile of this cylinder is shown as blue bars in the Figure. These currents are proportional to the gradient of the potential and the net top (orange diamond) and bottom (green circle) currents have equal magnitude and different direction, yielding a total zero current along the cylinder.

Guided by the results from the two potentials above we propose the following expression for the bulk currents

$$I_{\mathrm{bulk}}(\mathbf{r}) = \frac{\nu}{2\pi} a |\nabla V(\mathbf{r})| \tag{3.63}$$

with a the length constant of the lattice and $\nabla V(\mathbf{r})$ the local potential gradient. These currents run perpendicular to the potential gradient and their direction is given by the sign of the gradient. This expression qualitatively explains the emergence of currents localized at the regions where the potential gradient is non zero.

We confirm in Figure 3.14 that the above expression for the currents is correct by measuring the net density currents on the top (T) and bottom (B) halves of a cylinder with $L_x \times L_y = 1000 \times 30$ unit cells when the system is either in a topological or in a trivial phase and against temperature and local random disorder. The system is subject to a two step potential (3.62) whose

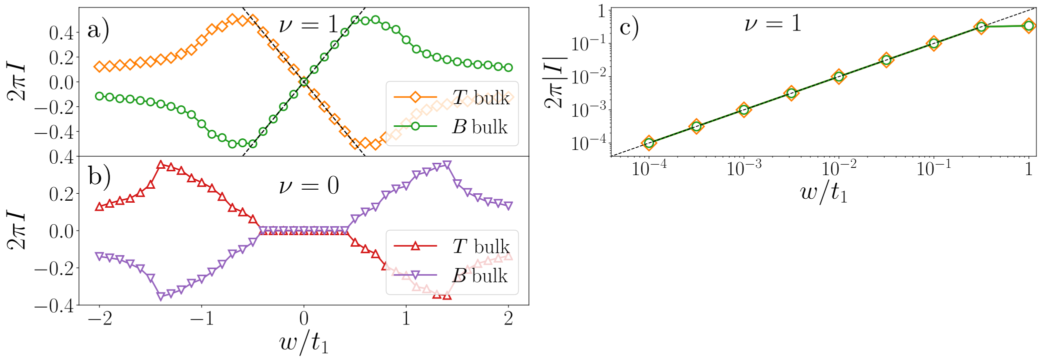

Figure 3.14: (a-c) Behaviour of the net top (T) and bottom (B) bulk currents $2\pi I$ with respect to the height w of a two step potential in a topological (a) and a trivial (b) phase. (c) Magnitude of the currents in a topological phase for very small potentials w. The dashed lines in (a,c) illustrate the linear behaviour of the currents inside the energy gap.

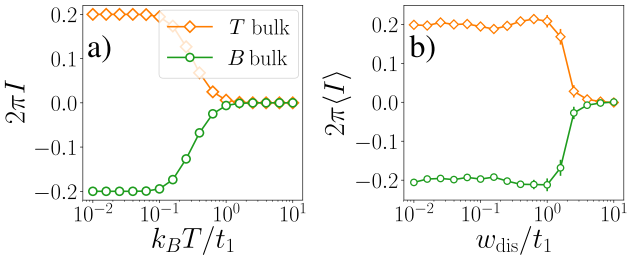

Figure 3.15: Resilience of the net top (T) and bottom (B) bulk currents with respect to the temperature (a) and local random disorder (b).

height w we can control and is proportional to the local potential gradient $|\nabla V(\mathbf{r})| \propto w\,\delta_{\mathbf{r},\mathbf{r}_{\text{step}}}$ at the two steps of the potential. Figs 3.14(a,b) show the behaviour of the top and bottom currents in a topological phase with $\phi = \pi/2$, $\epsilon = 0$ (a) and in a topologically trivial phase with $\phi = \pi/2$, $\epsilon = 0.2t_1$ (b) against the height of the potential step w. When w is below the energy gap, the bulk currents are proportional to it and to the Chern number of the system, indicating that they have a topological origin. Figure 3.14(c) shows the currents in the same topological phase as (a) against very small potential steps w, where it is seen that the currents are proportional to w and, thus, to the local gradient of the potential $|\nabla V(\mathbf{r})|$.

Because the density currents depend on the topology of the system, they must be resilient against thermal excitations and local random disorder. First, Figure 3.15(a) shows the temperature dependency of the density currents, which is similar to the one we found for edge currents [See Figure 3.10(c)]. Second, Figure 3.15(e) shows the average density currents when a local random potential $V(\mathbf{r}) = \delta(\mathbf{r})$ is introduced, with values drawn from a uniform distribution in $[-w_{\text{dis}}, w_{\text{dis}}]$. To respect the translational symmetry of the cylinder, the local disorder only depends on the height on the cylinder $\delta(\mathbf{r}) = \delta(y)$. In both cases, if the temperature is of the order of the energy gap $k_B T/t_1 \sim 1$ or if the disorder strength is similar to the gap $w_{\text{dis}}/t_1 \sim 1$, the system develops particle and hole excitations in the valence and conductance bands that annihilate the density currents. However, both figures also show that the bulk currents are resilient against small thermal excitations and local disorder.

3.5.3 Localized bulk states in the Haldane model

Edge states in conventional Chern insulators arise from modes that are exponentially localized at the boundaries. It is then natural to ask whether bulk currents arise from localized states in the bulk. This can be studied by measuring the degree of locality of the eigenstates in the valence and conductance bands. A possible characterization of this localization can be done with the Inverse Participation Ratio (IPR), which quantifies the localization of every eigenstate ψ_{mp}

$$\text{IPR}_{mp} = \sum_y |\psi_{mp}(y)|^4. \tag{3.64}$$

An IPR near to one reveals a highly localized state, while a low IPR is an indication of high delocalization. More information about the localization of the bulk modes can be drawn from the asymmetrical IPR

$$F_{mp} = \sum_y |\psi_{mp}(y)|^4 \operatorname{sgn}\left(y - \frac{L_y}{2}\right), \tag{3.65}$$

which is positive for states that are mostly localized at the bottom half of the system $y < L_y/2$, negative if they are localized at the top half and zero if they are evenly delocalized.

We computed both observables for the Haldane model on a cylinder with $L_x \times L_y = 100 \times 150$ unit cells subject to a two step potential (3.62) of height

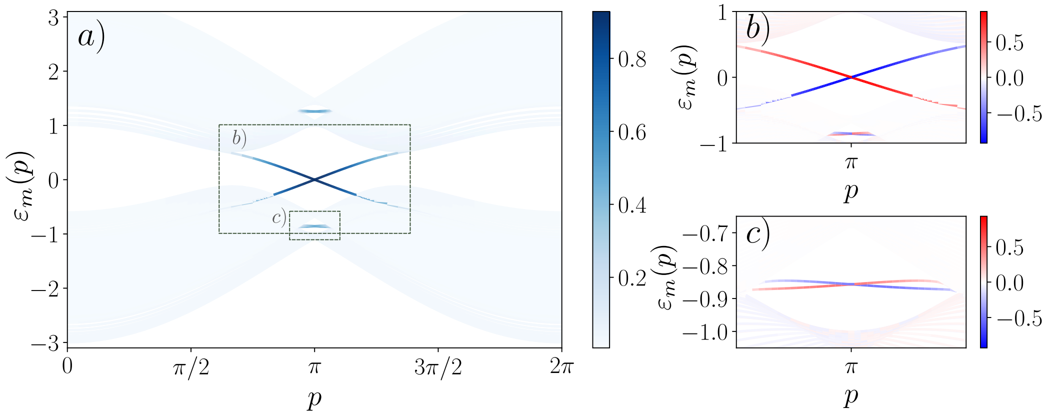

Figure 3.16: (a) IPR of the Haldane model inside a two step potential on a cylinder. The dashed lines mark the regions where we measure the asymmetrical IPR. (b, c) Zoom of the asymmetrical IPR of the edge (b) and bulk (c) modes.

$w = 0.4$. This potential is smaller than the energy gap and cannot induce a topological phase transition on the cylinder. From the IPR results, shown in Figure 3.16(a), we conclude that there are two distinct sets of localized states in this model. The first set is composed of two localized bands crossing from the valence to the conductance bands that correspond to the localized edge states at the boundaries of the cylinder. As expected, the asymmetrical IPR, Figure 3.16(b), indicates that each of these bands corresponds to one boundary.

The second set of localized states is, however, not found in Chern insulators with homogeneous potentials. When the potential step is present, $w \neq 0$, two small gaps of size proportional to w open inside the valence and conductance bands around momentum $p = \pi$, as shown in Figure 3.16(a). Inside each gap there are two localized bands that correspond to localized states at the step of the potential in the bulk of the cylinder. Furthermore, the asymmetrical IPR, Figure 3.16(c), shows that each band is localized in a different half of the cylinder. These states, as the edge states, have a non zero dispersion relation dE/dp, which will give rise to currents in the system. However, contrary to the edge states, the localized bulk modes are well inside the valence and conductance bands, meaning that these modes are, in general, either always occupied or unoccupied.

3.5.4 Topological bulk and edge currents in harmonic potentials

The results from this section are reported in our article: *Seeing topological edge and bulk currents in time-of-flight images* [177].

Translational invariant systems on cylinders such as the ones studied in the previous section are not found in any real material. To find any model that hosts localized bulk and edge currents, while at the same time is able to be experimentally recreated, we must look into ultracold atom experiments. These experiments [166] trap a neutral atom cloud into a laser field that is composed of two parts: one that creates an effective Hamiltonian for the atoms, such as the Haldane model [170], and an harmonic potential that traps the atoms inside the optical lattice. Interestingly, this harmonic trap has a non zero potential gradient that can cause localized bulk and edge currents to appear when the effective Hamiltonian has a non trivial topology. Motivated by this possibility we study in this section the currents that appear when the Haldane model is placed inside an harmonic potential. We conclude that the harmonic potential divides the system into three separate regions with different topological quantum phases: a CI and two topologically trivial phases. Moreover, the slowly changing potential of the harmonic trap creates edge currents at the boundaries of the CI phase and a counter propagating bulk current inside it.

The Haldane Hamiltonian (3.4) inside a local harmonic trapping potential is

$$H = t_1 \sum_{\langle ij \rangle} c_i^\dagger c_j + t_2 \sum_{\langle\langle ij \rangle\rangle} e^{i\nu_{ij}\phi}\, c_i^\dagger c_j + \sum_i V(\mathbf{r}_i)\, c_i^\dagger c_i, \tag{3.66}$$

with

$$V(\mathbf{r}_i) = V_0 + k \left(\frac{|\mathbf{r}_i|}{r_{\max}} \right)^2, \tag{3.67}$$

where V_0 is a constant chemical potential, k a positive constant that defines the width of the trap and the strength of the potential gradient and $r_{\max}$ is the maximum distance between any lattice site and the trap center. When the harmonic trap is wide enough that the potential gradient is very small in comparison with the energy scale of the Haldane Hamiltonian, the local density approximation (LDA) states that the physics in the neighbourhood of a point $\mathbf{r}$ is determined by the local value of the harmonic potential $V(\mathbf{r})$ at that site. Therefore, the potential can split the lattice into separate regions

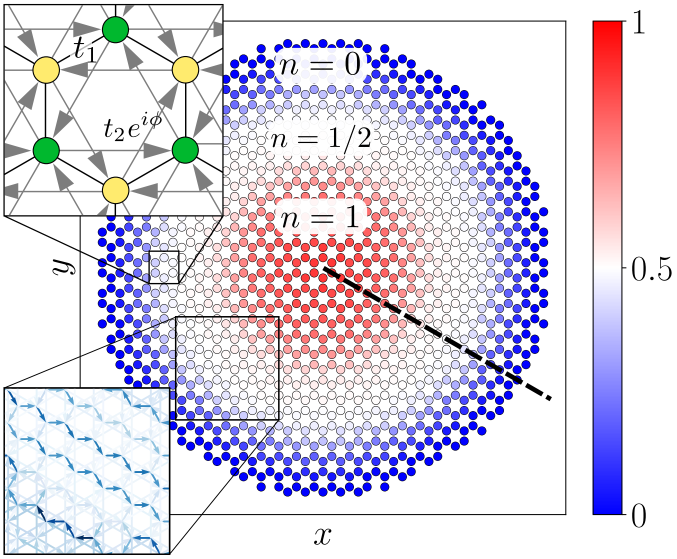

Figure 3.17: Site occupations of the Haldane model inside an harmonic potential. The lattice is divided into three regions with densities $n = 0$ (blue), $n = 1/2$ (white), $n = 1$ (red). We measure the density currents travelling through the dashed line. (Upper inset) Sketch of the Haldane Hamiltonian hoppings. (Lower inset) Two-point currents J_{ij} between neighbouring sites of the lattice.

with different local properties. In particular, when $V(\mathbf{r})$ is inside the energy gap of the Haldane Hamiltonian, the LDA states that this region is in a CI phase $\nu = \pm 1$.

We have analysed the ground state of the Haldane model in a large lattice with 1200 sites inside an harmonic trap with parameters $V_0 = -2.1$, $k = 5.6$, $r_{\text{max}} = 13\sqrt{3}$. The trap parameters are chosen such that its spectral bandwidth is similar to that of the Haldane model, while simultaneously the trap is wide enough for the LDA to hold. The site occupations of the ground state $\langle n_i \rangle$, shown in Figure 3.9, separate the sample into three separate regions [197]: an inner layer that is almost fully occupied, with local density $n = 1$, an external layer that is almost depleted, $n = 0$, and an intermediate layer between these two regions at approximate half filling, $n = 1/2$. The boundaries of these regions are located at the points where the harmonic potential $V(\mathbf{r})$ is equal to the beginning or the end of the band gap. Due to the LDA, the intermediate phase at half filling is a CI with local Chern number

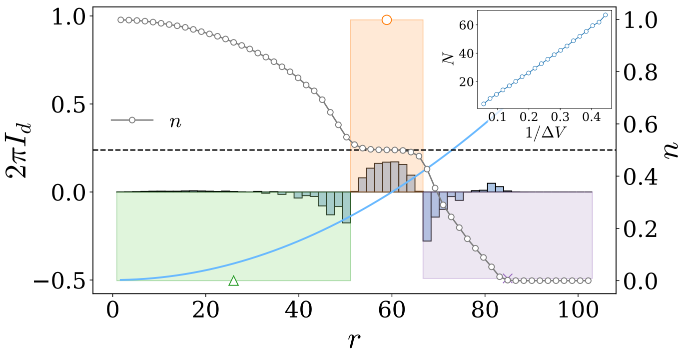

Figure 3.18: Local current profile (bars) of the Haldane model inside an harmonic trap. The net inner edge (green triangle), outer edge (purple cross) and bulk (orange circle) currents are shown as wide bars. The local site occupation $\langle n_i \rangle$ is illustrated by the white dots. (Inset) Width of the CI phase with respect to the potential difference ΔV between its two boundaries.

$\nu = 1$, while the inner and outer regions are topologically trivial $\nu = 0$.

The CI phase inside the harmonic trap is in contact with two trivial phases and, therefore, edge currents should naturally emerge at the boundaries of the CI. In addition, due to the non zero potential gradient of the harmonic trap, localized bulk currents should also emerge in this phase. We test this hypothesis by measuring the particle density currents J_{ij} travelling across a radial line in the lattice as illustrated by the dashed line in Figure 3.17. The lattice has 28000 sites and the harmonic potential parameters are $V_0 = -3$, $k = 9$, $r_{\max} = 60\sqrt{3}$. The current profile of the harmonic potential is shown as an histogram in Figure 3.18, where $2\pi I_d(r)$ measures the density current at a distance r from the center of the trap. The shape of the currents clearly displays two sets of edge currents at the boundaries of the CI, $n = 1/2$, and an extended bulk current inside that phase. The net bulk current is proportional to the potential difference between the two boundaries of the CI

$$\sum_{i:\,\langle n_i \rangle = 1/2} a|\nabla V(\mathbf{r}_i)| \sim |V(\mathbf{r}_{\text{outer}}) - V(\mathbf{r}_{\text{inner}})|, \tag{3.68}$$

which further confirms the previous law for the bulk currents (3.63). On the other hand, the combined net edge currents have the same magnitude but opposite direction as the bulk currents, leading to a zero net current along the harmonic trap.

We have also quantified the width of the CI phase, defined as the number of lattice sites N between the boundaries with the trivial phases. This width is shown in the Inset of Figure 3.18. It grows linearly with the inverse potential difference between the two phase boundaries $N \propto 1/\Delta V \propto 1/k$, so that macroscopic observables of the currents could, in principle, be observed in an ultracold atom experiment by tuning the potential trap strength k.

3.6 Observation of topological phases and currents in ultracold atom experiments

Ultracold atom experiments are an excellent platform to study the topological properties of topological insulators, as they offer a rich degree of controllability that can simulate many physically interesting materials with different kinds of geometries and hoppings. Moreover, new techniques, such as periodically shaking the lattice [204, 205] or laser assisted hopping [168, 171, 206], have lead to the implementation of artificial gauge fields in ultracold atoms. These advances have culminated in the full implementation of the Haldane model in an optical lattice and the measurement of its topological properties [170]. In this section we will explore how to implement the Haldane-Hubbard model studied in Section 3.3 and how to measure the topological bulk and edge currents that appear in the optical lattice implementation of the Haldane model inside an harmonic trap.

3.6.1 Topological phases in the Haldane model with on-site interactions

The results from this section are reported in our article: *Topological phases in the Haldane model with spin-spin on-site interactions* [175].

In Section 3.3 we studied the Haldane-Hubbard model with a mean field ansatz and MPS simulations. We concluded that the CI phase of the Haldane model is extended in the presence of interactions until they become of order of the electron's kinetic energy $|U| \sim |\mathbf{B}|$. We also analysed other observables, such as the double occupancy or the staggered magnetization, that classify the topological phase diagram of the model and found traces of a possible intermediate phase between the CI and trivial Mott insulator phases.

Interestingly, the Haldane-Hubbard Hamiltonian can be realized in ultracold atom experiments using state-of-the-art techniques. In Reference [170], where the Haldane model is implemented in an optical lattice, the authors report that the ultracold atom cloud consists of a population of neutral atoms of one species and that the two hyperfine levels of this species with lowest energy are trapped inside the optical lattice. These two hyperfine level populations spontaneously interact between them when they are on the same lattice site, much like a Hubbard interaction, and the authors, therefore, have to suppress this interaction using Feshbach resonances to arrive at the non interacting Haldane model. It is, thus, evident that the Haldane-Hubbard model can be implemented in optical lattices using techniques that have already been applied. To explore the whole interaction parameter space it is only necessary to adiabatically tune these Feshbach resonances.

With respect to the hopping parameters studied in Section 3.3, they are similar to those realized in the optical lattice implementation of the Haldane model [170]. The authors report the first neighbour hoppings to be $t_1/h = [-746(81), -527(17), -527(17)]$ Hz and the second neighbour hoppings $t_2/h = [14, 14, 61]$ Hz, with h the Planck's constant. The ratio of the hoppings $t_2/t_1 \sim 0.05$ is thus very similar to the one studied in our model. Supposing the heating issues with having two atomic levels in the lattice reported in Reference [170] can be overcome for laser assisted hopping, our model could easily be reproduced in state-of-the-art experiments. In addition, time of flight images, which we discuss later, can reveal the winding number of the system and characterize the complete topological phase diagram of the Haldane-Hubbard model [197].

3.6.2 Seeing topological edge and bulk currents in time of flight images

The results from this section are reported in our article: *Seeing topological edge and bulk currents in time-of-flight images* [177].

The bulk and edge particle density currents of the Haldane Hamiltonian inside the harmonic trap, discussed in Section 3.5.4, can be measured with time of flight (TOF) images in ultracold atoms experiments. This is a state-of-the-art method that allows to measure the density or velocity profiles of selected regions inside the lattice [167]. It works by swapping the internal state of the atoms of a selected region that one wants to observe. This other internal state does not see neither the effective Haldane Hamiltonian nor the

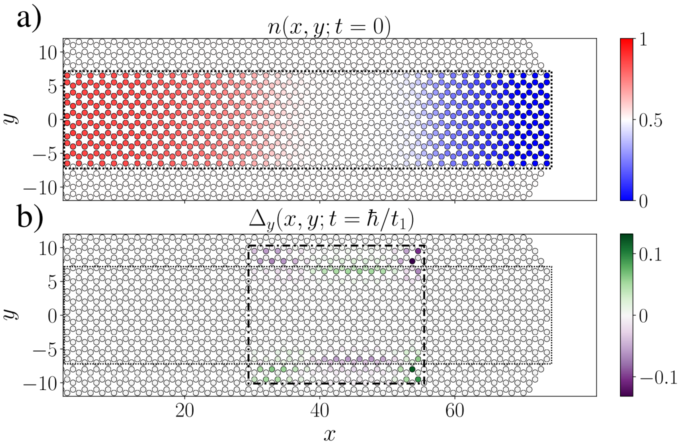

Figure 3.19: (a) Rectangular patch used to sample very short time TOF images. Only sites inside the patch are coloured, which show the initial site occupations $n(x, y; 0)$. (b) Relative population difference $\Delta_y(x, y; t)$ after letting the sample atoms expand for a short time $t = \hbar/t_1$. The dash dotted line shows the TOF measurement region.

harmonic trap and, thus, the atoms in this state are free to expand. One then lets this atom cloud expand for a certain amount of time and then takes a picture of this atom cloud after that time has passed. For very short times this amounts to almost not letting the atom cloud expand and the result is a density profile of the particles inside the selected region. For relatively long times one considers that the atom cloud is initially confined in a very small region in space $\sim \mathbf{x}(t_0)$ and that the final density distribution of the atom cloud is almost exclusively determined by their velocity distribution $\mathbf{x}(t) = \mathbf{x}(t_0) + \mathbf{v} \cdot (t - t_0) \sim \mathbf{v} \cdot (t - t_0)$, so the TOF picture displays a velocity profile. This selective imaging with varying times has already been used in ultracold atom experiments, see for example References [170, 207].

In the particular case of the Haldane model inside the harmonic potential of the optical lattice, releasing small samples of atoms inside the CI phase and at its boundaries can give information about the bulk and edge currents. This can be achieved both by employing long and short expansion times. For short times we select a rectangular sample as illustrated in Figure 3.19(a). By swapping the internal state of the atoms inside the selected region these atoms are left free to expand. After a very short expansion time t, proportional to the inverse tunneling of the Hamiltonian $\Delta t = \hbar/t_1$, an image is taken of the

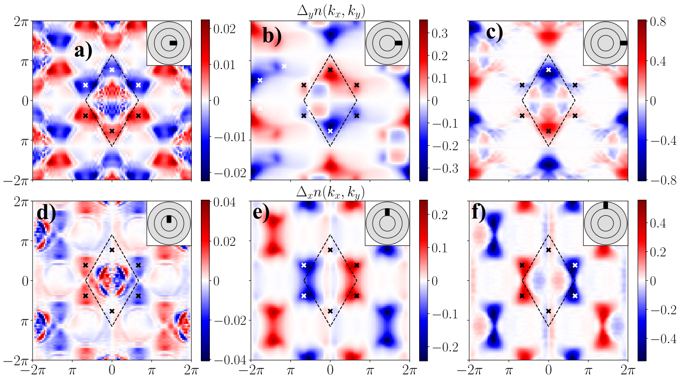

Figure 3.20: Relative velocity differences $\Delta_{x,y}(k_x, k_y)$ of samples taken from the topological (b,e) or from one of the trivial phases (a,c,d,f), as shown in the Insets. The exterior and interior annuli of the Inset represent the trivial regions, while the middle annulus represents the topological one.

expanded atom cloud and their density distribution is recorded. If there is a particle density current inside this region then, after the expansion, there should be a small population imbalance in the direction of the current. For an horizontal rectangular sample that stretches over the $y = 0$ line, as the one shown in Figure 3.19(a), the density imbalance can be measured by defining the relative population difference

$$\Delta_y(x, y; t) = [n(x, y; t) - n(x, -y; t)]/n(x, y; t). \tag{3.69}$$

To avoid singularities where the final density vanishes, we only measure with TOF images a smaller region than the starting one, as illustrated in Figure 3.19(b). The relative population difference is shown in Figure 3.19(b) for a lattice with 9800 sites and an harmonic potential $V_0 = -2.1$, $k = 5.8$, $r_{\max} = 43\sqrt{3}$. The pattern of the population difference clearly shows a displacement of particles towards $y > 0$ inside the CI phase and a displacement in the opposite direction, $y < 0$, at both edges of the CI. This pattern reveals the existence of a particle density current in the bulk of the CI and two edge currents counter propagating to it.

The density currents can also be extracted from long time TOF images. In this case, the procedure is to select smaller samples that only cover either the CI or one of the two trivial insulator phases, as sketched in the Insets of Figures 3.20(a-f). Then, one lets the sampled particles expand for longer times than the tunneling constant $t \gg \hbar/t_1$ and takes a picture of the resulting atom cloud, which outputs its velocity distribution $n(k_x,\, k_x)$. Similar to the shorter TOF images, we define the relative velocity differences

$$\begin{aligned}\Delta_x(k_x,k_y) =& \left[n(k_x,k_y) - n(-k_x,k_y)\right]/n(k_x,k_y)\\ \Delta_y(k_x,k_y) =& \left[n(k_x,k_y) - n(k_x,-k_y)\right]/n(k_x,k_y).\end{aligned} \tag{3.70}$$

These differences are shown as a colormap in Figures 3.20(a-f) for different starting samples in the lattice. When these samples are taken from the $y = 0$ axis (a-c), the trivial phases (a,c) show a positive Δ_y for particles going downwards, $k_y < 0$, while the CI phase (b) has more particles going upwards, $k_y > 0$. From here we infer the existence of currents moving upwards in the bulk of the CI phase and two currents going downwards at its two boundaries. Similarly, if the initial samples were taken in the axis $x = 0$, the bulk produces a leftwards moving density current that counter propagates to the two edge currents at the boundaries of the trivial phases, as shown in Figures 3.20(d-f).

The bulk and edge currents arise from the topological properties of the Haldane model and are proportional to the Chern number ν. Therefore, these currents must be resilient against thermal excitations and small inhomogeneities that do not change the topological phase. To evaluate its topological character we analyze the behaviour of the particle density currents measured from long time TOF images against temperature, random coupling disorder and random local disorder. Also, because the width k of the harmonic trap in optical lattices is an experimental parameter that can be tuned, we study the behaviour of the density currents against this width. To evaluate the topological nature of the currents we define the net long time TOF current as

$$\mathbf{I}_{\mathrm{TOF}} = \sum_{\mathbf{k}\in BZ} \mathbf{k}\, n(\mathbf{k}), \tag{3.71}$$

which is non zero if there is an imbalance of particles with opposite momentum in the BZ and outputs the direction and magnitude of the net density current. The velocity distribution $n(\mathbf{k})$ can be taken from initial samples of either the topological or the trivial regions to distinguish between bulk and edge currents.

The behaviour of the TOF currents with respect to the temperature T is shown in Figure 3.21(a), indicating that they are stable against small thermal excitations. Ultracold atom experiments with the Haldane model usually reach temperatures around $\sim 0.2T_F$ [170, 208] with T_F the Fermi temperature, which is inside the region where TOF currents are stable. In

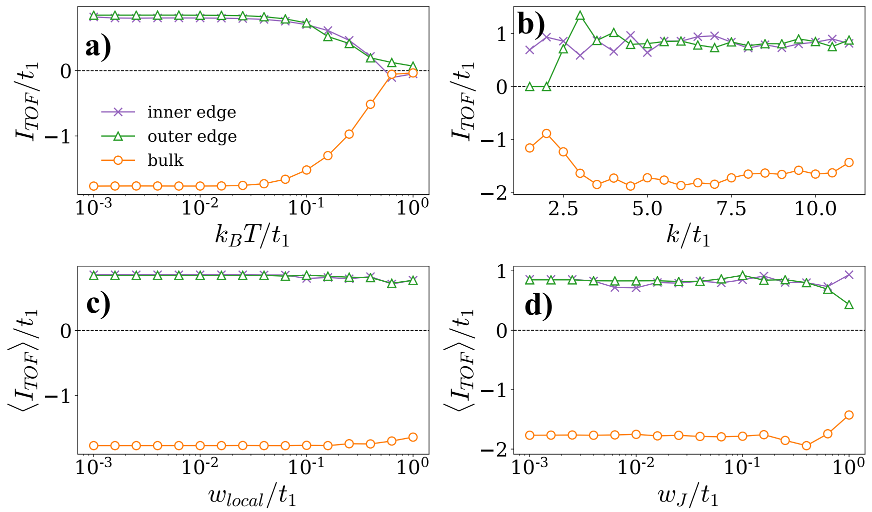

Figure 3.21: (a) Behaviour of the TOF current against temperature. (b) Stability of the TOF current with respect to different widths of the harmonic trap. (c,d) TOF currents against random local disorder (c) and random disorder in the lattice couplings (d).

Figure 3.21(b) we display the bulk and edge currents against the width of the harmonic trap k/t_1, showing that TOF currents are stable for a wide range of trap widths. In general, only temperature and the width of the harmonic trap are relevant parameters in an optical lattice. Therefore, our results show that bulk and edge currents can be observed in ultracold atoms. The lattices employed in these simulations have 9800 sites and, whenever these parameters are not varied, the system is at $T = 0$ and the trap parameters are $V_0 = -2$, $k = 5.5$, $r_{\max} = 38\sqrt{3}$.

To conclude with the topological characterization of the TOF currents we show in Figure 3.21(c) the average current when a local disorder potential is added at every site of the lattice with strengths drawn from the uniform distribution $(-w_{\text{local}}/2t_1,\, w_{\text{local}}/2t_1)$. Similarly, in Figure 3.21(d) the lattice couplings are multiplied by a factor drawn from the uniform distribution $(1 - w_J/2t_1,\, 1 + w_J/2t_1)$. In both cases the TOF currents are shown to be resilient against local and coupling inhomogeneities until they start to be comparable with the energy gap of the Haldane model. Nevertheless, in ultracold atom setups the level of disorder is usually very low, so the stability of TOF currents only depends on whether the temperature is lower than the energy of the gap.

3.7 Conclusions

In this Chapter we have studied three relevant topics in the field of topological insulators. We analysed the topological quantum phase diagram of the Haldane-Hubbard model and the emergence of bulk currents in the Haldane model when it is subject to an inhomogeneous potential. In addition, we made two proposals for the observation of the topological phases of the Haldane-Hubbard model and the bulk and edge currents in the Haldane model in optical lattices.

First, we have found that the CI phases of the Haldane model are able to survive in the presence of on-site interactions and extend until values of the interaction strength comparable to the kinetic energy of the system $|U| \sim t$. We were able to describe the quantum phase diagram by measuring the Chern number of the ground state, the double occupancy and staggered magnetization, which are related to magnetic ordering imposed by the Hubbard interactions. Above the CI phase of the Haldane model, in the strong repulsive regime the system becomes a Mott insulator that is topologically trivial and, between this region and the CI phase, we found traces of an intermediate CI phase with magnetic ordering. This phase has been found in the literature but there is yet no clear consensus on what its topological order is and whether it displays magnetic ordering or not. An interesting direction of research for the future could involve exploring this intermediate phase by allowing a non zero sublattice imbalance in the lattice, which is also non zero in the works that have found this phase. This would be of wide interest as it would point to a topological phase that might not be realized without interactions.

Second, the usual notion of TIs is that they have currents localized at their boundaries, while the bulk remains an insulator. We have challenged this notion by subjecting the Haldane model to a series of inhomogeneous potentials. Our results show that the inhomogeneities of the potential create localized states in the bulk of the system and that these localized states also give rise to currents localized in the bulk. These results were shown for a wide variety of potentials and were also derived from a perturbation theory analysis in the Haldane model on a cylinder. Contrary to the edge currents, the bulk currents do not have a predetermined form and can be controlled at will by reshaping the form of the potential. Furthermore, these localized currents are topological and are, thus, resilient against thermal excitations and random disorder in the lattice. These properties, along with the great versatility in controlling their shape, make the localized bulk currents great candidates for new technological applications.

Finally, we have shown how our models can be implemented in ultracold atom experiments. They all rely on the recent implementation of the Haldane model [170] and the possibility of measuring the Chern number using TOF images [197]. For the Haldane-Hubbard model the implementation can be done with state-of-the-art techniques, as the on-site interactions spontaneously arise in the ultracold atom implementation of the Haldane model and they are subsequently suppressed using Feshbach resonances. Exploring the whole interaction spectrum simply requires to adiabatically tune the Feshbach resonances, which can reach the whole attractive and negative interaction spectrum. On the other hand, for the observation of localized currents in the bulk of topological insulators we proposed to remake the Haldane model implementation of Reference [170]. The optical lattice in this experiment has two parts: one that simulates the Haldane Hamiltonian and another one that keeps the atoms trapped inside the lattice. We have shown that the latter, the trapping potential, is an inhomogeneous harmonic potential and, thus, has the ability to create bulk and edge currents in the Haldane model. We have proposed two different TOF measurements that can show the existence of particle density currents. Such experiments would be the first observation of topological edge and bulk currents in a topological insulator in optical lattices.

Appendices

Appendix A

Appendices

A.1 The DOCI 3-particle N-representability conditions

The B operators that give the 3-particle DOCI conditions are

$$\begin{aligned}
{}^3B_Q &= \sum_{i<j<k} a_i^\dagger a_j^\dagger a_k^\dagger + a_{\bar{i}}^\dagger a_{\bar{j}}^\dagger a_{\bar{k}}^\dagger + \sum_{i<j,k} a_i^\dagger a_j^\dagger a_{\bar{k}}^\dagger + a_k^\dagger a_{\bar{i}}^\dagger a_{\bar{j}}^\dagger \\
{}^3B_D &= \sum_{i<j<k} a_i a_j a_k + a_{\bar{i}} a_{\bar{j}} a_{\bar{k}} + \sum_{ijk} a_i a_j a_{\bar{k}} + a_k a_{\bar{i}} a_{\bar{j}} \\
{}^3B_F &= \sum_{i<j,k} a_i^\dagger a_j^\dagger a_k + a_i^\dagger a_j^\dagger a_{\bar{k}} + a_{\bar{i}}^\dagger a_{\bar{j}}^\dagger a_k + a_{\bar{i}}^\dagger a_{\bar{j}}^\dagger a_{\bar{k}} \\
&\quad + \sum_{ijk} a_i^\dagger a_{\bar{j}}^\dagger a_k + a_i^\dagger a_{\bar{j}}^\dagger a_{\bar{k}} + \sum_i a_i^\dagger + a_{\bar{i}}^\dagger \\
{}^3B_E &= \sum_{i,j<k} a_i^\dagger a_j a_k + a_i^\dagger a_{\bar{j}} a_{\bar{k}} + a_{\bar{i}}^\dagger a_j a_k + a_{\bar{i}}^\dagger a_{\bar{j}} a_{\bar{k}} \\
&\quad + \sum_{ijk} a_i^\dagger a_j a_{\bar{k}} + a_{\bar{i}}^\dagger a_j a_{\bar{k}} + \sum_i a_i + a_{\bar{i}}
\end{aligned} \tag{A.1}$$

We remember the DOCI 3-RDM elements

$$ {}^3D_{ijk} = \langle n_i n_j n_k \rangle, \quad \forall\ i \neq j \neq k \tag{A.2}$$

$$ {}^3\Pi^i_{jk} = \langle b_j^\dagger n_i b_k \rangle, \quad \forall\ i \neq j, k. \tag{A.3}$$

For the sake of simplicity we will not go through every block of the ${}^3B_\cdot$ operators. Instead, we will make a listing of the full 3-particle N-representability conditions:

- Diagonal conditions

$$ D_{ijk} \geq 0, \quad \forall\ i < j < k \tag{A.4}$$

$$ 1 - \rho_i - \rho_j - \rho_k + D_{ij} + D_{jk} + D_{ki} - {}^3D_{ijk} \geq 0, \quad \forall\ i < j < k. \tag{A.5}$$

- The 3-$\mathcal{P}$ and 3-$\mathcal{Q}$ conditions

$$ \Pi^a \succeq 0, \quad \forall\ a \tag{A.6}$$

and

$$\mathcal{Q}^a \succeq 0, \quad \forall\ a, \tag{A.7}$$

with

$$\mathcal{Q}^a_{ij} = -\Pi^a_{ij} + \Pi_{ji} + \delta_{ij}\left(1 - 2\rho_i - \rho_a + 2D_{ia}\right), \quad \forall\ ij \neq a. \tag{A.8}$$

- The two 3-$\mathcal{E}$ conditions:

$$^3\mathcal{E}_{abc} = \begin{pmatrix} D_{ab} - {}^3D_{abc} & \Pi^a_{bc} & \Pi^b_{ac} \\ \Pi^a_{bc} & D_{ac} - {}^3D_{abc} & \Pi^c_{ab} \\ \Pi^b_{ac} & \Pi^c_{ab} & D_{bc} - {}^3D_{abc} \end{pmatrix} \succeq 0, \quad \forall\, a < b < c. \tag{A.9}$$

and

$$^3\mathcal{E}_a = \begin{pmatrix} {}^3D_{aij} + \delta_{ij}D_{ai} & \Pi^i_{aj} & D_{ia} \\ \Pi^j_{ai} & \Pi_{ij} - \Pi^a_{ij} & \Pi_{ia} \\ D_{ai} & \Pi_{ai} & \rho_a \end{pmatrix} \succeq 0, \quad \forall\ a, ij \neq a. \tag{A.10}$$

- The two 3-$\mathcal{F}$ conditions:

$$^3\mathcal{F}_{abc} = \begin{pmatrix} \rho_a - D_{ab} - D_{ac} + {}^3D_{abc} & \Pi_{ac} - \Pi^b_{ac} & \Pi_{ab} - \Pi^c_{ab} \\ \Pi_{ac} - \Pi^b_{ac} & \rho_c - D_{bc} - D_{ac} + {}^3D_{abc} & \Pi_{bc} - \Pi^a_{bc} \\ \Pi_{ab} - \Pi^c_{ab} & \Pi_{bc} - \Pi^a_{bc} & \rho_b - D_{ab} - D_{bc} + {}^3D_{abc} \end{pmatrix}$$
$$^3\mathcal{F}_{abc} \quad \forall\ a < b < c. \tag{A.11}$$

and

$$^3\mathcal{F}_a = \begin{pmatrix} -{}^3D_{aij} + \delta_{ij}\left(\rho_i - D_{ai}\right) + D_{ij} & -\Pi^i_{aj} - \delta_{ij}\Pi_{ia} & \rho_i - D_{ia} \\ -\Pi^i_{aj} - \delta_{ij}\Pi_{ia} & \Pi^a_{ij} + \delta_{ij}\left(\rho_a - 2D_{ia}\right) & -\Pi_{ia} \\ \rho_i - D_{ai} & -\Pi_{ai} & 1 - \rho_a \end{pmatrix}$$
$$^3\mathcal{F}_a = \succeq 0, \quad \forall\ a, ij \neq a. \tag{A.12}$$

A.2 The DOCI 4-particle N-representability conditions

Due to its complexity, we will omit writing down the B operator, which includes all possible 4-particle operators with all possible spin combinations.

We remember the DOCI 4-RDM elements

$$\begin{aligned}\Pi_{ijkl} &= \langle b_i^\dagger b_j^\dagger b_l b_k \rangle, \quad \forall\, i \neq j \neq k \neq l \\ \Pi_{ij}^{kl} &= \langle b_i^\dagger b_j n_k n_l \rangle, \quad \forall\, i \neq j \neq k \neq l \\ D_{ijkl} &= \langle n_i n_j n_k n_l \rangle, \quad \forall i \neq j \neq k \neq l.\end{aligned} \tag{A.13}$$

The 4-particle N-representability conditions, summarized by their number and size, are

- The diagonal conditions. Size: 1×1, number: $L(L-1)(L-2)(L-3)/24$

$$D_{ijkl} \geq 0, \quad \forall\, i < j < k < l. \tag{A.14}$$

$$\begin{aligned}&1 - \rho_i - \rho_j - \rho_k - \rho_l + D_{ij} + D_{ik} + D_{il} + D_{jk} + D_{jl} + D_{kl} \\ &-D_{jkl} - D_{ikl} - D_{ijl} - D_{ijk} + D_{ijkl} \geq 0, \quad \forall\, i < j < k < l.\end{aligned} \tag{A.15}$$

- Size: $L \times L$, number: $L(L-1)/2$

$$\mathcal{A}_{ij}^{ab} = \Pi_{ij}^{ab}. \tag{A.16}$$

$$\begin{aligned}\mathcal{C}_{ij}^{ab} = &\Pi_{ij} - \Pi_{ij}^{a} - \Pi_{ij}^{b} + \Pi_{ij}^{ab} \\ &+ \delta_{ij} \left(1 - \rho_a - \rho_b - 2\rho_i + D_{ab} + 2D_{ia} + 2D_{ib} - 2D_{iab}\right)\end{aligned} \tag{A.17}$$

- Size: $L^2 \times L^2$, number: 1

$$\mathcal{B}_{ij,kl} = \Pi_{ijkl}. \tag{A.18}$$

$$\begin{aligned}\mathcal{Q}_{ij,kl} = &\Pi_{ijkl} + \delta_{ik}\left(\Pi_{lj} - 2\Pi_{lj}^{i}\right) + \delta_{jk}\left(\Pi_{li} - 2\Pi_{li}^{j}\right) + \delta_{il}\left(\Pi_{kj} - 2\Pi_{kj}^{i}\right) \\ &+ \delta_{jl}\left(\Pi_{ki} - 2\Pi_{ki}^{j}\right) + \delta_{ik}\delta_{jl}\left(1 - 2\rho_i - 2\rho_j + 4D_{ij}\right).\end{aligned} \tag{A.19}$$

- Size: 4×4, number: $L(L-1)(L-2)/6$

$$\begin{pmatrix} {}^3D_{abc} - {}^4D_{abcd} & \Pi^{bc}_{ad} & \Pi^{ac}_{bd} & \Pi^{ab}_{cd} \\ \Pi^{bc}_{ad} & {}^3D_{bcd} - {}^4D_{abcd} & \Pi^{cd}_{ab} & \Pi^{bd}_{ac} \\ \Pi^{ac}_{bd} & \Pi^{cd}_{ab} & {}^3D_{cda} - {}^4D_{abcd} & \Pi^{ad}_{bc} \\ \Pi^{ab}_{cd} & \Pi^{bd}_{ac} & \Pi^{ad}_{bc} & {}^3D_{dab} - {}^4D_{abcd} \end{pmatrix}, \quad \forall\ a < b < c, d \neq abc. \tag{A.20}$$

$$\begin{pmatrix} (a) & \Pi_{ab} - \Pi^c_{ab} - \Pi^d_{ab} + \Pi^{cd}_{ab} & \Pi_{ac} - \Pi^b_{ac} - \Pi^d_{ac} + \Pi^{bd}_{ac} & \Pi_{ad} - \Pi^b_{ad} - \Pi^c_{ad} + \Pi^{bc}_{ad} \\ & (b) & \Pi_{bc} - \Pi^a_{bc} - \Pi^d_{bc} + \Pi^{ad}_{bc} & \Pi_{bd} - \Pi^a_{bd} - \Pi^c_{bd} + \Pi^{ac}_{bd} \\ & & (c) & \Pi_{cd} - \Pi^a_{cd} - \Pi^b_{cd} + \Pi^{ab}_{bd} \\ & & & (d) \end{pmatrix}, \tag{A.21}$$

where the matrix is symmetric (not enough space). The () notation means

$$(a) = \rho_a - D_{ab} - D_{ac} - D_{ad} + D_{abc} + D_{abd} + D_{acd} - D_{abcd}. \tag{A.22}$$

- Size: $3L \times 3L$, number: $L(L-1)/2$

$$\begin{pmatrix} D_{ijab} & \Pi^{ia}_{jb} & \Pi^{ib}_{aj} \\ \Pi^{ja}_{ib} & \Pi^a_{ij} - \Pi^{ab}_{ij} & \Pi_{iajb} \\ \Pi^{jb}_{ia} & \Pi_{ibja} & \Pi^b_{ij} - \Pi^{ab}_{ij} \end{pmatrix}, \quad \forall\ ij \neq ab. \tag{A.23}$$

$$\begin{pmatrix} D_{ij} - D_{ija} - D_{ijb} + D_{ijab} & \Pi^i_{ja} - \Pi^{ib}_{ja} + \delta_{ij}\left(\Pi_{ia} - \Pi^b_{ia}\right) & a_1 \\ \Pi^j_{ia} - \Pi^{jb}_{ia} + \delta_{ij}\left(\Pi_{ja} - \Pi^b_{ja}\right) & \Pi^a_{ij} - \Pi^{ab}_{ij} + \delta_{ij}\left(\rho_a - D_{ab} - 2D_{ia} + 2D_{iab}\right) & a_2 \\ \Pi^j_{ib} - \Pi^{ja}_{ib} + \delta_{ij}\left(\Pi_{jb} - \Pi^a_{jb}\right) & \Pi_{aijb} + \delta_{ij}\left(\Pi_{ab} - 2\Pi^i_{ab}\right) & a_3 \end{pmatrix}, \tag{A.24}$$

with

$$\begin{aligned} a_1 &= \Pi^i_{jb} - \Pi^{ia}_{jb} + \delta_{ij}\left(\Pi_{ib} - \Pi^a_{ib}\right) \\ a_2 &= \Pi_{ajib} + \delta_{ij}\left(\Pi_{ab} - 2\Pi^i_{ab}\right) \\ a_3 &= \Pi^b_{ij} - \Pi^{ab}_{ij} + \delta_{ij}\left(\rho_b - D_{ab} - 2D_{ib} + 2D_{iab}\right) \end{aligned} \tag{A.25}$$

- Size: 6×6, number: $L(L-1)(L-2)(L-3)/24$

$$\begin{pmatrix} (ab) & \Pi^{a}_{bd} - \Pi^{ac}_{bd} & \Pi^{b}_{ad} - \Pi^{bc}_{ad} & \Pi^{a}_{bc} - \Pi^{ad}_{bc} & \Pi^{b}_{ac} - \Pi^{bd}_{ac} & \Pi_{abcd} \\ \Pi^{a}_{bd} - \Pi^{ac}_{bd} & (ad) & \Pi^{d}_{ab} - \Pi^{cd}_{ab} & \Pi^{a}_{cd} - \Pi^{ab}_{cd} & \Pi_{adbc} & \Pi^{d}_{ac} - \Pi^{bd}_{ac} \\ \Pi^{b}_{ad} - \Pi^{bc}_{ad} & \Pi^{d}_{ab} - \Pi^{cd}_{ab} & (bd) & \Pi_{bdac} & \Pi^{b}_{cd} - \Pi^{ab}_{cd} & \Pi^{d}_{bc} - \Pi^{ad}_{bc} \\ \Pi^{a}_{bc} - \Pi^{ad}_{bc} & \Pi^{a}_{cd} - \Pi^{ab}_{cd} & \Pi_{acbd} & (ac) & \Pi^{c}_{ab} - \Pi^{cd}_{ab} & \Pi^{c}_{ad} - \Pi^{bc}_{ad} \\ \Pi^{b}_{ac} - \Pi^{bd}_{ac} & \Pi_{bcad} & \Pi^{b}_{cd} - \Pi^{ab}_{cd} & \Pi^{c}_{ab} - \Pi^{cd}_{ab} & (bc) & \Pi^{c}_{bd} - \Pi^{ac}_{bd} \\ \Pi_{cdab} & \Pi^{d}_{ac} - \Pi^{bd}_{ac} & \Pi^{d}_{bc} - \Pi^{ad}_{bc} & \Pi^{c}_{ad} - \Pi^{bc}_{ad} & \Pi^{c}_{bd} - \Pi^{ac}_{bd} & (cd) \end{pmatrix}, \tag{A.26}$$

with, for example,

$$\begin{aligned} (ab) &= D_{ab} - D_{abc} - D_{abd} + D_{abcd} \\ (bc) &= D_{bc} - D_{abc} - D_{bcd} + D_{abcd}. \end{aligned} \tag{A.27}$$

- Size: $4L \times 4L$, number: $L(L-1)/2$

$$\begin{pmatrix} D_{ijb} - D_{ijab} & \Pi^{ij}_{ab} & \Pi^{ib}_{ja} + \delta_{ij}\Pi^{b}_{aj} & \Pi^{i}_{jb} - \Pi^{ia}_{jb} \\ \Pi^{ij}_{ab} & D_{ija} - D_{ijab} & \Pi^{ia}_{jb} + \delta_{ij}\Pi^{a}_{bj} & \Pi^{i}_{ja} - \Pi^{ib}_{ja} \\ \Pi^{jb}_{ia} + \delta_{ij}\Pi^{b}_{aj} & \Pi^{aj}_{ib} + \delta_{ij}\Pi^{a}_{bj} & \Pi^{ab}_{ij} + \delta_{ij}\left(D_{ab} - 2D_{iab}\right) & \Pi_{abij} \\ \Pi^{j}_{ib} - \Pi^{ja}_{ib} & \Pi^{j}_{ia} - \Pi^{jb}_{ia} & \Pi_{ijba} & \Pi_{ij} - \Pi^{a}_{ij} - \Pi^{b}_{ij} + \Pi^{ab}_{ij} \end{pmatrix}. \tag{A.28}$$

- Size: $(3L^2 - 2L)/2 \times (3L^2 - 2L)/2$, number: 1

$$\mathcal{R}_{ij,kl} = \begin{pmatrix} \Pi_{iljk} + \delta_{jl}\left(\Pi_{ik} - 2\Pi^{j}_{ik}\right) & \Pi^{kl}_{ij} + \delta_{jk}\Pi^{l}_{ij} + \delta_{jl}\Pi^{k}_{ij} & \Pi^{k}_{ij} + \delta_{jk}\Pi_{ij} \\ \Pi^{ij}_{kl} + \delta_{il}\Pi^{j}_{kl} + \delta_{jl}\Pi^{i}_{kl} & D_{ijkl} & D_{ijk} \\ \Pi^{i}_{kl} + \delta_{il}\Pi_{kl} & D_{ikl} & D_{ik} \end{pmatrix} \succeq 0 \tag{A.29}$$

A.3 Perturbation theory analysis of the $p = \pi$ modes of the Haldane model inside a cylinder

As has been noted in the main text, the Haldane mode in the cylinder with momentum $p = \pi$ (3.57) is equivalent to a SSH model with complex second neighbour hoppings t_2

$$\begin{aligned} H &= H_0 + V_t \\ H_0 &= t_1 \sum_{j=1}^{L_y} \left(b_j^\dagger a_{j+1} + \text{h.c.} \right) + \sum_j \left[V_a(j) a_j^\dagger a_j + V_b(j) b_j^\dagger b_j \right] \\ V_t &= t_2 \sum_j \left(2i\ a_j^\dagger a_{j+1} - 2i\ b_y^\dagger b_{j+1} + \text{h.c.} \right), \end{aligned} \tag{A.30}$$

where the second neighbour hoppings can be considered to be sufficiently small $t_2 \ll t_1$ so that we can do a perturbation theory analysis of the $p = \pi$ mode. The potential $V_{a,b}(j)$ is taken to be a simple potential step (3.58) of height $2w$. This step is located between sites $b_{s-1}^\dagger$ and $a_s^\dagger$.

A.3.1 SSH chain modes

The eigenstates of the unperturbed Hamiltonian H_0 can be written as products of localized dimers

$$|j,-\rangle_0 = \left(\alpha_j a_j^\dagger - \beta_{j-1} b_{j-1}^\dagger \right) |0\rangle, \quad |j,+\rangle_0 = \left(\beta_{j-1} a_j^\dagger + \alpha_j b_{j-1}^\dagger \right) |0\rangle. \tag{A.31}$$

where $\alpha_j,\ \beta_j > 0$ and $|j,-\rangle$ is the lowest energy mode. Because the boundary sites $j = \{1, L\}$ are decoupled from the rest of the chain, there are two localized edge modes

$$|L\rangle_0 = a_1^\dagger |0\rangle, \quad |R\rangle_0 = b_{L_y}^\dagger |0\rangle. \tag{A.32}$$

For all bulk dimers that are not in the edge [See Figure 3.11], the mode parameters are $\alpha_j = \beta_{j-1} = 1/\sqrt{2}$, while for the dimer mode at the potential step these are

$$\begin{aligned} \alpha_s &= \sqrt{\frac{r-w}{2r}} = \frac{1}{\sqrt{2}} \left(1 - \frac{w}{2t_1} \right) + \mathcal{O}\left(\frac{w^2}{t_1^2} \right) \\ \beta_{s-1} &= \frac{t_1}{\sqrt{2r(r-w)}} = \frac{1}{\sqrt{2}} \left(1 + \frac{w}{2t_1} \right) + \mathcal{O}\left(\frac{w^2}{t_1^2} \right), \end{aligned} \tag{A.33}$$

with $r = \sqrt{t_1^2 + w^2}$. The energy of these modes is summarized in Table A.1.

First order perturbation expansion

At first order in t_2/t_1 the energy of the modes of the SSH chain is not perturbed

$$\varepsilon^1_{j,\phi} = \langle j, \phi|_0 V_t |j, \phi\rangle_0 = 0, \quad \forall\ j \in [1, L_y]\,,\ \phi \in \{+, -\}\,. \tag{A.34}$$

However, the modes are affected by the perturbation potential $V_t \propto t_2$ (A.33)

$$|j, \phi\rangle_1 = |j, \phi\rangle_0 + \sum_{k:\varepsilon^0_{k,\phi'} \neq \varepsilon^0_{j,\phi}} \frac{\langle k, \phi'|_0 V_t |j, \phi\rangle_0}{\varepsilon^0_{j,\phi} - \varepsilon^0_{k,\phi'}} |k, \phi'\rangle_0. \tag{A.35}$$

Due to the particular form of V_t, the perturbed modes result in a combination of the nearest neighbours

$$|j, \phi\rangle_1 = |j, \phi\rangle_0 + t_2\, c_{j+1} |j + 1, \phi\rangle_0 + t_2\, c_{j-1} |j - 1, \phi\rangle_0, \tag{A.36}$$

with $c_{j\pm1}$ determined from the previous equation.

Correlations inside the chain

With the dimers to first order in t_2/t_1 we can compute the correlations between neighbouring dimers that emerge from each single mode

$$\begin{aligned} \theta_{j\phi} &= \langle j, \phi|_1\, a^\dagger_j b_j\, |j, \phi\rangle_1 \\ \varphi_{j\phi} &= \langle j, \phi|_1\, a^\dagger_{j-1} b_{j-1}\, |j, \phi\rangle_1. \end{aligned} \tag{A.37}$$

These values are summarized in Table A.1 for the lowest energy modes of the SSH chain with the step potential. At zero temperature and no chemical potential, the correlations between neighbouring dimers are given by the contributions of both dimers

$$\begin{aligned} \langle a^\dagger_j b_j\rangle &= \theta_{j-} + \varphi_{j+1,-} \\ &= 2it_2\, (\beta_{j-1}\alpha_{j+1} + \alpha_j\beta_j) \left(\frac{\beta_{j-1}\beta_j}{\varepsilon^0_{j+1,-} - \varepsilon^0_{j+}} - \frac{\alpha_j\alpha_{j+1}}{\varepsilon^0_{j-} - \varepsilon^0_{j+1,+}} \right). \end{aligned} \tag{A.38}$$

The correlations can be interpreted as two contributions from each dimer with different sign each. If the two dimers have equal energies $\varepsilon^0_{j+1,\pm} = \varepsilon^0_{j\pm}$ and their population density distribution is balanced in the form $\beta_{j-1}\beta_j = \alpha_j\alpha_{j+1}$, the magnitudes of their contributions to the correlations are equal and they cancel out. This is the case of the bulk modes. However, this balance does not exist for the step and edge modes and, therefore, there are correlations between them and their respectively nearest neighbouring modes.

Two-point currents in the cylinder

Using the formulas of the two-point currents J_{ij} (3.55) and of the two-point correlations (A.38), we can see that the latter give rise to localized currents at the edges of the cylinder

$$J_{a_1,b_1} = 2\,t_2, \quad J_{a_{L_y},b_{L_y}} = 2\,t_2. \tag{A.39}$$

and at both sides of the potential step

$$\begin{aligned} J_{a_{s-1},b_{s-1}} &= -2\,\frac{t_2\,w}{t_1} + \mathcal{O}\left(t_2\frac{w^2}{t_1^2}\right) \\ J_{a_s,b_s} &= -2\,\frac{t_2\,w}{t_1} + \mathcal{O}\left(t_2\frac{w^2}{t_1^2}\right). \end{aligned} \tag{A.40}$$

These currents come from the imbalance between the edge modes and the dimer modes with respect to the other bulk modes. It can be interpreted as each mode producing two counter propagating currents at its sites and, if two nearest neighbouring modes have the same characteristics, their currents cancel out, as is the case of the bulk dimers. Otherwise, the magnitudes of the currents are different and produce a net current.

A.3.2 Dispersion relation at $p = \pi$

The continuum model of edge currents (3.36) tells us that there needs to be a non zero dispersion relation of the boundary modes in order to be an edge current. This dispersion relation can be computed in perturbation theory by considering an offset in the potential $p = \pi + \delta p$ as a perturbation potential V_p of the SSH Hamiltonian for the modes $p = \pi$

$$\frac{d\varepsilon_j}{dp}(p = \pi) = \lim_{\delta p \to 0} \frac{\varepsilon_j\left(\pi + \delta p\right) - \varepsilon_j\left(\pi\right)}{\delta p} = \langle j, -|_1 | j, -\rangle_1, \tag{A.41}$$

with $\varepsilon_j(q)$ the dimer mode energies of the SSH chain at first order in t_2/t_1 and at momentum $p = q$ and the offset perturbation potential

$$\begin{aligned} V_p = \delta p\ t_1 \sum_j^{L_y} \left(-i a_j^\dagger b_j + \text{h.c.}\right) &+ 2\delta p\ t_2 \sum_j \left(a_j^\dagger a_j - b_j^\dagger b_j\right) \\ + \delta p\ t_2 \sum_j &\left(-a_j^\dagger a_{j+1} + b_j^\dagger b_{j+1} + \text{h.c.}\right). \end{aligned} \tag{A.42}$$

For each mode $|j,\pm\rangle_1$ we define the following expectation values

$$\begin{aligned}
\chi_j &= \langle j,\phi|_1 \left(a_j^\dagger a_j - b_{j-1}^\dagger b_{j-1} \right) |j,\phi\rangle_1 \\
\sigma_j^a &= \langle j,\phi|_1 a_j^\dagger a_{j+1} |j,\phi\rangle_1, \quad \sigma_j^b = \langle j,\phi|_1 b_{j-1}^\dagger b_j |j,\phi\rangle_1 \\
\tau_j^a &= \langle j,\phi|_1 a_{j-1}^\dagger a_j |j,\phi\rangle_1, \quad \tau_j^b = \langle j,\phi|_1 b_{j-2}^\dagger b_{j-1} |j,\phi\rangle_1 .
\end{aligned} \tag{A.43}$$

from which the expression of the dispersion relation for a mode $|j,\phi\rangle$ with $p = \pi$ is

$$\begin{aligned}
\frac{d\varepsilon_{j\phi}}{dp} &= 2t_1 \,\mathrm{Im}\left\{\theta_{j\phi} + \varphi_{j\phi}\right\} + 2t_2 \chi_{j\phi} \\
&\quad + 2t_2 \,\mathrm{Re}\left\{-\sigma_{j\phi}^a - \tau_{j\phi}^a + \sigma_{j\phi}^b + \tau_{j\phi}^b\right\} .
\end{aligned} \tag{A.44}$$

The elements $\theta, \varphi, \sigma, \tau$ are imaginary at first order in t_2/t_1 and the dispersion relation is written in a simpler form

$$\frac{d\varepsilon_{j\phi}}{dp} = \; 2t_1 \,\mathrm{Im}\left\{\theta_{j\phi} + \varphi_{j\phi}\right\} + 2t_2 \chi_{j\phi}. \tag{A.45}$$

We present the relevant values of $\chi_{j\phi}$ in Table A.1 for the modes with negative energy. Evaluating this expression, we find for the modes localized at the step

$$\frac{d\varepsilon_{s\pm}}{dp} = \pm 6 \frac{w t_2}{t_1} + \mathcal{O}\left(t_2 \frac{w^2}{t_1^2} \right) \tag{A.46}$$

and for the edge modes

$$\frac{d\varepsilon_L}{dp} = 6t_2, \quad \frac{d\varepsilon_R}{dp} = -6t_2. \tag{A.47}$$

With respect to the bulk modes, their dispersion relation is zero except for the modes that are nearest neighbour to the potential step and both edges, for which

$$\frac{d\varepsilon_{2-}}{dp} = -\frac{d\varepsilon_{s-1,-}}{dp} = \frac{d\varepsilon_{s+1,-}}{dp} = -\frac{d\varepsilon_{L_y,-}}{dp} = -t_2. \tag{A.48}$$

j	φ_{j-}	θ_{j-}	χ_{j-}	$\varepsilon^0_{j\pm}$
L	0	$2i\frac{t_2}{t_1}$	1	$-w$
2	$-i\frac{t_2}{t_1}$	$i\frac{t_2}{2t_1}$	0	$\pm t_1 - w$
$2 < j < s-1$	$-i\frac{t_2}{2t_1}$	$i\frac{t_2}{2t_1}$	0	$\pm t_1 - w$
$s-1$	$-i\frac{t_2}{2t_1}$	$i\frac{t_2}{t_1}$	0	$\pm t_1 - w$
s	$-i\frac{t_2(1+w)}{t_1}$	$i\frac{t_2(1-w)}{t_1}$	$-\frac{w}{t_1}$	$\pm\sqrt{t_1^2 + w^2}$
$s+1$	$-i\frac{t_2}{t_1}$	$i\frac{t_2}{2t_1}$	0	$\pm t_1 + w$
$s+1 < j < L_y$	$-i\frac{t_2}{2t_1}$	$i\frac{t_2}{2t_1}$	0	$\pm t_1 + w$
L_y	$-i\frac{t_2}{2t_1}$	$i\frac{t_2}{t_1}$	0	$\pm t_1 + w$
R	$-2i\frac{t_2}{t_1}$	0	-1	$+w$

Table A.1: Values of $\theta, \varphi, \chi, \varepsilon$ to first order in w, t_2 for the edge, bulk and potential step modes with lowest energy. L ($j = 1$) and R ($j = L_y$) correspond to the left and right boundary modes, respectively, while the potential step mode is at $j = s$.

Bibliography

[1] M. Aspelmeyer, T. J. Kippenberg, and F. Marquardt, “Cavity optomechanics”, Rev. Mod. Phys. **86**, 1391–1452 (2014).

[2] M. Fitzpatrick, N. M. Sundaresan, A. C. Y. Li, J. Koch, and A. A. Houck, “Observation of a dissipative phase transition in a one-dimensional circuit qed lattice”, Phys. Rev. X **7**, 011016 (2017).

[3] A. A. Houck, H. E. Türeci, and J. Koch, “On-chip quantum simulation with superconducting circuits”, Nature Physics **8**, 292–299 (2012).

[4] K. Temme, S. Bravyi, and J. M. Gambetta, “Error mitigation for short-depth quantum circuits”, Phys. Rev. Lett. **119**, 180509 (2017).

[5] F. A. Buot, *Nonequilibrium quantum transport physics in nanosystems: foundation of computational nonequilibrium physics in nanoscience and nanotechnology* (World Scientific, 2009).

[6] T. Xin, S.-J. Wei, J. S. Pedernales, E. Solano, and G.-L. Long, “Quantum simulation of quantum channels in nuclear magnetic resonance”, Phys. Rev. A **96**, 062303 (2017).

[7] J. Kasprzak, M. Richard, S. Kundermann, A. Baas, P. Jeambrun, J. M. J. Keeling, F. M. Marchetti, M. H. Szymańska, R. André, J. L. Staehli, V. Savona, P. B. Littlewood, B. Deveaud, and L. S. Dang, “Bose–einstein condensation of exciton polaritons”, Nature **443**, 409–414 (2006).

[8] V. Gorini, A. Kossakowski, and E. C. G. Sudarshan, “Completely positive dynamical semigroups of n-level systems”, Journal of Mathematical Physics **17**, 821–825 (1976).

[9] G. Lindblad, “On the generators of quantum dynamical semigroups”, Communications in Mathematical Physics **48**, 119–130 (1976).

[10] T. Prosen, “Third quantization: a general method to solve master equations for quadratic open fermi systems”, New Journal of Physics **10**, 043026 (2008).

[11] T. Prosen and T. H. Seligman, “Quantization over boson operator spaces”, Journal of Physics A: Mathematical and Theoretical **43**, 392004 (2010).

[12] M. V. Medvedyeva, F. H. L. Essler, and T. Prosen, “Exact bethe ansatz spectrum of a tight-binding chain with dephasing noise”, Phys. Rev. Lett. **117**, 137202 (2016).

[13] D. A. Rowlands and A. Lamacraft, “Noisy spins and the richardson-gaudin model”, Phys. Rev. Lett. **120**, 090401 (2018).

[14] P. Ribeiro and T. ž. Prosen, “Integrable quantum dynamics of open collective spin models”, Phys. Rev. Lett. **122**, 010401 (2019).

[15] S. Denisov, T. Laptyeva, W. Tarnowski, D. Chru ści ński, and K. Życzkowski, “Universal spectra of random lindblad operators”, Phys. Rev. Lett. **123**, 140403 (2019).

[16] L. Sá, P. Ribeiro, and T. Prosen, “Spectral and steady-state properties of random liouvillians”, Journal of Physics A: Mathematical and Theoretical **53**, 305303 (2020).

[17] A. B. Jaiswal, A. Pandey, and R. Prakash, “Universality classes of quantum chaotic dissipative systems”, EPL (Europhysics Letters) **127**, 30004 (2019).

[18] R. Hamazaki, K. Kawabata, N. Kura, and M. Ueda, “Universality classes of non-hermitian random matrices”, Phys. Rev. Research **2**, 023286 (2020).

[19] J. Ginibre, “Statistical ensembles of complex, quaternion, and real matrices”, Journal of Mathematical Physics **6**, 440–449 (1965).

[20] G. Akemann, M. Kieburg, A. Mielke, and T. Prosen, “Universal signature from integrability to chaos in dissipative open quantum systems”, Phys. Rev. Lett. **123**, 254101 (2019).

[21] S. Lerma-Hernández, A. Rubio-García, and J. Dukelsky, “Trigonometric SU(n) richardson-gaudin models and dissipative multi-level atomic systems”, Journal of Physics A: Mathematical and Theoretical **53**, 395302 (2020).

[22] Á. Rubio-García, R. A. Molina, and J. Dukelsky, *From integrability to chaos in quantum liouvillians*, 2021.

[23] H. Bethe, "Zur theorie der metalle", Zeitschrift für Physik **71**, 205–226 (1931).

[24] E. H. Lieb and F.-Y. Wu, "Absence of mott transition in an exact solution of the short-range, one-band model in one dimension", in *Exactly solvable models of strongly correlated electrons* (World Scientific, 1994), pp. 9–12.

[25] J. Dukelsky, C. Esebbag, and P. Schuck, "Class of exactly solvable pairing models", Phys. Rev. Lett. **87**, 066403 (2001).

[26] J. Dukelsky and P. Schuck, "Condensate fragmentation in a new exactly solvable model for confined bosons", Phys. Rev. Lett. **86**, 4207–4210 (2001).

[27] L. Amico, A. Di Lorenzo, and A. Osterloh, "Integrable model for interacting electrons in metallic grains", Phys. Rev. Lett. **86**, 5759–5762 (2001).

[28] J. von Delft and R. Poghossian, "Algebraic bethe ansatz for a discrete-state bcs pairing model", Phys. Rev. B **66**, 134502 (2002).

[29] J. Dukelsky, S. Pittel, and G. Sierra, "Colloquium: exactly solvable richardson-gaudin models for many-body quantum systems", Rev. Mod. Phys. **76**, 643–662 (2004).

[30] J. Bardeen, L. N. Cooper, and J. R. Schrieffer, "Theory of superconductivity", Phys. Rev. **108**, 1175–1204 (1957).

[31] S. Weigert, "The problem of quantum integrability", Physica D: Nonlinear Phenomena **56**, 107–119 (1992).

[32] J. Clemente-Gallardo and G. Marmo, "Towards a definition of quantum integrability", International Journal of Geometric Methods in Modern Physics **06**, 129–172 (2009).

[33] J.-S. Caux and J. Mossel, "Remarks on the notion of quantum integrability", Journal of Statistical Mechanics: Theory and Experiment **2011**, P02023 (2011).

[34] M. P. Grabowski and P. Mathieu, "Quantum integrals of motion for the heisenberg spin chain", Modern Physics Letters A **09**, 2197–2206 (1994).

[35] R. Richardson, “A restricted class of exact eigenstates of the pairing-force hamiltonian”, Physics Letters **3**, 277–279 (1963).

[36] R. Richardson and N. Sherman, “Exact eigenstates of the pairing-force hamiltonian”, Nuclear Physics **52**, 221–238 (1964).

[37] R. W. Richardson, “Numerical study of the 8-32-particle eigenstates of the pairing hamiltonian”, Phys. Rev. **141**, 949–956 (1966).

[38] R. W. Richardson, “Pairing in the limit of a large number of particles”, Journal of Mathematical Physics **18**, 1802–1811 (1977).

[39] Gaudin, M., “Diagonalisation d’une classe d’hamiltoniens de spin”, J. Phys. France **37**, 1087–1098 (1976).

[40] M. Gaudin, *La fonction d onde de Bethe*, Commissariat á l’Energie Atomique: série scientifique (Masson, Paris, 1983).

[41] P. Anderson, “Theory of dirty superconductors”, Journal of Physics and Chemistry of Solids **11**, 26–30 (1959).

[42] J. von Delft, A. D. Zaikin, D. S. Golubev, and W. Tichy, “Parity-affected superconductivity in ultrasmall metallic grains”, Phys. Rev. Lett. **77**, 3189–3192 (1996).

[43] F. Braun and J. von Delft, “Fixed-n superconductivity: the crossover from the bulk to the few-electron limit”, Phys. Rev. Lett. **81**, 4712–4715 (1998).

[44] M. Cambiaggio, A. Rivas, and M. Saraceno, “Integrability of the pairing hamiltonian”, Nuclear Physics A **624**, 157–167 (1997).

[45] J. von Delft and F. Braun, “Superconductivity in ultrasmall grains: introduction to richardson’s exact solution”, in , edited by I. Kulik and R. Ellialtioglu (1999), p. 361.

[46] G. Sierra, J. Dukelsky, G. G. Dussel, J. von Delft, and F. Braun, “Exact study of the effect of level statistics in ultrasmall superconducting grains”, Phys. Rev. B **61**, R11890–R11893 (2000).

[47] J. Roman, G. Sierra, and J. Dukelsky, “Large-n limit of the exactly solvable bcs model: analytics versus numerics”, Nuclear Physics B **634**, 483–510 (2002).

[48] J. M. Román, G. Sierra, and J. Dukelsky, “Elementary excitations of the bcs model in the canonical ensemble”, Phys. Rev. B **67**, 064510 (2003).

[49] H.-Q. Zhou, J. Links, R. H. McKenzie, and M. D. Gould, "Superconducting correlations in metallic nanoparticles: exact solution of the bcs model by the algebraic bethe ansatz", Phys. Rev. B **65**, 060502 (2002).

[50] J. Links, H.-Q. Zhou, R. H. McKenzie, and M. D. Gould, "Algebraic bethe ansatz method for the exact calculation of energy spectra and form factors: applications to models of bose einstein condensates and metallic nanograins", Journal of Physics A: Mathematical and General **36**, R63–R104 (2003).

[51] M. Ibañez, J. Links, G. Sierra, and S.-Y. Zhao, "Exactly solvable pairing model for superconductors with $p_x + ip_y$-wave symmetry", Phys. Rev. B **79**, 180501 (2009).

[52] C. Dunning, M. Ibañez, J. Links, G. Sierra, and S.-Y. Zhao, "Exact solution of the $p_x + ip_y$ pairing hamiltonian and a hierarchy of integrable models", Journal of Statistical Mechanics: Theory and Experiment **2010**, P08025 (2010).

[53] S. M. A. Rombouts, J. Dukelsky, and G. Ortiz, "Quantum phase diagram of the integrable $p_x + ip_y$ fermionic superfluid", Phys. Rev. B **82**, 224510 (2010).

[54] G. Ortiz, J. Dukelsky, E. Cobanera, C. Esebbag, and C. Beenakker, "Many-body characterization of particle-conserving topological superfluids", Phys. Rev. Lett. **113**, 267002 (2014).

[55] A. Y. Kitaev, "Unpaired majorana fermions in quantum wires", Physics-Uspekhi **44**, 131–136 (2001).

[56] P. W. Claeys, C. Dimo, S. D. Baerdemacker, and A. Faribault, "Integrable spin-1/2 richardson-gaudin xyz models in an arbitrary magnetic field", Journal of Physics A: Mathematical and Theoretical **52**, 08LT01 (2019).

[57] P. W. Claeys, S. De Baerdemacker, M. Van Raemdonck, and D. Van Neck, "Eigenvalue-based method and form-factor determinant representations for integrable xxz richardson-gaudin models", Phys. Rev. B **91**, 155102 (2015).

[58] G. Ortiz, R. Somma, J. Dukelsky, and S. Rombouts, "Exactly-solvable models derived from a generalized gaudin algebra", Nuclear Physics B **707**, 421–457 (2005).

[59] G. Moore and N. Read, "Nonabelions in the fractional quantum hall effect", Nuclear Physics B **360**, 362–396 (1991).

[60] M. Greiter, X.-G. Wen, and F. Wilczek, "Paired hall state at half filling", Phys. Rev. Lett. **66**, 3205–3208 (1991).

[61] M. Greiter, X. G. Wen, and F. Wilczek, "Paired hall states in double-layer electron systems", Phys. Rev. B **46**, 9586–9589 (1992).

[62] N. Read and D. Green, "Paired states of fermions in two dimensions with breaking of parity and time-reversal symmetries and the fractional quantum hall effect", Phys. Rev. B **61**, 10267–10297 (2000).

[63] F. Breuer Heinz-Peter and Petruccione, *The theory of open quantum systems* (Oxford University Press, Oxford, 2007).

[64] F. Minganti, A. Biella, N. Bartolo, and C. Ciuti, "Spectral theory of liouvillians for dissipative phase transitions", Phys. Rev. A **98**, 042118 (2018).

[65] S. F. Huelga et al., *Open quantum systems: an introduction* (Springer, 2012).

[66] V. V. Albert and L. Jiang, "Symmetries and conserved quantities in lindblad master equations", Phys. Rev. A **89**, 022118 (2014).

[67] M. van Caspel and V. Gritsev, "Symmetry-protected coherent relaxation of open quantum systems", Phys. Rev. A **97**, 052106 (2018).

[68] U. Kaup, P. Ring, and R. Nikam, "A microscopic boson model for collective transition nuclei: schwinger representation of the so(8) shell model algebra", Nuclear Physics A **480**, 222–252 (1988).

[69] D. P. Arovas and A. Auerbach, "Functional integral theories of low-dimensional quantum heisenberg models", Phys. Rev. B **38**, 316–332 (1988).

[70] M. Srednicki, "Chaos and quantum thermalization", Phys. Rev. E **50**, 888–901 (1994).

[71] M. Ueda, "Quantum equilibration, thermalization and prethermalization in ultracold atoms", Nature Reviews Physics **2**, 669–681 (2020).

[72] J. Maldacena, S. H. Shenker, and D. Stanford, "A bound on chaos", Journal of High Energy Physics **2016**, 106 (2016).

[73] R. J. Lewis-Swan, A. Safavi-Naini, J. J. Bollinger, and A. M. Rey, “Unifying scrambling, thermalization and entanglement through measurement of fidelity out-of-time-order correlators in the dicke model”, Nature Communications **10**, 1581 (2019).

[74] L. M. Sieberer, T. Olsacher, A. Elben, M. Heyl, P. Hauke, F. Haake, and P. Zoller, “Digital quantum simulation, trotter errors, and quantum chaos of the kicked top”, npj Quantum Information **5**, 78 (2019).

[75] F. Haake, *Quantum signatures of chaos* (Springer, 1991), pp. 583–595.

[76] O. Bohigas, M. J. Giannoni, and C. Schmit, “Characterization of chaotic quantum spectra and universality of level fluctuation laws”, Phys. Rev. Lett. **52**, 1–4 (1984).

[77] H.-J. Stöckmann, *Quantum chaos: an introduction* (Cambridge University Press, Cambridge, 1999).

[78] M. Gutzwiller, “Quantum chaos”, Scholarpedia **2**, 3146 (2007).

[79] J. Gómez, K. Kar, V. Kota, R. Molina, A. Relaño, and J. Retamosa, “Many-body quantum chaos: recent developments and applications to nuclei”, Physics Reports **499**, 103–226 (2011).

[80] S. Müller, S. Heusler, P. Braun, F. Haake, and A. Altland, “Semiclassical foundation of universality in quantum chaos”, Phys. Rev. Lett. **93**, 014103 (2004).

[81] S. Müller, S. Heusler, A. Altland, P. Braun, and F. Haake, “Periodic-orbit theory of universal level correlations in quantum chaos”, New Journal of Physics **11**, 103025 (2009).

[82] R. Grobe, F. Haake, and H.-J. Sommers, “Quantum distinction of regular and chaotic dissipative motion”, Phys. Rev. Lett. **61**, 1899–1902 (1988).

[83] L. Sá, P. Ribeiro, and T. Prosen, “Complex spacing ratios: a signature of dissipative quantum chaos”, Phys. Rev. X **10**, 021019 (2020).

[84] T. A. Brody, “A statistical measure for the repulsion of energy levels”, Lettere al Nuovo Cimento (1971-1985) **7**, 482–484 (1973).

[85] V. Oganesyan and D. A. Huse, “Localization of interacting fermions at high temperature”, Phys. Rev. B **75**, 155111 (2007).

[86] T. Peron, B. M. F. de Resende, F. A. Rodrigues, L. d. F. Costa, and J. A. Méndez-Bermúdez, “Spacing ratio characterization of the spectra of directed random networks”, Phys. Rev. E **102**, 062305 (2020).

[87] F. Coester, “Bound states of a many-particle system”, Nuclear Physics **7**, 421–424 (1958).

[88] R. J. Bartlett and M. Musiał, “Coupled-cluster theory in quantum chemistry”, Rev. Mod. Phys. **79**, 291–352 (2007).

[89] R. J. Bartlett and D. M. Silver, “Pair-correlation energies in sodium hydride with many-body perturbation theory”, Phys. Rev. A **10**, 1927–1931 (1974).

[90] D. L. Freeman, “Coupled-cluster expansion applied to the electron gas: inclusion of ring and exchange effects”, Phys. Rev. B **15**, 5512–5521 (1977).

[91] U. Schollwöck, “The density-matrix renormalization group”, Rev. Mod. Phys. **77**, 259–315 (2005).

[92] U. Schollwöck, “The density-matrix renormalization group in the age of matrix product states”, Annals of Physics **326**, January 2011 Special Issue, 96–192 (2011).

[93] W. M. C. Foulkes, L. Mitas, R. J. Needs, and G. Rajagopal, “Quantum monte carlo simulations of solids”, Rev. Mod. Phys. **73**, 33–83 (2001).

[94] A. Georges and G. Kotliar, “Hubbard model in infinite dimensions”, Phys. Rev. B **45**, 6479–6483 (1992).

[95] G. Kotliar, S. Y. Savrasov, K. Haule, V. S. Oudovenko, O. Parcollet, and C. A. Marianetti, “Electronic structure calculations with dynamical mean-field theory”, Rev. Mod. Phys. **78**, 865–951 (2006).

[96] G. Knizia and G. K.-L. Chan, “Density matrix embedding: a simple alternative to dynamical mean-field theory”, Phys. Rev. Lett. **109**, 186404 (2012).

[97] C. Garrod, M. V. Mihailovic, and M. Rosina, “The variational approach to the two-body density matrix”, Journal of Mathematical Physics **16**, 868–874 (1975).

[98] M. Nakata, H. Nakatsuji, M. Ehara, M. Fukuda, K. Nakata, and K. Fujisawa, "Variational calculations of fermion second-order reduced density matrices be semidefinite programming algorithm", Journal of Chemical Physics **114**, 8282–8292 (2001).

[99] M. Mihailovic and M. Rosina, "The variational approach to the density matrix for light nuclei", Nuclear Physics A **237**, 221–228 (1975).

[100] J. S. Anderson, M. Nakata, R. Igarashi, K. Fujisawa, and M. Yamashita, "The second-order reduced density matrix method and the two-dimensional hubbard model", Computational and Theoretical Chemistry **1003**, Reduced Density Matrices: A Simpler Approach to Many-Electron Problems?, 22–27 (2013).

[101] K. Husimi, "Some formal properties of the density matrix", Nippon Sugaku-Buturigakkwai Kizi Dai 3 Ki **22**, 264–314 (1940).

[102] P.-O. Löwdin, "Quantum theory of many-particle systems. i. physical interpretations by means of density matrices, natural spin-orbitals, and convergence problems in the method of configurational interaction", Phys. Rev. **97**, 1474–1489 (1955).

[103] J. E. Mayer, "Electron correlation", Phys. Rev. **100**, 1579–1586 (1955).

[104] R. H. Tredgold, "Density matrix and the many-body problem", Phys. Rev. **105**, 1421–1423 (1957).

[105] A. J. Coleman, "Structure of fermion density matrices", Rev. Mod. Phys. **35**, 668–686 (1963).

[106] F. Weinhold and E. B. Wilson, "Reduced density matrices of atoms and molecules. i. the 2 matrix of double-occupancy, configuration-interaction wavefunctions for singlet states", The Journal of Chemical Physics **46**, 2752–2758 (1967).

[107] L. Bytautas, T. M. Henderson, C. A. Jiménez-Hoyos, J. K. Ellis, and G. E. Scuseria, "Seniority and orbital symmetry as tools for establishing a full configuration interaction hierarchy", The Journal of Chemical Physics **135**, 044119 (2011).

[108] P. A. Limacher, P. W. Ayers, P. A. Johnson, S. De Baerdemacker, D. Van Neck, and P. Bultinck, "A new mean-field method suitable for strongly correlated electrons: computationally facile antisymmetric products of nonorthogonal geminals", Journal of Chemical Theory and Computation **9**, 1394–1401 (2013).

[109] D. R. Alcoba, A. Torre, L. Lain, G. E. Massaccesi, and O. B. Oña, "Seniority number in spin-adapted spaces and compactness of configuration interaction wave functions", The Journal of Chemical Physics **139**, 084103 (2013).

[110] A. Rubio-García, D. R. Alcoba, P. Capuzzi, and J. Dukelsky, "Benchmarking the variational reduced density matrix theory in the doubly occupied configuration interaction space with integrable pairing models", Journal of Chemical Theory and Computation **14**, 4183–4192 (2018).

[111] D. R. Alcoba, P. Capuzzi, A. Rubio-García, J. Dukelsky, G. E. Massaccesi, O. B. Oña, A. Torre, and L. Lain, "Variational reduced density matrix method in the doubly occupied configuration interaction space using three-particle n-representability conditions", The Journal of Chemical Physics **149**, 194105 (2018).

[112] A. Rubio-García, J. Dukelsky, D. R. Alcoba, P. Capuzzi, O. B. Oña, E. Ríos, A. Torre, and L. Lain, "Variational reduced density matrix method in the doubly-occupied configuration interaction space using four-particle n-representability conditions: application to the xxz model of quantum magnetism", The Journal of Chemical Physics **151**, 154104 (2019).

[113] G. E. Massaccesi, A. Rubio-García, P. Capuzzi, E. Ríos, O. B. Oña, J. Dukelsky, L. Lain, A. Torre, and D. R. Alcoba, "Variational determination of the two-particle reduced density matrix within the doubly occupied configuration interaction space: exploiting translational and reflection invariance", Journal of Statistical Mechanics: Theory and Experiment **2021**, 013110 (2021).

[114] D. A. Mazziotti, "Variational minimization of atomic and molecular ground-state energies via the two-particle reduced density matrix", Phys. Rev. A **65**, 062511 (2002).

[115] J. R. Hammond and D. A. Mazziotti, "Variational reduced-density-matrix calculation of the one-dimensional hubbard model", Phys. Rev. A **73**, 062505 (2006).

[116] B. Verstichel, H. van Aggelen, W. Poelmans, S. Wouters, and D. Van Neck, "Extensive v2dm study of the one-dimensional hubbard model for large lattice sizes: exploiting translational invariance and parity", Computational and Theoretical Chemistry **1003**, Reduced Density Matrices: A Simpler Approach to Many-Electron Problems?, 12–21 (2013).

[117] W. Poelmans, “Variational determination of the two-particle density matrix: the case of doubly-occupied space”, PhD thesis (Jan. 2015).

[118] M. Yamashita, K. Fujisawa, and M. Kojima, “Implementation and evaluation of sdpa 6.0 (semidefinite programming algorithm 6.0)”, Optimization Methods and Software **18**, 491–505 (2003).

[119] M. Yamashita, K. Fujisawa, K. Nakata, M. Nakata, M. Fukuda, K. Kobayashi, and K. Goto, “A high-performance software package for semidefinite programs: sdpa 7”, (2010).

[120] D. A. Mazziotti, “Large-scale semidefinite programming for many-electron quantum mechanics”, Phys. Rev. Lett. **106**, 083001 (2011).

[121] T. L. Allen and H. Shull, “Electron pairs in the beryllium atom”, The Journal of Physical Chemistry **66**, 2281–2283 (1962).

[122] D. W. Smith and S. J. Fogel, “Natural orbitals and geminals of the beryllium atom”, The Journal of Chemical Physics **43**, S91–S96 (1965).

[123] T. Perez and P. Cassam-Chenaï, “Generalization of the concepts of seniority number and ionicity”, Journal of Mathematical Chemistry **56**, 1428–1436 (2018).

[124] I. Shavitt, “The history and evolution of configuration interaction”, Molecular Physics **94**, 3–17 (1998).

[125] C. David Sherrill and H. F. Schaefer, “The configuration interaction method: advances in highly correlated approaches”, in , Vol. 34, edited by P.-O. Löwdin, J. R. Sabin, M. C. Zerner, and E. Brändas, Advances in Quantum Chemistry (Academic Press, 1999), pp. 143–269.

[126] M. Van Raemdonck, D. R. Alcoba, W. Poelmans, S. De Baerdemacker, A. Torre, L. Lain, G. E. Massaccesi, D. Van Neck, and P. Bultinck, “Polynomial scaling approximations and dynamic correlation corrections to doubly occupied configuration interaction wave functions”, The Journal of Chemical Physics **143**, 104106 (2015).

[127] C. N. Yang and C. P. Yang, “Ground-state energy of a heisenberg-ising lattice”, Phys. Rev. **147**, 303–306 (1966).

[128] A. Auerbach, *Interacting electrons and quantum magnetism* (Springer-Verlag, New York, 1994).

[129] V. I. Inozemtsev, "On the connection between the one-dimensional S=1/2 heisenberg chain and haldane-shastry model", Journal of Statistical Physics **59**, 1143–1155 (1990).

[130] B. S. Shastry, "Exact solution of an s=1/2 heisenberg antiferromagnetic chain with long-ranged interactions", Phys. Rev. Lett. **60**, 639–642 (1988).

[131] F. D. M. Haldane, "Exact jastrow-gutzwiller resonating-valence-bond ground state of the spin-1/2 antiferromagnetic heisenberg chain with $1/r^2$ exchange", Phys. Rev. Lett. **60**, 635–638 (1988).

[132] F. Finkel and A. González-López, "A new perspective on the integrability of inozemtsev's elliptic spin chain", Annals of Physics **351**, 797–827 (2014).

[133] H.-H. Tu and G. Sierra, "Infinite matrix product states, boundary conformal field theory, and the open haldane-shastry model", Phys. Rev. B **92**, 041119 (2015).

[134] R. Bishop, P. Li, R. Zinke, R. Darradi, J. Richter, D. Farnell, and J. Schulenburg, "The spin-half xxz antiferromagnet on the square lattice revisited: a high-order coupled cluster treatment", Journal of Magnetism and Magnetic Materials **428**, 178–188 (2017).

[135] K. v. Klitzing, G. Dorda, and M. Pepper, "New method for high-accuracy determination of the fine-structure constant based on quantized hall resistance", Phys. Rev. Lett. **45**, 494–497 (1980).

[136] R. B. Laughlin, "Quantized hall conductivity in two dimensions", Phys. Rev. B **23**, 5632–5633 (1981).

[137] D. C. Tsui, H. L. Stormer, and A. C. Gossard, "Two-dimensional magnetotransport in the extreme quantum limit", Phys. Rev. Lett. **48**, 1559–1562 (1982).

[138] R. B. Laughlin, "Anomalous quantum hall effect: an incompressible quantum fluid with fractionally charged excitations", Phys. Rev. Lett. **50**, 1395–1398 (1983).

[139] X.-G. Wen, "Topological orders and edge excitations in fractional quantum hall states", Advances in Physics **44**, 405–473 (1995).

[140] X. G. Wen, "Vacuum degeneracy of chiral spin states in compactified space", Phys. Rev. B **40**, 7387–7390 (1989).

[141] X. G. Wen and Q. Niu, "Ground-state degeneracy of the fractional quantum hall states in the presence of a random potential and on high-genus riemann surfaces", Phys. Rev. B **41**, 9377–9396 (1990).

[142] B. I. Halperin, "Quantized hall conductance, current-carrying edge states, and the existence of extended states in a two-dimensional disordered potential", Phys. Rev. B **25**, 2185–2190 (1982).

[143] Xiao-Gang Wen, Yong-Shi Wu, and Yasuhiro Hatsugai, "Chiral operator product algebra and edge excitations of a fractional quantum hall droplet", Nuclear Physics B **422**, 476–494 (1994).

[144] M. Z. Hasan and C. L. Kane, "Colloquium: topological insulators", Rev. Mod. Phys. **82**, 3045–3067 (2010).

[145] X.-L. Qi and S.-C. Zhang, "Topological insulators and superconductors", Rev. Mod. Phys. **83**, 1057–1110 (2011).

[146] B. A. Bernevig and T. L. Hughes (Princeton University Press, 2013), p. 260.

[147] Y. Hatsugai, "Edge states in the integer quantum hall effect and the riemann surface of the bloch function", Phys. Rev. B **48**, 11851–11862 (1993).

[148] Y. Hatsugai, "Chern number and edge states in the integer quantum hall effect", Phys. Rev. Lett. **71**, 3697–3700 (1993).

[149] S. Ryu and Y. Hatsugai, "Topological origin of zero-energy edge states in particle-hole symmetric systems", Phys. Rev. Lett. **89**, 077002 (2002).

[150] A. P. Schnyder, S. Ryu, A. Furusaki, and A. W. W. Ludwig, "Classification of topological insulators and superconductors in three spatial dimensions", Phys. Rev. B **78**, 195125 (2008).

[151] A. P. Schnyder, S. Ryu, A. Furusaki, and A. W. W. Ludwig, "Classification of topological insulators and superconductors", AIP Conference Proceedings **1134**, 10–21 (2009).

[152] A. Kitaev, "Periodic table for topological insulators and superconductors", AIP Conference Proceedings **1134**, 22–30 (2009).

[153] S. Ryu, A. P. Schnyder, A. Furusaki, and A. W. W. Ludwig, "Topological insulators and superconductors: tenfold way and dimensional hierarchy", New Journal of Physics **12**, 065010 (2010).

[154] D. J. Thouless, M. Kohmoto, M. P. Nightingale, and M. den Nijs, "Quantized hall conductance in a two-dimensional periodic potential", Phys. Rev. Lett. **49**, 405–408 (1982).

[155] M. Kohmoto, "Topological invariant and the quantization of the hall conductance", Annals of Physics **160**, 343–354 (1985).

[156] M. V. Berry and P. R. S. L. A, "Quantal phase factors accompanying adiabatic changes", Proceedings of the Royal Society of London. A. Mathematical and Physical Sciences **392**, 45–57 (1984).

[157] S. Ryu and Y. Hatsugai, "Entanglement entropy and the berry phase in the solid state", Phys. Rev. B **73**, 245115 (2006).

[158] C. L. Kane and E. J. Mele, "Quantum spin hall effect in graphene", Phys. Rev. Lett. **95**, 226801 (2005).

[159] C. L. Kane and E. J. Mele, "Z_2 topological order and the quantum spin hall effect", Phys. Rev. Lett. **95**, 146802 (2005).

[160] B. A. Bernevig, T. L. Hughes, and S.-C. Zhang, "Quantum spin hall effect and topological phase transition in hgte quantum wells", Science **314**, 1757–1761 (2006).

[161] M. König, S. Wiedmann, C. Brüne, A. Roth, H. Buhmann, L. W. Molenkamp, X.-L. Qi, and S.-C. Zhang, "Quantum spin hall insulator state in hgte quantum wells", Science **318**, 766–770 (2007).

[162] D. Hsieh, D. Qian, L. Wray, Y. Xia, Y. S. Hor, R. J. Cava, and M. Z. Hasan, "A topological dirac insulator in a quantum spin hall phase", Nature **452**, 970–974 (2008).

[163] H. Zhang, C.-X. Liu, X.-L. Qi, X. Dai, Z. Fang, and S.-C. Zhang, "Topological insulators in bi2se3, bi2te3 and sb2te3 with a single dirac cone on the surface", Nature Physics **5**, 438–442 (2009).

[164] Y. Xia, D. Qian, D. Hsieh, L. Wray, A. Pal, H. Lin, A. Bansil, D. Grauer, Y. S. Hor, R. J. Cava, and M. Z. Hasan, "Observation of a large-gap topological-insulator class with a single dirac cone on the surface", Nature Physics **5**, 398–402 (2009).

[165] D. Jaksch, C. Bruder, J. I. Cirac, C. W. Gardiner, and P. Zoller, "Cold bosonic atoms in optical lattices", Phys. Rev. Lett. **81**, 3108–3111 (1998).

[166] I. Bloch, “Ultracold quantum gases in optical lattices”, Nature Physics **1**, 23–30 (2005).

[167] I. Bloch, J. Dalibard, and W. Zwerger, “Many-body physics with ultracold gases”, Rev. Mod. Phys. **80**, 885–964 (2008).

[168] D. Jaksch and P. Zoller, “Creation of effective magnetic fields in optical lattices: the hofstadter butterfly for cold neutral atoms”, New Journal of Physics **5**, 56–56 (2003).

[169] G. Juzeli ūnas and P. Öhberg, “Slow light in degenerate fermi gases”, Phys. Rev. Lett. **93**, 033602 (2004).

[170] G. Jotzu, M. Messer, R. Desbuquois, M. Lebrat, T. Uehlinger, D. Greif, and T. Esslinger, “Experimental realization of the topological haldane model with ultracold fermions”, Nature **515**, 237–240 (2014).

[171] M. Aidelsburger, M. Atala, M. Lohse, J. T. Barreiro, B. Paredes, and I. Bloch, “Realization of the hofstadter hamiltonian with ultracold atoms in optical lattices”, Phys. Rev. Lett. **111**, 185301 (2013).

[172] M. Atala, M. Aidelsburger, J. T. Barreiro, D. Abanin, T. Kitagawa, E. Demler, and I. Bloch, “Direct measurement of the zak phase in topological bloch bands”, Nature Physics **9**, 795–800 (2013).

[173] J. H. Kang, J. H. Han, and Y. Shin, “Creutz ladder in a resonantly shaken 1d optical lattice”, New Journal of Physics **22**, 013023 (2020).

[174] F. D. M. Haldane, “Model for a quantum hall effect without landau levels: condensed-matter realization of the ”parity anomaly””, Phys. Rev. Lett. **61**, 2015–2018 (1988).

[175] A. Rubio-García and J. J. García-Ripoll, “Topological phases in the haldane model with spin–spin on-site interactions”, New Journal of Physics **20**, 043033 (2018).

[176] C. N. Self, A. Rubio-García, J. J. García-Ripoll, and J. K. Pachos, “Topological bulk states and their currents”, Phys. Rev. B **102**, 045424 (2020).

[177] A. Rubio-García, C. N. Self, J. J. García-Ripoll, and J. K. Pachos, “Seeing topological edge and bulk currents in time-of-flight images”, Phys. Rev. B **102**, 041123 (2020).

[178] Y. Hasegawa, R. Konno, H. Nakano, and M. Kohmoto, "Zero modes of tight-binding electrons on the honeycomb lattice", Phys. Rev. B **74**, 033413 (2006).

[179] B. Wunsch, F. Guinea, and F. Sols, "Dirac-point engineering and topological phase transitions in honeycomb optical lattices", New Journal of Physics **10**, 103027 (2008).

[180] J. de Lisle, S. De, E. Alba, A. Bullivant, J. J. Garcia-Ripoll, V. Lahtinen, and J. K. Pachos, "Detection of chern numbers and entanglement in topological two-species systems through subsystem winding numbers", New Journal of Physics **16**, 083022 (2014).

[181] S. Rachel, "Interacting topological insulators: a review", Reports on Progress in Physics **81**, 116501 (2018).

[182] E. Alba, J. K. Pachos, and J. J. García-Ripoll, "Winding number order in the haldane model with interactions", New Journal of Physics **18**, 033022 (2016).

[183] C. Hickey, P. Rath, and A. Paramekanti, "Competing chiral orders in the topological haldane-hubbard model of spin-$\frac{1}{2}$ fermions and bosons", Phys. Rev. B **91**, 134414 (2015).

[184] W. Zheng, H. Shen, Z. Wang, and H. Zhai, "Magnetic-order-driven topological transition in the haldane-hubbard model", Phys. Rev. B **91**, 161107 (2015).

[185] Y.-J. Wu, N. Li, and S.-P. Kou, "Chiral topological superfluids in the attractive haldane-hubbard model with opposite zeeman energy at two sublattice sites", The European Physical Journal B **88**, 255 (2015).

[186] V. S. Arun, R. Sohal, C. Hickey, and A. Paramekanti, "Mean field study of the topological haldane-hubbard model of spin-$\frac{1}{2}$ fermions", Phys. Rev. B **93**, 115110 (2016).

[187] C. Hickey, L. Cincio, Z. Papi ć, and A. Paramekanti, "Haldane-hubbard mott insulator: from tetrahedral spin crystal to chiral spin liquid", Phys. Rev. Lett. **116**, 137202 (2016).

[188] J. Imri ška, L. Wang, and M. Troyer, "First-order topological phase transition of the haldane-hubbard model", Phys. Rev. B **94**, 035109 (2016).

[189] J. Wu, J. P. L. Faye, D. Sénéchal, and J. Maciejko, “Quantum cluster approach to the spinful haldane-hubbard model”, Phys. Rev. B **93**, 075131 (2016).

[190] T. I. Vanhala, T. Siro, L. Liang, M. Troyer, A. Harju, and P. Törmä, “Topological phase transitions in the repulsively interacting haldane-hubbard model”, Phys. Rev. Lett. **116**, 225305 (2016).

[191] Y.-C. Zhang, Z. Xu, and S. Zhang, “Topological superfluids and the bec-bcs crossover in the attractive haldane-hubbard model”, Phys. Rev. A **95**, 043640 (2017).

[192] Z.-L. Gu, K. Li, and J.-X. Li, “Quantum cluster approach to the topological invariants in correlated chern insulators”, New Journal of Physics **21**, 073016 (2019).

[193] S. Rachel and K. Le Hur, “Topological insulators and mott physics from the hubbard interaction”, Phys. Rev. B **82**, 075106 (2010).

[194] M. Hohenadler, Z. Y. Meng, T. C. Lang, S. Wessel, A. Muramatsu, and F. F. Assaad, “Quantum phase transitions in the kane-mele-hubbard model”, Phys. Rev. B **85**, 115132 (2012).

[195] Y.-L. Wu, B. A. Bernevig, and N. Regnault, “Zoology of fractional chern insulators”, Phys. Rev. B **85**, 075116 (2012).

[196] S. R. White, “Density matrix formulation for quantum renormalization groups”, Phys. Rev. Lett. **69**, 2863–2866 (1992).

[197] E. Alba, X. Fernandez-Gonzalvo, J. Mur-Petit, J. K. Pachos, and J. J. Garcia-Ripoll, “Seeing topological order in time-of-flight measurements”, Phys. Rev. Lett. **107**, 235301 (2011).

[198] N. Goldman, E. Anisimovas, F. Gerbier, P. Öhberg, I. B. Spielman, and G. Juzeliūnas, “Measuring topology in a laser-coupled honeycomb lattice: from chern insulators to topological semi-metals”, New Journal of Physics **15**, 013025 (2013).

[199] Y. Tanaka, T. Yokoyama, and N. Nagaosa, “Manipulation of the majorana fermion, andreev reflection, and josephson current on topological insulators”, Phys. Rev. Lett. **103**, 107002 (2009).

[200] S. Mondal, D. Sen, K. Sengupta, and R. Shankar, “Tuning the conductance of dirac fermions on the surface of a topological insulator”, Phys. Rev. Lett. **104**, 046403 (2010).

[201] S. K. Banerjee, I. L. F. Register, A. MacDonald, B. R. Sahu, P. Jadaun, and J. Chang, *Topological insulator-based field-effect transistor*, US Patent 8,629,427, Jan. 2014.

[202] S. Zhang and X. Zhang, *Electrical and optical devices incorporating topological materials including topological insulators*, US Patent 9,024,415, May 2015.

[203] B. Scharf, A. Matos-Abiague, J. E. Han, E. M. Hankiewicz, and I. Žutić, "Tunneling planar hall effect in topological insulators: spin valves and amplifiers", Phys. Rev. Lett. **117**, 166806 (2016).

[204] T. Oka and H. Aoki, "Photovoltaic hall effect in graphene", Phys. Rev. B **79**, 081406 (2009).

[205] N. Goldman, J. C. Budich, and P. Zoller, "Topological quantum matter with ultracold gases in optical lattices", Nature Physics **12**, 639–645 (2016).

[206] H. Miyake, G. A. Siviloglou, C. J. Kennedy, W. C. Burton, and W. Ketterle, "Realizing the harper hamiltonian with laser-assisted tunneling in optical lattices", Phys. Rev. Lett. **111**, 185302 (2013).

[207] L. Riegger, N. Darkwah Oppong, M. Höfer, D. R. Fernandes, I. Bloch, and S. Fölling, "Localized magnetic moments with tunable spin exchange in a gas of ultracold fermions", Phys. Rev. Lett. **120**, 143601 (2018).

[208] G. Jotzu, M. Messer, F. Görg, D. Greif, R. Desbuquois, and T. Esslinger, "Creating state-dependent lattices for ultracold fermions by magnetic gradient modulation", Phys. Rev. Lett. **115**, 073002 (2015).